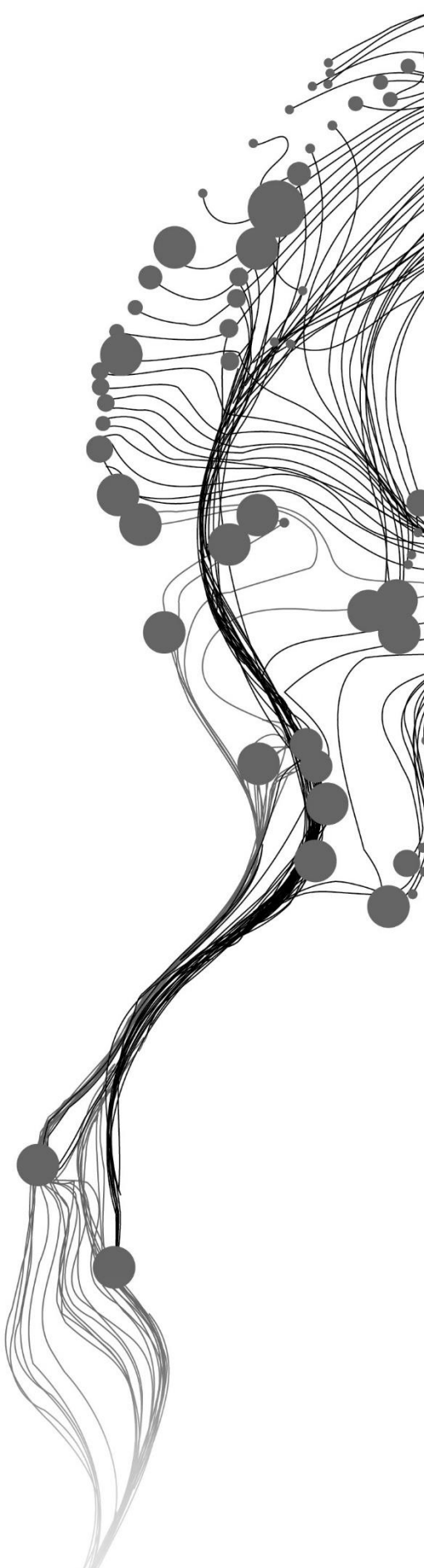


**GLACIER FACIES
CLASSIFICATION AND
COMPARISON OF VELOCITY
ESTIMATION TECHNIQUES
USING SAR AND OPTICAL
DATASETS**

ARAVIND M
August 2022

SUPERVISORS:
Dr. P. K., Thakur
Dr. Ling Chang



GLACIER FACIES CLASSIFICATION AND COMPARISON OF VELOCITY ESTIMATION TECHNIQUES USING SAR AND OPTICAL DATASETS

ARAVIND M

Enschede, The Netherlands, January 2023

Thesis submitted to the Faculty of Geo-Information Science and Earth
Observation of the University of Twente in partial fulfilment of the
requirements for the degree of Master of Science in Geo-information
Science and Earth Observation.

Specialization: Geoinformatics

SUPERVISORS:

Dr. P. K., Thakur

Dr. Ling Chang

THESIS ASSESSMENT BOARD:

Dedicated to my Mother and Father

DISCLAIMER

This document describes work undertaken as part of a programme of study at the Faculty of Geo-Information Science and Earth Observation of the University of Twente. All views and opinions expressed therein remain the sole responsibility of the author, and do not necessarily represent those of the faculty.

ABSTRACT

Glaciers are important features of the cryosphere that command the microclimate and water availability that are relied upon by many communities. The phenomenon of global warming has put the fragile glacial ecosystem of the Himalayas at the risk of recession. This detrimental effect is caused by variations in multiple parameters of the glacier. It affects the millions who reside downstream that rely on the water source fed by the glaciers. Bada Shigri, Chota Shigri and Gepang Gath of the Chandra basin, are such glaciers that directly contribute to the water level of the Chandra River. Hence, this study focusses on classifying the various zones of the glaciers with SAR imagery to map the accumulation zone, ablation zone and the resulting equilibrium altitude line (ELA)..

The glaciers were classified by using satellite imagery from three different seasons- early summer, late summer, and winter. Five zones namely upper percolation zone, middle percolation zone, lower percolation zone, bare ice and debris were mapped and quantified with a random forest classifier with an out of bag accuracy of 97%. All three glaciers showed an increase in elevation of the ELA depicting an increase in area of ablation zone through the years of 2019-2022.

The study also estimates the velocity of each glacier, an important parameter that keeps a check on glacier's health and hazards, using feature tracking, Time series InSAR (Using MintPy) methods on SAR and optical imageries. The velocity showed a downward trend through 2019-2022. The obtained values were compared with historical dataset and GoLive global velocity dataset. Although the results aligned with the historical velocity trend, it showed a high deflection from the values obtained from GoLive..

Keywords- Facies classification, ELA, Glacier velocity, SAR, Feature tracking, Time series InSAR, Indian Himalyas.

ACKNOWLEDGEMENTS

Any research is a collective endeavour of many who work for its betterment directly or indirectly. I would like to offer my sincere gratitude to everyone who was a part of this journey. This masters study had its highs and lows, but the people involved made every moment worthwhile, and the whole experience was nurturing

The constant support and guidance from Dr.Praveen Thakur and Dr.Ling Chang sparked my interest in the field of cryosphere and remote sensing as a whole. Their extensive knowledge in the field is very inspiring and is going to help me in my future aspirations.

I would like to thank my colleagues, Shivang Pandey, Neethu Narayanan, Prateet Tiwari, Rohith Badrigari, Gautamee Baviskar, Omkar Jadhav, Ketaki Jambhali and Shanmathi who took their time in their busy schedules out to help me with the research. I would like to thank my IIRS peers Rayyan Shaik, Arshad Mohammed, Sukalpa, Vaibhav Dhawan, Akshay Sinha, Saraanch Raghav, Vivek Kumar, Arsalaan, Akarsh, Mayank for their constant support in this journey.

I would like to thank the ITC faculties and its various wings for making my stay in Netherlands one of the best moments of my life. I would also like to thank the IIRS GID department for sharing their expertise in the field of remote sensing which set the foundation for the research.

I would like to thank my mother, Father, and Brother who were always by my side during the tough phase of the study program and research.

TABLE OF CONTENTS

1.	Introduction	8
1.1.	Background	8
1.2.	Motivation	8
1.3.	Related Work	9
1.4.	Thesis Outline	10
2.	Research Identification	11
2.1	GENERAL objectives	11
2.2	Sub objectives	11
2.1	Research Questions	11
3.	Literature Review	12
3.1	Glaciers	12
3.1.1	Evolution of Glaciers	12
3.1.2	Glacial Studies over the years	13
3.2	Synthetic Aperture Radar	13
3.2.1	SAR and Glacier Radar Zones	15
4.3	Glacier Movement	17
4.4	Interferometry	18
4.5	SUMMARY	19
5.	METHODOLOGY	20
5.1.	Velocity Estimation	20
5.1.1	Pixel/Feature Tracking	20
5.1.2	Time Series InSAR	23
5.1.3	Miami Time InSAR and its Workflow	24
5.2	Glacier Facies Classification	26
5.2.1	Random Forest Classifier	28
6.	Materials	29
6.1	Study Area	29
6.2	Datasets used	31
7.	Results	33
7.1	Glacier Facies Classification	33
7.1.1.	Bada Shigri Glacier	34
7.1.2	Chota Shigri Glacier	36
7.1.3	Gepang Gath Glacier	38
7.1.4	Accuracy Assessment	41
7.2	Velocity Estimation of the Glaciers	41
7.2.1	Optical Feature Tracking	41
7.2.2	Time Series InSAR	45
8.	Discussion & Conclusion	49
8.1	Equilibrium Line Altitude (ELA) of the Glaciers [2020-2022]	49
8.2.	Glacier Velocity	54
8.2.1	GoLIVE Velocity trend	56
8.3	Research Questions	57
8.4	Future Scope of work	59
	REFERENCES	60

9.ANNEXURE	68
Feature Tracking with SAR Dataset.....	68

LIST OF TABLES

<i>Table 1 SAR missions over the years</i>	14
<i>Table 2 Appearance of each glacier zone and their level of backscatter intensity (Partington, 1998).....</i>	27
<i>Table 4 Dataset used for polarimetric classification</i>	32
<i>Table 3 Dataset used for Optical feature tracking and SAR pixel tracking</i>	32
<i>Table 5 Historical ELA data of Chota Shigri Glacier.....</i>	51
<i>Table 6 Historical ELA data of Bada Shigri Glacier</i>	51
<i>Table 7 Historical ELA data of Gepang Gath glacier</i>	51
<i>Table 8 Area of each classified zone of Bada Shigri glacier</i>	52
<i>Table 9 Area of each classified zone of Chota Shigri glacier</i>	53
<i>Table 10 Area of each classified zone of Gepang Gath glacier.....</i>	53
<i>Table 11 Historical velocity data of Bada Shigri glacier.....</i>	55
<i>Table 12 Historical velocity data for Chota Shigri glacier</i>	55
<i>Table 13 Historical Velocity data of gepang gath glacier.....</i>	56

TABLE OF FIGURES

Figure 1 Stages of Snow	12
Figure 2 Geometry of SAR sensors(X. Zhou et al., 2009)	14
Figure 3 Different Scattering mechanisms of snow in response to SAR signals(Koskinen et al., 2000).....	15
Figure 4 Glacial radar zones (Partington, 1998b).....	16
Figure 5 Glacier Movement Scenarios (Siegert, 2008).....	17
Figure 6 Depiction of the Concept of interferometry (Osmanoğlu et al., 2016).....	18
Figure 7 Workflow for pixel tracking for velocity estimation.....	20
Figure 8 Workflow for feature tracking of optical imagery for velocity estimation.....	21
Figure 9 Workflow followed for computing velocity with Time series InSAR.....	23
Figure 10 Routine Workflow of MintPy (Yunjun et al., 2019)	24
Figure 11 Workflow adopted for glacier facies classification.....	26
Figure 12 Working of a Random Forest Classifier (Davis David, 2020).....	28
Figure 14 Map showing the Study area of Bada Shigri glacier.	29
Figure 15 Figure showing the study area of Chota Shigri glacier [you have two figure 15].....	30
Figure 16 Study Area of Gepang Gath glacier	31
Figure 17 Example of RGB Composites of the study area. Top left- Bada Shigri glacier; Bottom left- Gepang gath glacier; Right- Chota Shigri Glacier	33
Figure 18 Graphs of mean score of each parameter of RF classifier.....	34
Figure 19 Bada Shigri Glacier Classified Map.....	35
Figure 20 Bada Shigri Glacier Classified map- 2021.....	35
Figure 21 Bada Shigri Glacier Classified map 2022.....	36
Figure 22 Chota Shigri Glacier Classified Map- 2021	37
Figure 23 Chota Shigri Glacier Classified Map- 2020	37
Figure 24 Chota Shigri Glacier Classified Map- 2022	38
Figure 25 Gepang Glacier Classified Map- 2020	39
Figure 26 Gepang Gath Glacier Classified Map- 2021	39
Figure 27 Gepang Gath Glacier Classified Map- 2022.....	40
Figure 28 Gepang Gath Glacier Classified Map- 2022.....	40
Figure 29 Error Matrix of the Classification process	41
Figure 30 Cosi-Corr Result for Bada Shigri glacier 2019-2022.....	42
Figure 31 Cosi-Corr Result for Chota Shigri glacier 2019-2022.....	43
Figure 32 Cosi-Corr Result for Gepang Gath glacier 2019-2022	44
Figure 39 Average Coherence of the interferogram pairs	45
Figure 40 Average spatial coherence of each image.....	46
Figure 41 Minimum and Maximum coherence of each interferogram pair.....	46
Figure 42 Perpendicular baseline of each image pair.....	47
Figure 43 InSAR results of Bada Shigri ,Chota Shigri and Gepang Gath Glaciers	48
Figure 44 ELA trend of Bada Shigri Glacier.....	49
Figure 45 ELA Trend of Chota Shigri Glacier.....	50
Figure 46 ELA Trend of Gepang Gath Glacier.....	50
Figure 47 Past Velocity data of Bada Shigri glacier (Yellala et al., 2019a).....	54
Figure 48 Past Velocity trend of Chota Shigri Glacier (Yellala et al., 2019b).....	55
Figure 49 GoLive Velocity trend graph 2014-2021	57
Figure 33 Screenshot of Co-registration process and the relevant parameters. Map of chosen master points.....	68

Figure 34 Velocity Scatterplot for 2017-2018.....69
Figure 35 Velocity Scatterplot for 2018-201969
Figure 36 Velocity Scatterplot for 2019-202070
Figure 37 Velocity Scatterplot for 2020-202170
Figure 38 Velocity Scatterplot for 2021-202271

LIST OF ACRONYMS

IHR	Indian Himalayan Region
ELA	Equilibrium Altitude line
SLC	Single look complex
GRD	Ground Range Detection
PolSAR	Polarimetric Synthetic Aperture Radar
SAR	Synthetic Aperture radar
JAXA	Japanese aerospace exploration agency
NASA	National aeronautics and space administration
CS, BS	Chota Shigri, Bada Shigri glaciers
GG	Gepang Gath glacier
DEM	Digital elevation model
InSAR	Interferometric synthetic aperture radar
DInSAR	Differential interferometric synthetic aperture radar
FAU	Friedrich Alexander University
IW	Interferometric swath width
SNR	Signal to noise ratio
RF	Random Forest
SVM	Support vector machines
ASF	Alaska State facility
SBAS	Small baseline subset
LOS	Line of Sight
MintPy	Miami time InSAR python library
ANN	Artificial Neural network
ML	Machine learning
M.S.L	Mean Sea level

1. INTRODUCTION

1.1. Background

While several countries are striving for a greener and cleaner future, it is no surprise that climate change has been a bane for humanity. It has set off a chain of tragic events in the past and continues to do so. One of them being the melting of glaciers. Glaciers are massive geological features that are formed over thousands of years of accumulation of ice and snow.

They are extremely reactive towards minor changes in temperature (Kääb et al., 2007); (Anil V. Kulkarni et al., 2011) which results in their recession. Hence, they have become an important indicator of global warming, varying weather patterns, rise in sea level, exhaustion of freshwater resources and an imminent risk of glacial hazard put the majority of living organisms on Earth in a perilous state. (Sood, 2016)

Mountainous glaciers are origin points of major rivers which aid in irrigation and hydro-electric projects (Neyret & Benastar, 2005). Although the polar regions have the largest glaciated zones, The Himalayan region contains the third largest amount of fresh water in the form of snow and glaciers (Thakur et al., 2017). The Glaciers of the Himalayan Mountain range contribute and give birth to a lot of major rivers in India. These rivers are relied upon by billions of people for efficient agriculture, consumption etc. These cryospheric features have depicted continuous retreat since 1850 due to global warming (Paul et al., 1979). Accelerated melting of these geological features can trigger natural disasters like avalanches, flash floods in mountains and can disrupt the lives of billions. The Himalayan glaciers are especially sensitive to variations in weather patterns and cause disruptions to the local temperature and precipitation trends (Ding et al., 2006) (Mayewski & Jeschke, 1979). Due to these factors of sensitivity, it is crucial to evaluate the growth of these cryospheric systems (Bolch et al., 2012). Such an evaluation of these systems can assist in reducing potential hazards. Glaciers are often present in inaccessible terrains, hence, the most germane way to monitor these geographical features can only be through incessant remote sensing (Barry, 2006)

1.2. Motivation

The new age increase in warmth of the atmosphere (NASA, 2022) has had a negative influence on polar and mountainous glaciers alike. It has induced a change in their mass balance (Zemp et al., 2019) and their dynamics. Since human dependence on them is high for freshwater, prevention of natural hazards (Moore et al., 2009) and controlling the sea level rise (Bamber & Rivera, 2007), it is important to monitor their parameters constantly.

Glacier velocity is one such parameter that gives a crucial insight into the dynamics of a glacier (Rutberg et al., 2000) (Van Wychen et al., 2014) which in turn gives us an idea of its health. Almost all the existing global ice velocity products use optical data for analysis of various parameters of the cryosphere. Ice surface velocities on a global scale can currently only be obtained from ITS_LIVE ADD (Gardner et al. 2018; Gardner et al. 2019) and the GoLIVE (Scambos et al., 2004) (Scambos et al. 2016; Fahnestock et al. 2016) data sets, where LANDSAT optical data is relied upon for velocity computations. This may cause gaps in data as optical data relies on perfect weather and meteorological conditions. A SAR (Synthetic Aperture Radar) based velocity product (Friedl et al., 2021) named FAU, derived from Sentinel 1, uses

offset tracking method for estimation of velocity of 12 major glaciated zones of the world. Although Offset tracking has been successfully applied on various velocity studies (Sánchez-Gómez et al., 2017) (Baek et al., 2018), it may not be a suitable method to estimate the velocity for every glacier. Since decorrelation has no influence on offset tracking, it is more suitable for glaciers with high velocity, while DinSAR (Differential synthetic aperture interferometry) performs better on slow moving glaciers and normalized cross correlation with optical data tends to be efficient for both slow and fast moving glaciers (Sivalingam et al., 2021). Hence it is essential to evaluate the existing global velocity products as they are relied upon by many for cryosphere modelling studies. (Sivalingam et al., 2021) suggests that it is better to choose a technique specific to the glacier depending upon its velocity rate. Various velocity estimation techniques have been used over the study area, but a valid comparison of these methods have never been done before. It is essential to implement and compare the commonly used velocity estimation methods.

A glacier has a complex terrain, and its surface characteristics keep varying depending on the overlying snowpack conditions. These surface facies are key supraglacial features that require constant monitoring (Shridhar Jawak, Sagar Filipe, 2022). Crucial data can be extracted from such surface features and be assimilated for distributed mass balance modelling. Hence accurate facies identification and mapping of the same is essential to keep a check on the glacier's health. This process also helps in identifying and quantifying the extent of accumulation and ablation zones of the glacier. Mapping the equilibrium altitude line (line that separates the accumulation and the ablation zones) and observing its altitude change over the years can give a direct knowledge on if a glacier is gaining or losing mass.

Although a lot of studies on facies mapping have been carried out in the arctic (Alvarinho J. Luis, 2020) (Wolken et al., 2009) and the Antarctic (C. Zhou & Zheng, 2017), such facies mapping and monitoring is very limited in the IHR (Indian Himalayan region). This is crucial as glacial hazards have an upward trend in the Himalayas (Sayantan Das et al., 2015).

Since glaciers provide a key indication of climate change, every bit of contribution from any sector would be a big boon for climate studies. The Himalayas have always been known its serene beauty and has been an important centre for tourism (Apollo et al., 2022). Accelerated glacier melt and improper monitoring of them would affect the country and the world (Bishop, 2022).

1.3. Related Work

- (i) (Sood, 2016) – Classified and computed the velocity of Samudra Tapu glacier using SAR polarimetric decomposition, Feature tracking and InSAR methods.
- (ii) (Vijay Mahagaonkar, 2019)- Classified and computed velocity of Siachen, Bada shigri and Gangotri glaciers for the years 2015-2018 using SAR polarimetric and interferometric methods.
- (iii) (Sivalingam et al., 2021) studied glacier velocity in the Karakoram ranges using various feature tracking and DinSAR methods.
- (iv) (Adam et al., 1997) Mapped the snow line of Place glacier using ERS-1 SAR Imagery.
- (v) (V. Kumar et al., 2011) estimated the parameters of snow and monitored the movement of Gangotri glacier using ALOS-PALSAR dual pol data.
- (vi) (Huang & Li, 2011) monitored glacial radar zones and changes in the ELA line in the Qinghai-Tibetan Plateau using SAR imagery in C-band.
- (vii) (Jiang et al., 2021) computed the surface flow velocity of Yengisogat glacier using feature tracking of ALOS PALSAR data.

- (viii) (Strozzi et al., 2002) estimated the movement of Monacobreen glacier in the Svalbard region by utilizing feature tracking of ERS SAR data.
- (ix) (Partington, 1998a) identified the radar glacial zones of Greenland ice sheet and Warangell St. Elias mountain in Alaska, using multitemporal ERS-1 SAR dataset.
- (x) (Nijhawan et al., 2016) took advantage of multispectral images for comparing different classification methods for detecting change in glaciers in a part of Alakananda basin,

1.4. Thesis Outline

The thesis intends to be an organized document for easy interpretability for readers and future references. It is split into 9 chapters. Chapter 2 gives an overview of the study to be carried out. Chapter 4 explains the relevant literature required for a better understanding of the work. Chapter 5 depicts the workflow adopted for carrying out each analysis. Chapter 6 describes the area of study and datasets used for the completion of the study. The results, discussion of the same and the relevant conclusion is given in chapters 7 and 8 respectively. The remaining chapters answer the research questions and show the various research papers that were referred to for the successful completion of the work.

2. RESEARCH IDENTIFICATION

2.1 GENERAL OBJECTIVES

The key objective of this work is to classify facies and to implement, compare, and validate techniques for estimation of velocity of a glacier.

2.2 SUB OBJECTIVES

1. To map glacier facies using Polarimetric SAR technique and to classify it using a machine learning classifier.
2. To estimate change in ELA of the glacier.
3. To implement, compare and evaluate various velocity estimation techniques and a global glacier velocity product.

2.1 RESEARCH QUESTIONS

The following research questions will be addressed

1. Referring to sub-objective 1:
 - a) What methods are applicable for glacier facies classification?
 - b) Which machine learning classification algorithm is optimal for an accurate facies' classification?
2. Referring to sub-objective 2:
 - a) How can the accumulation and ablation zones be mapped?
 - b) How has the ELA evolved over the years and what could be the driving factors behind this?
3. Referring to sub-objective 3
 - a) How has the velocity trend changed over the years?
 - b) Which published data can be used for an accurate validation?

3. LITERATURE REVIEW

This chapter intends to guide the reader through the concepts of radar technology and how it can be exploited for cryospheric studies. It depicts the morphology of a glacier and how its different parts respond to radar waves. One can also understand the process of glacier movement and the methods that can be used for quantifying it.

3.1 Glaciers

3.1.1 Evolution of Glaciers

Glaciers are features that are formed by years of continuous accumulation of snow. In polar regions, glaciers often reside in both plain and mountainous elevations alike. In temperate regions, they can only exist in higher altitudes which faces adequate snowfall and low temperatures.

Glaciers form in an environment where the snow that precipitates in the winter of a year make it through to the following year's summer without melting. This results in the accumulation of snow which eventually turns into ice due to the pressure of the newer overlying snow. The process of snow to ice conversion is a slow one and can take upwards of ten years (Kodde et al., 2007) . The materials involved goes through a lot of transitional phases. First, the accumulated snowflake crystals get disintegrated into smaller grains due to the above-mentioned pressure. This results in a finer and denser state of snow called firn. This is usually present in regions where the new snow interacts with underlying glacier ice. Firn eventually crystallizes due to low temperatures. This time, resulting in bigger crystals to form solid ice. This state is extremely dense and only has room for small bubbles of air.

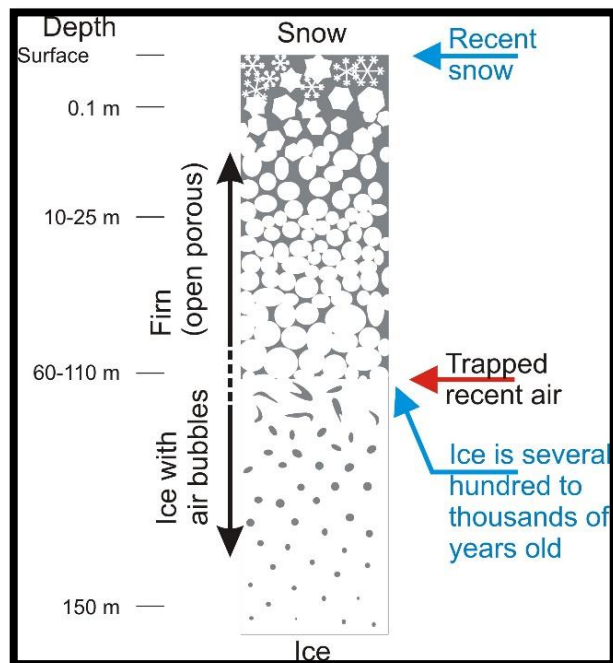


Figure 1 Stages of Snow
(Blunier & Schwander, 2000)

The density of snow is about 50-200 kg/m³ firn about 400-530 kg/m³ and ice about 800-930 kg/m³ (Armstrong & Brun, 2010) (Kurt Cuffey, 2006).

The shape of ice crystals is constantly changing due to the steady movement of the glacier. Due to this movement, the evolution of a glacier from snow to solid ice is visible spatially. Aged ice is present at the snout of a glacier while the younger ones are found upstream of it i.e, ice consists of firn at a relatively high elevation and snow at an even higher elevation.

This geographical difference of presence of different state of snow can be exploited for various earth observation applications and cryospheric studies as each state has a unique rate of absorption and reflectivity (Kodde et al., 2007). An example of this is that of (Lutz et al., 2003) who studied the difference in backscatter intensity of each state of snow using a laser scanner. Another study (Murray et al., 2007) exploited the difference in dielectric properties (water content in particular) of each zone of a glacier. SAR signals are fully reflected by water and hence can't penetrate it.

3.1.2 Glacial Studies over the years

Glacial studies started in the early 1900's to study about clues of the past ice age. These studies evolved into glacier health monitoring in the early 2000's once global warming was identified as an issue. These studies started with traditional field surveys. (Hambrey et al., 2005) quantified accumulation and ablation in terms of SWE (snow water equivalent) by using stakes and pits on the glacier surface.

Glacier velocity was determined with the help of theodolites and calculating their distance from nearby fixed features by (Kurt Cuffey, 2006). Glacier behaviour was studied (Douglas I. Benn & Evans, 1996) by monitoring the snout of a glacier using total station and differential GPS.

These studies eventually utilized remote sensing technology due to the obvious difficulty in accessing glaciers, which usually reside in areas of rugged terrain and extreme weather conditions (Bolch et al., 2012). Although remote sensing provides an all-weather observing capability of glaciers, it is only a partial substitute to traditional field measurement methods (Bolch et al., 2012).

The initial remote sensing studies made use of optical remote sensors. (Jesko Schaper, 2000) studied the daily runoff of snow and glacier melt. (Frauenfelder & Kääb, 2000) studied glacier related hazards in the Swiss alps. Although optical remote sensing proved to provide robust data for analysis, it can't be used in overcast weather as the waves can't penetrate clouds. With the advent of SAR technology, this problem was eliminated.

3.2 Synthetic Aperture Radar

Synthetic aperture radar (SAR) was invented in 1951 by Carl Wiley. SAR sensors emit microwave radiations onto earth's terrain and receives back the backscattered. Signals with an antenna. This process leads to the creation of an image that is synthesized by motion of the sensor system (Sridhar Jawak, 2015). Since its genesis, SAR technology has been constantly evolving. The first sensors were that of RORSAT (1967-1988) of the Soviet Union, SAR Lupe of the German air force, COSMO-SkyMed of Italy (2007) and TecSAR of Israel (2008). Just like most other remote sensing technologies, SAR was kept under the sheets for the public and was primarily used for military purposes (Aher et al., 2014).

The first homegrown Indian satellite, Radar imaging satellite (Risar-1) was launched in 2012. Its data has been put in use in various fields like agriculture, Forestry, and disaster management (Aher et al., 2014).

Satellite	Region, Year	Spatial Resolution(m)	Polarization	Frequency	Band
RISAT-1	India,2012	3 to 50	HH,HV,VH,VV,RH,RV	5.3 GHz	C
Sentinel-1	Europe,2014	5x10(TW)	HH+HV,VV+VH,VV,HH	5.3GHz	C
ALOS-2	Japan,2014	10-100	HH,HV,VH,VV	1.2 GHz	L
Tandem-X	Germany,2010	1-16	HH,VV	9.65 GHz	X
ERS-1/2	Europe('91/'95)	30	VV	5.25GHz	C
SRTM	USA/Germany(2000)	30	HH,VV	5.25/9.6	C,X
JERS-1	Japan (1992)	20	HH	1.275	L
Radarsat-1	Canda,1995	10-100	HH	5.3 GHZ	C
ENVISAT	Europe,2002	5.6	HH,HV,VV,VH	5.6	C

Table 1 SAR missions over the years

Synthetic aperture radar technology, with its all-weather day and night imaging capability, proves to be an appropriate alternative to optical imagery (Baghdadi et al., 1997). Being an active sensor, it overcomes the issues faced by traditional passive remote sensors. It also has the capability of penetration which helps in imaging sub surface and hyper-arid features.

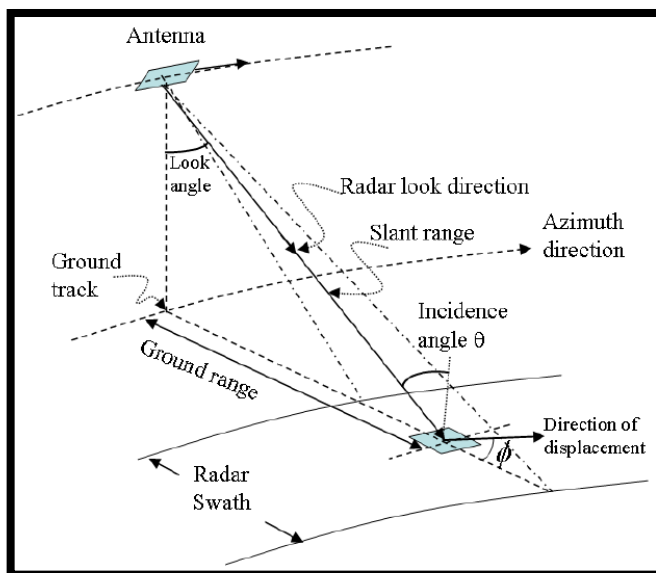


Figure 2 Geometry of SAR sensors(X. Zhou et al., 2009)

As mentioned above, the active SAR waves interact and gets scattered by objects on ground. The radiations that are partially scattered are recorded with antennas for extracting phase and amplitude information. Amplitude is the energy of the backscatter that is recorded by the receiver, and it represents an object's surface texture and dielectric properties (Ulaby et al., 1982). Phase depicts the distance that the wave takes to travel to hit an object and back to the receiver. The obtained data can only be utilized when

the sensors are side-looking, hence SAR sensors have a side-looking imaging geometry (Moreira et al., 2013) as represented in the figure above. The look angle represents the angle of sight of the surface. Incidence angle depicts the angle between the perpendicular drawn from the sensor to the object on ground and the incident beam. Azimuth angle depicts the angle between the look direction and satellite track on the horizontal plane (Vijay Mahagaonkar, 2019). Along with the phase and amplitude, the polarisation of the receiving wave is also recorded which provides extra information of the surface objects.

Comprehensive studies on snow and glaciers have been carried out to assess the performance of SAR (Rott & Mätzler, 1987). ERS-1, Sentinel-1, Japanese earth resource satellite (JERS), Radarsat-2, Terrasar-X etc. are used for monitoring the cryosphere. Polarimetry was utilized for modelling surface topography in 1980s (Gabriel et al., 1989) (Massonnet et al., 1993) (Shi & Dozier, 1995). Interferometry was used for measuring subsidence and movement.

3.2.1 SAR and Glacier Radar Zones

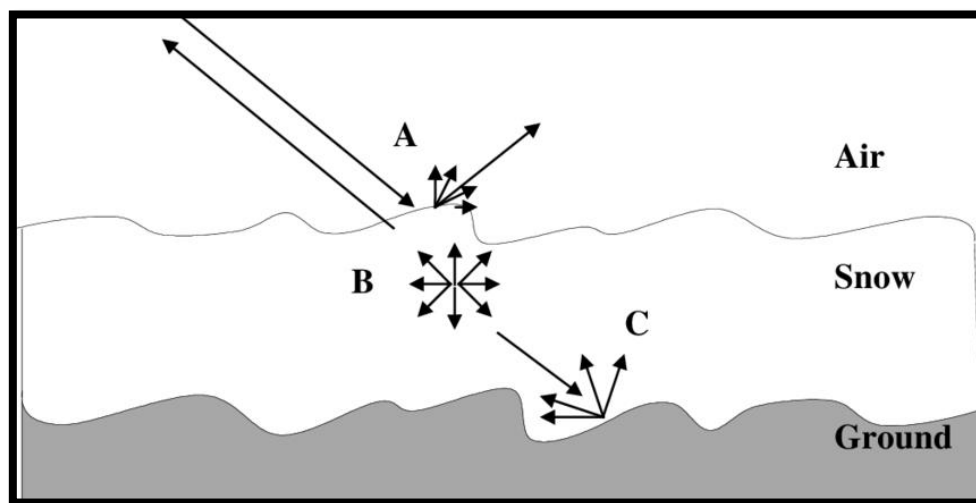


Figure 3 Different Scattering mechanisms of snow in response to SAR signals (Koskinen et al., 2000)

SAR signals undergo different interactions depending on the di-electric properties of the snowpack conditions. As temperatures would be higher at the lower elevations of a glacier, the water content would be higher in the snowpack. The higher elevations of the glacier would be much drier. The radar backscatter is affected by such changes in the di-electric properties like moisture and surface roughness. They are also affected by the incidence angle and wavelength polarisation of the satellite transmitter (Hall et al., 1987). As depicted in figure 3, volumetric scattering occurs in the case of dry snow as radiations of a higher frequency are transparent to it. Surface scattering occurs in the case of wet snow as SAR signals can't penetrate wet conditions (Rott & Mätzler, 1987).

The higher elevation sections of the glacier house the dry snow zone where annual temperatures go as low as -25 degree Celsius. Because of this, no melting occurs even during summer. Volume scattering of radar signals are prominent here and they can penetrate up to 20 meters (König et al., 2001). This region can be as a darker region in SAR imagery (Partington, 1998b).

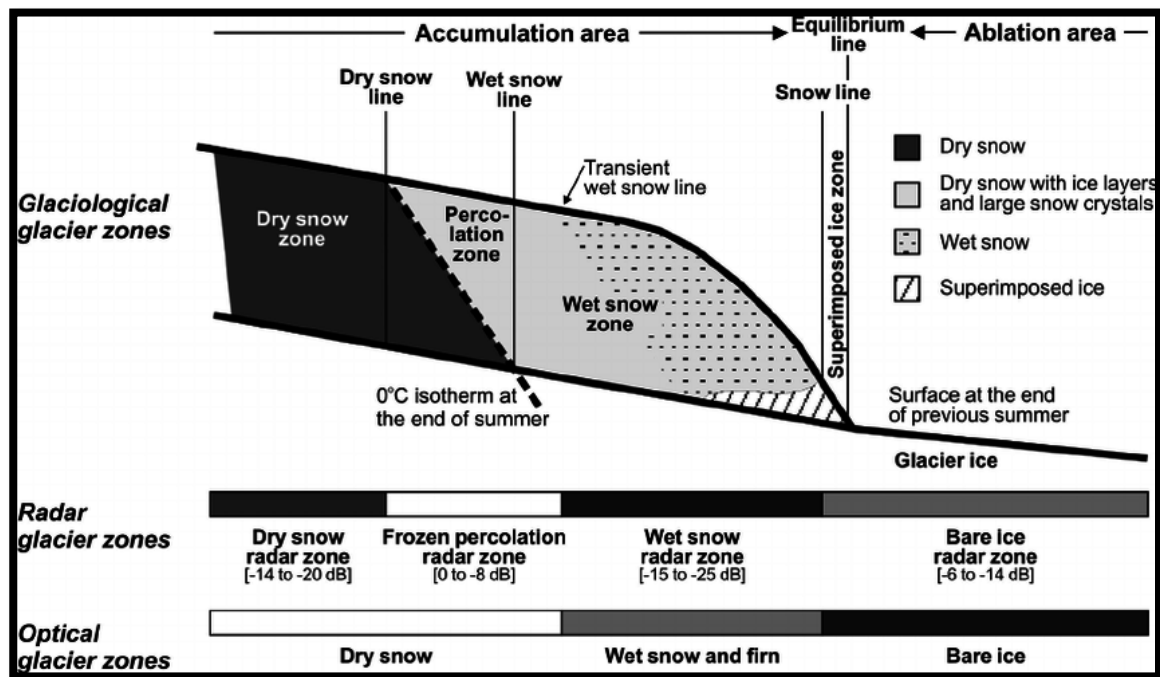


Figure 4 Glacial radar zones (Partington, 1998b)

The dry snow zone is followed by the percolation zone where melting of surface snow that had accumulated during the preceding precipitation season occurs. The melted snow percolates the surface and refreezes. This results in the emission of latent heat leading to the creation of ice lenses and vertical ice glands (Kurt Cuffey, 2006). The backscatter in this region is higher during winter season due to the presence of these small ice structures, while it's considerably lower during summer as meltwater appears in the surface.

The next zone that appears is that of the wet snow. The preceding season's whole accumulation of snow melts and refreezes in this zone. The lower regions of this zone experiences more prominent melting leading to the formation of slush. (Kurt Cuffey, 2006). This zone depicts a low backscatter during summer due to presence of water while a higher backscatter during winter can be seen.

A high number of ice lenses reside in the superimposed ice zone due to refreezing of melt water from the wet snow zone. It has a relatively high density. The wet snow and the superimposed ice zones are split by an imaginary line known as the snow line. In glaciers that face a higher rate of ablation, superimposed ice zones may cease to exist as refreezing may not be possible. (Partington, 1998b). The backscatter of superimposed ice and bare ice is very similar and can be differentiated with the help of their textures (Superimposed ice is smoother).

The ablation zone marks the end of a glacier and is present downstream at the lowest part of it. This zone is characterized by rough ice facies which helps in differentiating it from the superimposed ice zone (Vijay Mahagaonkar, 2019). The amount of accumulation of snow is lesser than the amount of melting here. Hence, during summer, a high backscatter value is observed as melt rate is high. The line separating the accumulation and ablation zone, marked between the bare ice facies and superimposed ice zone is known

as the ELA. In the Himalayas where the superimposed ice zone is rarely present, the line resides between the ablation and wet snow zones (Vijay Mahagaonkar, 2019).

4.3 Glacier Movement

A Mountainous glacier moves depending on its interaction with its bedrock and the characteristic of ice present in them. A change in this environment can cause prolonged (Dehecq et al., 2019), short-term (Vijay et al., 2019) (Partington, 1998a) (Moon et al., 2014) and rapid variations in velocity at the surface level (Bhambri et al., 2017). Velocity of ice is an important parameter for ice dynamic modelling, mass balance calculation studies as it's the main predictor of ice discharge. (Farinotti et al., 2019) (Bamber & Rivera, 2007). They are essential to keep a check on ice crevassing, sudden glacier retreat (Barry, 2006) (Fischer et al., 2003) and glacial hazards (Kaab et al., 2003).

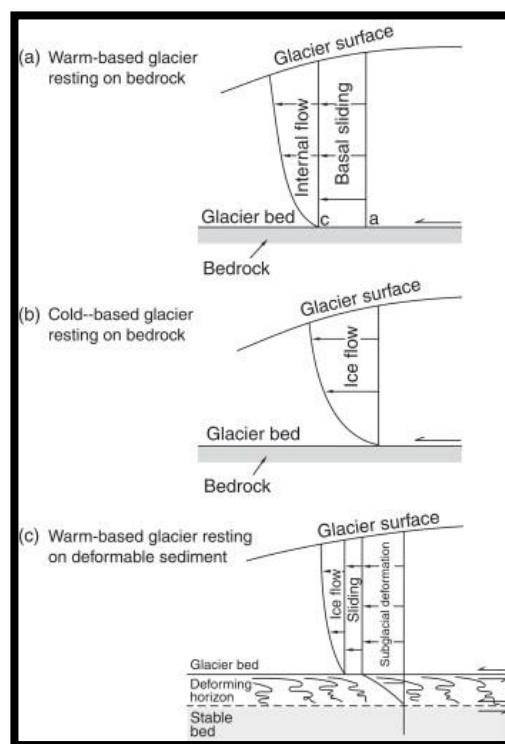


Figure 5 Glacier Movement Scenarios (Siegert, 2008)

The movement of a glacier can happen in the following ways,

- (A) Internal deformation occurs due to ice creep i.e., movement of ice crystals inside the glacier
- (B) Basal sliding occurs when the resistance betwixt the bedrock and glacier reduces due to presence of basal meltwater.
- (C) Subglacial deformation occurs when glacier is separated from its underlying glacial sediments.

4.4 Interferometry

SAR interferometry has demonstrated to be an efficient method for determining glacial velocity (V. Kumar et al., 2011), which in turn helps to keep a check on their melt (Erten et al., 2009). The phase information of SAR signals are exploited for determining the topographical changes over a region of interest (Hanssen;RF, 2001).

Figure 6 illustrates the basic concept of repeat pass interferometry. An initial pass over the subject of interest by the satellite acquires the master image along with its phase information and LOS. A second pass over the same region acquires the slave image. Perpendicular (B_{\perp}) and parallel (B_{\parallel}) baselines are hence formed.

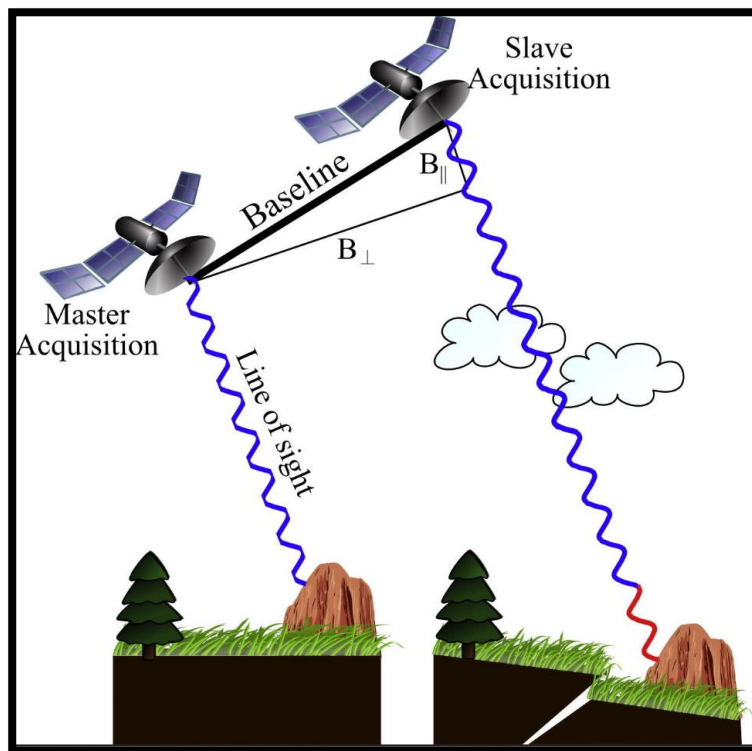


Figure 6 Depiction of the Concept of interferometry (Osmanoğlu et al., 2016)

Perpendicular baseline represents the length between the two positions of acquisition that is perpendicular to the look angle of the satellite. The summation of parallel and perpendicular baselines shows the total spatial baseline between the master and slave acquisitions (Osmanoğlu et al., 2016). The temporal baseline depicts the time between sensing of the two images.

The process demands two scenes sensed in different viewing angles by making use of two antennae or by using different passes of the same antenna. Pixel-by-pixel co-registration is performed on these two images and the difference of phase between them is computed (Huang & Li, 2011). The difference is calculated with the equation (Reigber & Scheiber, 2003).

$$\phi = \phi_{topo} + \phi_{earth} + \phi_n + \phi_{atm} + \phi_{\Delta r} \quad (1)$$

In equation 1, ϕ_{topo} depicts phase difference produced by topography of terrain. ϕ_{earth} , the systematic phase produced by flat earth. ϕ_n represents the SNR ratio and decorrelation on the temporal scale. ϕ_{atm} depicts the difference in phase caused by varying atmospheric conditions, and $\phi_{\Delta r}$ is the change in phase caused by variations in the slant range distance. (Bhattacharya et al., 2011) describes that the best state to observe surface deformations when the acquired images have minimal baseline between them. Phase shift is caused by movement in ground or other effects of topography in a minimal baseline condition. Usage of an external DEM or a common master interferogram can eliminate topographic effects (V. Kumar et al., 2011). This method is called DInSAR, it eliminates both ϕ_{topo} and ϕ_{earth} from the equation.

Interferometry is possible when two antennas have an overlapping ground reflectivity among them. For understanding the relationship between the orbits of master and slave images, the orbital baseline is estimated. Interferometry is not possible when the perpendicular baseline B_{\perp} exceeds a particular limit called as the critical baseline as the preservation of phase information and loss of coherence occurs (Sood, 2016).

A complex interferogram is created by multiplying each pixel in the master image with each pixel of a complex conjugate of the slave image.(Bhattacharya et al., 2011).

$$F_1 F_2^* = |F_1| \exp(j\phi_1) |F_2| \exp(j\phi_2) = |F_1| |F_2| \exp[j(\phi_1 - \phi_2)] \quad (2)$$

F_1 and F_2 depict the pixel values of slave and master images. $\phi_1 - \phi_2$ represents the phase difference. An Interferogram shows the difference in phase in the form of fringes of an interferogram. This includes topographical, horizontal, or vertical displacements.

Coherence depicts a system where the received signals preserve phase information (Closson & Milisavljevic, 2017). It is calculated by using an interferogram and the image that represents intensity. It lacks a unit and it varies from zero to one, where one represents a high coherence (whites) and zero represents a low coherence (blacks). The process of phase unwrapping demands a coherence value of at least 0.25. Adaptive filters aid in increasing the coherence (Bhattacharya et al., 2011). $(-\pi, \pi]$ represents the interval in which the interferometric phase is measured. Phase unwrapping is the process in which the total phase is estimated from the wrapped phase by assigning a multiple of 2π to each pixel while taking into consideration the amount of wavelengths that passes through the total path length (Pellikka & Rees, 2009). The accuracy of SAR interferometry is highly dependent on phase unwrapping.

4.5 SUMMARY

In this chapter, the genesis of a glacier and the different conditions of snowpack scenarios on it are discussed. It talks about how a glacier moves and interacts with its underlying bedrock which in turn causes the movement of the same. The theory and algorithms of the various methods (Feature tracking, Interferometry) used for velocity estimation are described in detail with the depiction of relevant equations and figures. The concept of synthetic aperture radar (SAR) and how it reacts to different types of snowpack conditions is discussed briefly.

5.METHODOLOGY

This chapter describes the workflow chosen for the processes of velocity estimation using feature tracking and time series InSAR using both SAR and optical imageries. It also explains the process carried out for classifying the facies of the three glaciers.

5.1. Velocity Estimation

5.1.1 Pixel/Feature Tracking

Feature tracking is a valid replacement for calculation of surface displacement with the use of interferometric methods (Jiang et al., 2021). The algorithm can be used for both SAR and optical imagery alike (Scherler et al., 2008). The process requires a master and slave scene, where the master usually precedes the slave in terms of time. Observable features that are stationary through the entire study period is necessary for a more accurate calculation (Huang & Li, 2011). Also, the displacement must be higher than the spatial resolution of the images.

SAR feature tracking can be carried out by using coherence or intensity tracking algorithms (Frey et al., 2012). This study makes use of a more traditional pixel tracking algorithm. SARPROZ developed by Periz was used for implementing this process.

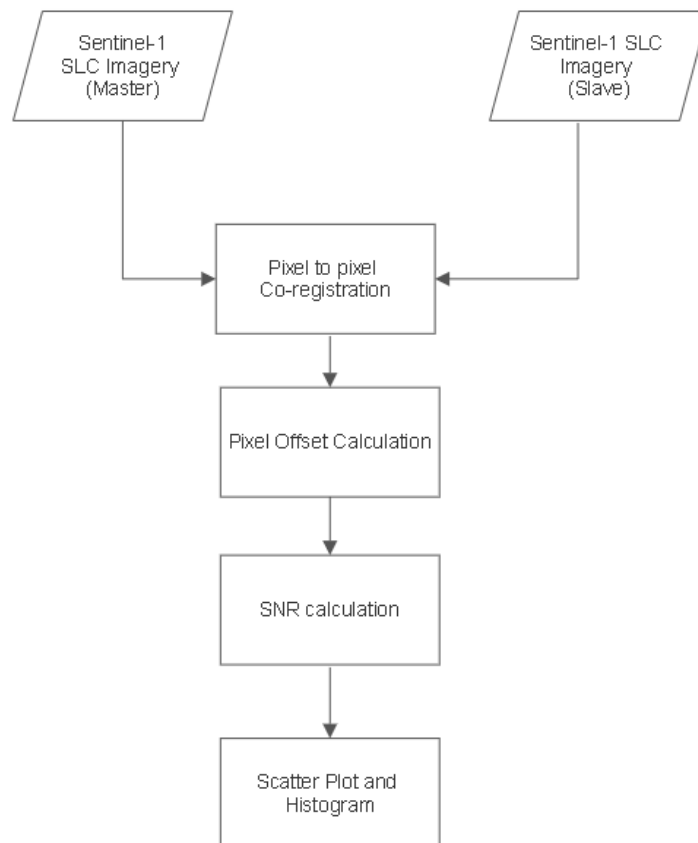


Figure 7 Workflow for pixel tracking for velocity estimation

As shown in Figure 7, two Sentinel-1 SLC imagery are co-registered with pixel-to-pixel accuracy using thousands of master reference points. The displacement of pixels is calculated over these points. Sub-pixel shifts are calculated for specific points that are chosen over the signal noise ratio and co-registration thresholds that are set by the user.

SAR feature tracking algorithm has been commonly used for velocity estimation studies in recent years. It was first successfully applied in Antarctica by (Strozzi et al., 2002). Ever since then, various work has been carried out in hope of making this algorithm more robust. When D-InSAR was affected by a scarcity of coherence, the approach proved to be effective. The method also got rid of problems related to phase unwrapping, an important step in SAR interferometry.

For optical imagery, the COSI-CORR module of ENVI was utilized for computing the surface velocity.

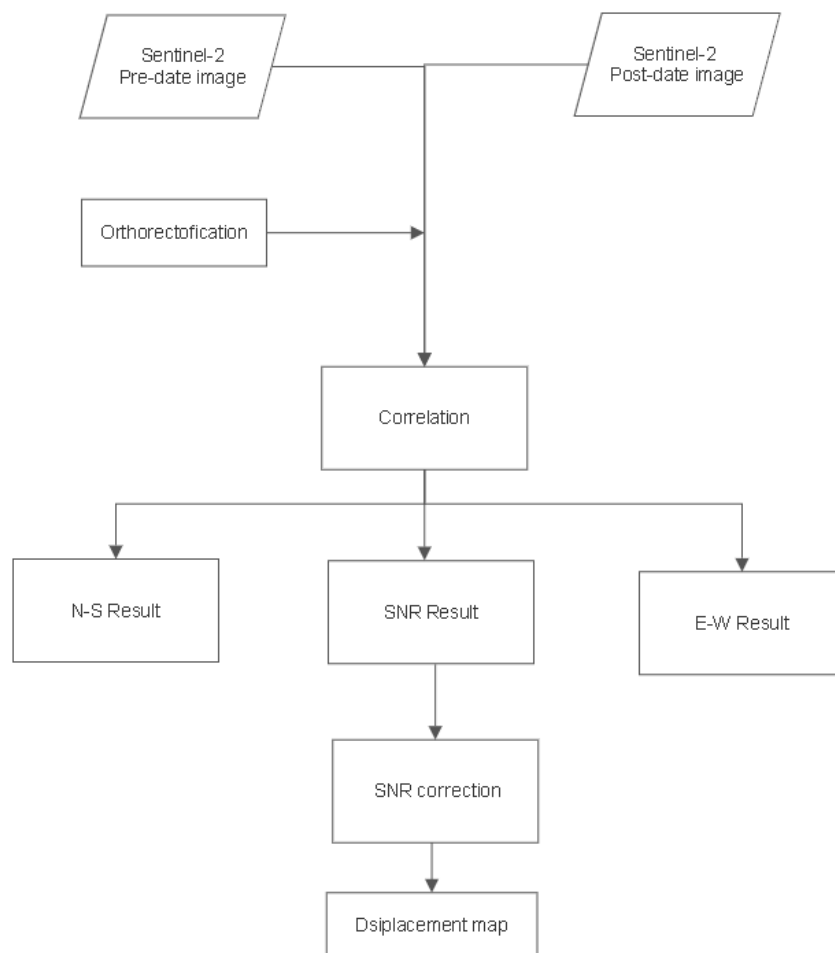


Figure 8 Workflow for feature tracking of optical imagery for velocity estimation

COSI-CORR saw its genesis back in 2008 at the tectonic observatory at Caltech (S. Leprince & Ayoub, 2009). It has since been used to compute surface displacements, changes and to monitor glaciers (Scherler

et al., 2008). A lot of studies to monitor displacement of sand dunes (Baird et al., 2019) has also been carried out. One can orthorectify, co-register and correlate satellite and aerial imagery precisely using the software. Co-registration represents the matching of pixels between the two images while correlation represents the degree of matching. The cross correlation is calculated with the help of an equation (Evans, 2000) that utilizes an image matching principle and computes phase difference in the Fourier domain to estimate correlation with a sub pixel accuracy which is given below.

$$C_{i_1, i_2}(\omega_x, \omega_y) = \frac{I_1^*(\omega_x, \omega_y) I_2(\omega_x, \omega_y)}{|I_1^*(\omega_x, \omega_y) I_2(\omega_x, \omega_y)|} = e^{j(\omega_x \Delta x + \omega_y \Delta y)} \text{ -----(3)}$$

Where, ω_x, ω_y are the variables of frequency in column and row. i_1 and i_2 represent the normalized cross spectrum of the master and slave images. I_1^*, I_2^* depict the complex conjugates. C denotes the displacement about to be computed. x and y represent the directions.

The errors pertaining to correlation are relatively higher (Scherler et al., 2008) and are eliminated by the software by using various filtering algorithms (S. Leprince & Ayoub, 2009). The output is obtained in the form of three bands which depict EW (east-west) and NS (north-south) displacements, and SNR.

Two algorithms namely frequency and statistical correlators are available for displacement calculations. This study utilizes the former. Two images that are at least one year apart are chosen to ensure that a considerable movement in the relatively slow-moving glacier is observed. This also ensures that stationary features that can be observed fall under the same glacier. The window size is the most important parameter for velocity estimation as COSI-CORR computes displacement within a window of $[2^n \times 2^n]$ pixels. The precision of the process can be increased with a larger window size, but smaller window sizes are more sensitive to minor changes on the surface. For computation, an initial window size of 128×128 and a final window size of 32×32 with a step size 2 and robustness iteration of 2 was used. A threshold of 0.9 for the SNR parameter was used for elimination of noise. The equation adopted by COSI-CORR for computing the signal to noise ratio is given below (Sébastien Leprince et al., 2007)

$$SNR^i = 1 - \frac{\sum_{\omega_x} \sum_{\omega_y} \varphi_{\Delta}^i(\omega_x, \omega_y)}{4 \sum_{\omega_x} \sum_{\omega_y} w^i(\omega_x, \omega_y)} \text{ -----(4)}$$

Where, w is a weighted matrix with positive values. φ_{Δ}^i depicts the phase difference. SNR varies from 0-1 and it quantifies the quality of correlation of the images.

The algorithm (3) in the frequency domain computes displacement in the EW and NS directions. The following formula is then used to compute the velocity and then later used for computing velocity and the velocity vector.

$\sqrt{B1^2 + B2^2}$. Where, $B1$ is the band which depicts displacement in the NS direction and $B2$ the displacement in EW direction.

5.1.2 Time Series InSAR

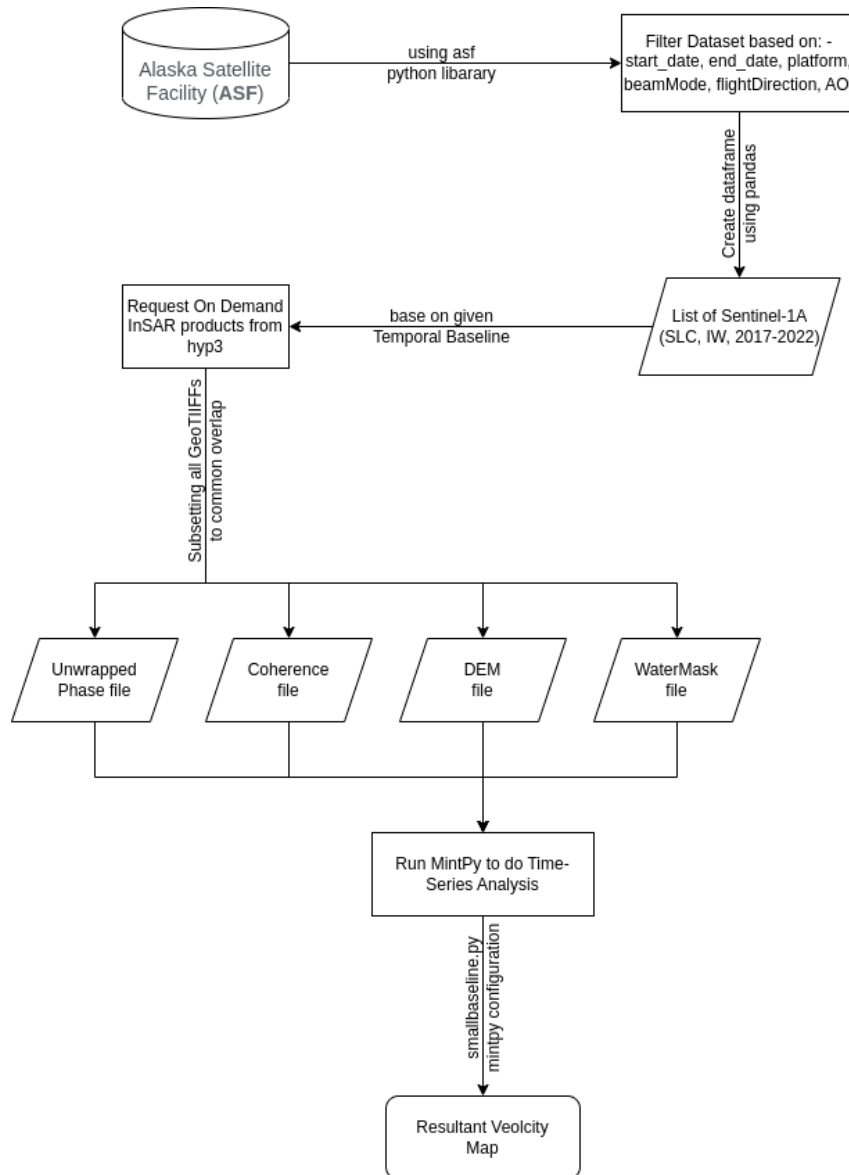


Figure 9 Workflow followed for computing velocity with Time series InSAR

A stack of Sentinel 1 imagery (SLC, IW mode) is imported from ASF to the MintPy python library. Hyp3 is an on-request service for processing Synthetic aperture radar data. This generates all the required inputs for the time series analysis process. The workflow that MintPy adopts for this process is given below.

5.1.3 Miami Time InSAR and its Workflow

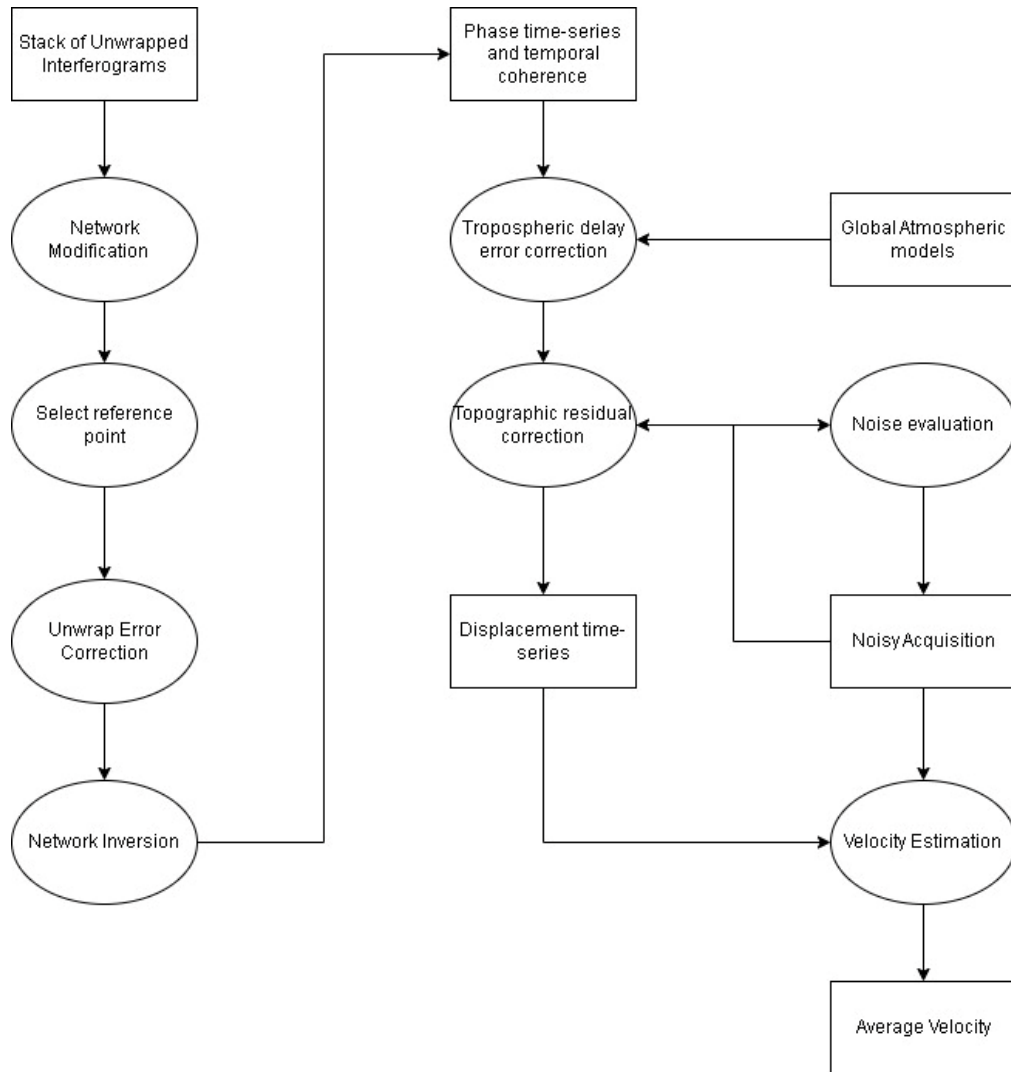


Figure 10 Routine Workflow of MintPy (Yunjun et al., 2019)

To eliminate the limitations caused by long revisit time and large orbit separation, two InSAR techniques namely persistent scatterer and distributed scatterer. The former has its applications limited to manmade structures (Hooper et al., 2004) while the latter is used for finding displacement and deformations on the land surface. MintPy utilizes the distributed scatterer method to use a stack of small baseline (in the temporal and spatial scale) interferograms. This method is also known as SBAS (Small baseline subsets) (Schmidt & Bürgmann, 2003)

The Miami Time InSAR (MintPy) (Yunjun et al., 2019) used in the study, is an open-source package meant for interferometric time series analysis. It reads already co-registered and unwrapped interferograms from various sources like ISCE, SNAP etc. and computes the 3D surface displacement in the LOS direction. It

computes the phase closure, unwrapping errors, corrects tropospheric delays using global atmospheric models, removes phase ramps and rectifies DEM errors while doing so.

As mentioned above, the process starts by reading interferograms from ASF, ISCE, GAMMA etc. (Rosen et al., 2004)(Werner et al., 2000) that are rectified for the curvature of earth and topographical errors. The spatially averaged coherence for the study area is calculated and is compared with a user defined threshold value. This is done to eliminate outlier interferograms that are affected by coherent pixels that are related to unwrapping errors. A reference pixel is then chosen which has a high spatial coherence of above 0.85. The selected pixel should be devoid of atmospheric turbulence and ionospheric streaks. It should also have minimal correlated atmospheric delay (Yunjun et al., 2019).

Unwrapping errors occurs when the phase time series is affected by faulty integer numbers of cycles. This errors pertains to the interferometric phase during the 2D phase wrapping where the raw phase time series is biased by faulty integer numbers (Yunjun et al., 2019). This is rectified by bridging of reliable regions where the pixels are free of relative local unwrapping errors (Chen & Zebker, 2002). These regions have a high spatial coherence and are separated from each other due to decorrelation.

The interferometric phase residual $\Delta\varphi_e$ is minimized for solving the raw phase time-series. The temporal coherence is calculated with the equation (Yunjun et al., 2019)

$$\gamma_{temp} = 1/M | \mathbf{H}^T \exp[j(\Delta\psi - \mathcal{A}\psi^*)] | \quad (5)$$

Where, M is the number of interferograms that are co-registered to a common SAR sensed image. j is an Imaginary unit, H is an $M \times 1$ vector, T denotes time, ψ^* represents the raw phase time series, \mathcal{A} represents a full rank design matrix. $\Delta\psi$ is an interferometric phase vector.

The tropospheric delay is corrected by utilizing a global atmospheric model. It is given in radians with the equation (Yunjun et al., 2019)

$$\varphi_{tropo}^i(p) = (\delta L_p^i - \delta L_p^{i1}) \frac{4\pi}{\gamma} - (\delta L_{ref}^i - \delta L_{ref}^{i1}) \frac{4\pi}{\gamma} \quad (6)$$

Where, δL_p^i depicts the Tropospheric delay at t_i on the pixels that are x meters in the satellite LOS γ – Wavelength in m; p represents the pixel.

The phase deramping process is then performed to minimize the remaining tropospheric and ionospheric delays caused by orbital errors. The DEM error pertaining to that of topographic phase residual is computed by considering the proportionality of the perpendicular baseline time series (Fattahi & Amelung, 2013). This error is given by the formula (Hetland et al., 2012)

$$\varphi^i - \varphi_{tropo}^i = \left(\frac{B_t}{r \sin \theta} z_e + \frac{\sum_{k=0}^{n_{poly}} c_k (t_1 - t_i)^k}{k!} \right) + \sum_{1 \in 1x} S_1 H(t_1 - t_i) \frac{-4\pi}{\gamma} + \varphi_{resid}^i \quad (7)$$

Where,

B_t represents the perpendicular baseline between t_i and t_1 , r , the slant range between target and radar antenna, θ depicts the incidence angle. $H(t_1 - t_i)$ is a step function. z_e , C_k , S_1 are the unknown parameters. φ_{tropo}^i represents the contribution of phase due to propagation delay caused by the troposphere. φ_{resid}^i is the residual phase at t_1 for pixel p .

The noise pertaining to InSAR time series is characterized by the phase component that cannot be rectified or characterized as deformations in the ground (Yunjun et al., 2019). The RMS of this residual phase is given by,

$$RMS = \sqrt{\frac{1}{N\omega} \sum_{p \in \omega} (\varphi_{resid}^i(p) \cdot \frac{\gamma}{-4\pi})^2} \text{---(8)}$$

Where, $i = (1 \dots N)$; ω is the set of pixels that are reliable in terms of temporal coherence. $N\omega$ is the total number of such pixels.

Once all the corrections have been successfully applied, the software calculates velocity v . It is computed as the best fit between displacement time series and slope line, given by,

$$\varphi_{dis}^i \cdot \lambda / (-4\pi) = v \cdot t_i + c; i = 1, N \text{---(9)}$$

Where, C is an offset constant. The velocity is obtained as an average for the years (m/year) 2017-2022 and is represented in the form of maps.

5.2 Glacier Facies Classification

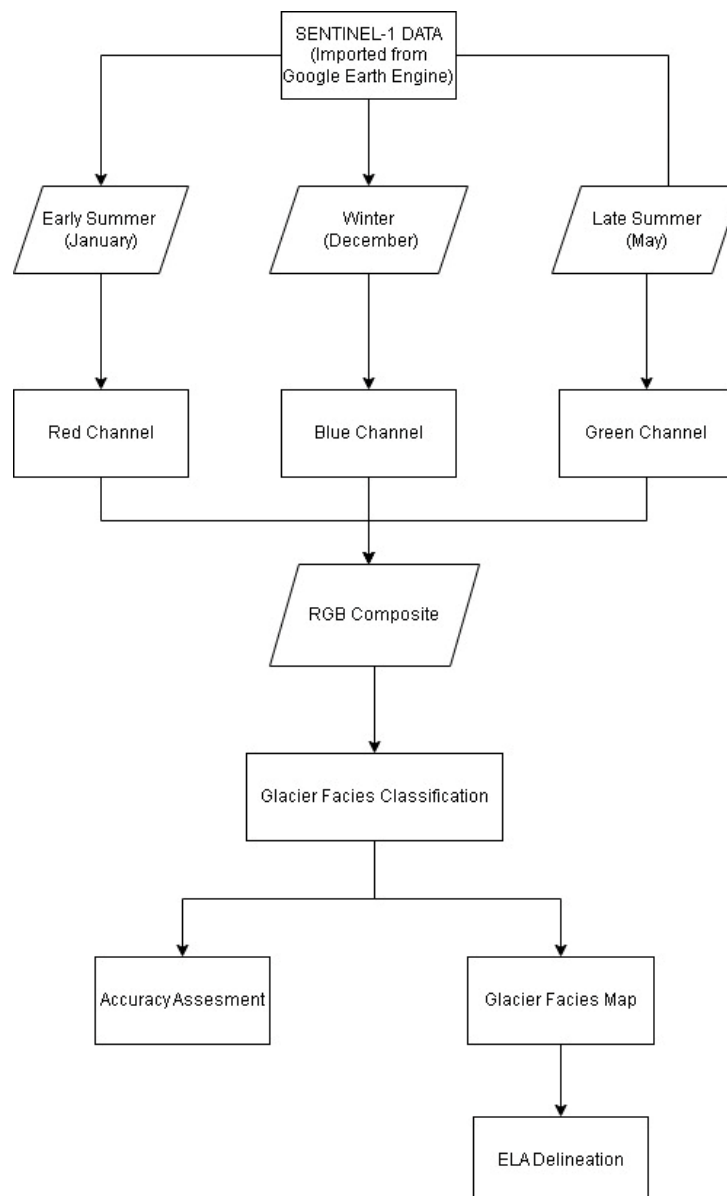


Figure 11 Workflow adopted for glacier facies classification

This process requires three images from different seasons (Early summer, late summer, and winter). The images were acquired from google earth engine. The downloaded images come pre-processed for orbital correction, calibration, and Terrain correction (Using SRTM 30m DEM). The images are chosen in such a way that the effect of westerlies on the glacier's onset of melting is considered (Bookhagen & Burbank, 2010) for early summer. Unseasonal precipitation on the Himalayan glaciers (Shrestha & Aryal, 2011), can affect the backscatter properties leading to an inaccurate classification result (Vijay Mahagaonkar, 2019). Hence, this phenomenon should also be considered while acquisition.

The images are dual polarized (VV+VH). Although Quad polarized data would give an easier interpretation of the complex glacier structure, it could not be used as the data is still limited across the Indian Himalayas. VV polarized information is used for this whole process as it is more sensitive (Vijay Mahagaonkar, 2019).

The images are then passed through different channels for creating an RGB composite image. Blue channel for winter, red channel for early summer and green channel for late summer (Partington, 1998b). The different facies of the glacier are depicted by different backscatter properties, and they exhibit a characteristic colour for each glacier zone as given in the table below.

Glacial Facies	Seasonal Characteristics			Appearance in RGB Composite
	Winter (Blue)	Early Summer (Red)	Late Summer (Green)	
Upper Percolation	Dry snow High	Dry snow High	Dry snow melting Slightly Higher	Greenish \White
	Middle Percolation	Dry snow melting High	Melting Snow LOW	
Lower Percolation	Dry snow melting High	Firn exposed Low	Firn melting Low	Blue
	Bare Ice	Ice melting Low	Excessive Ice Melting Low	
Debris Covered Ice	Debris	Debris	Debris	Light Grey

Table 2 Appearance of each glacier zone and their level of backscatter intensity (Partington, 1998)

The Necessary region of interest polygons are created for training the points and are later classified using a random forest classifier. Random forest is chosen due to its robust nature (Jehad Ali, 2012) and has proven to be an accurate algorithm for glacier classification and mapping (Nijhawan et al., 2018)(Wangchuk & Bolch, 2020)(Lu et al., 2022). Accuracy Assessment is performed after the process to evaluate the quality of classification. Using this information, a confusion matrix depicting the accuracy of user and producer is given.

The Equilibrium line altitude (ELA) is the line that separates the accumulation zone and ablation zone. After the classification of these zones, the ELA can be manually digitized using a GIS tool for each year. This in turn would give us a knowledge of if the glacier is gaining mass or if it is receding.

5.2.1 Random Forest Classifier

The random forest (RF) classifier comprises of many individual decision trees that work together to generate a more accurate result when compared to an individual tree (Breiman, 2001). Due to random selection of data, the variance is less biased and obtains the most information while creating numerous trees and dividing nodes (F. Pedregosa FABIANPEDREGOSA et al., 2011). A few past studies applied this algorithm for glacier mapping that proved to be successful. (Wangchuk & Bolch, 2020) mapped glacial lakes using sentinel data and an RF classifier, (Lu et al., 2020) mapped the glacier over the eastern Pamir using an algorithm based on a RF classifier, (Khan et al., 2020) mapped debris covered glaciers using various ML algorithms and concluded that the RF classifier has a higher accuracy of 95% as opposed to support vector machines and ANN (Artificial Neural network) that has an accuracy of 92.05 and 91.86% respectively.

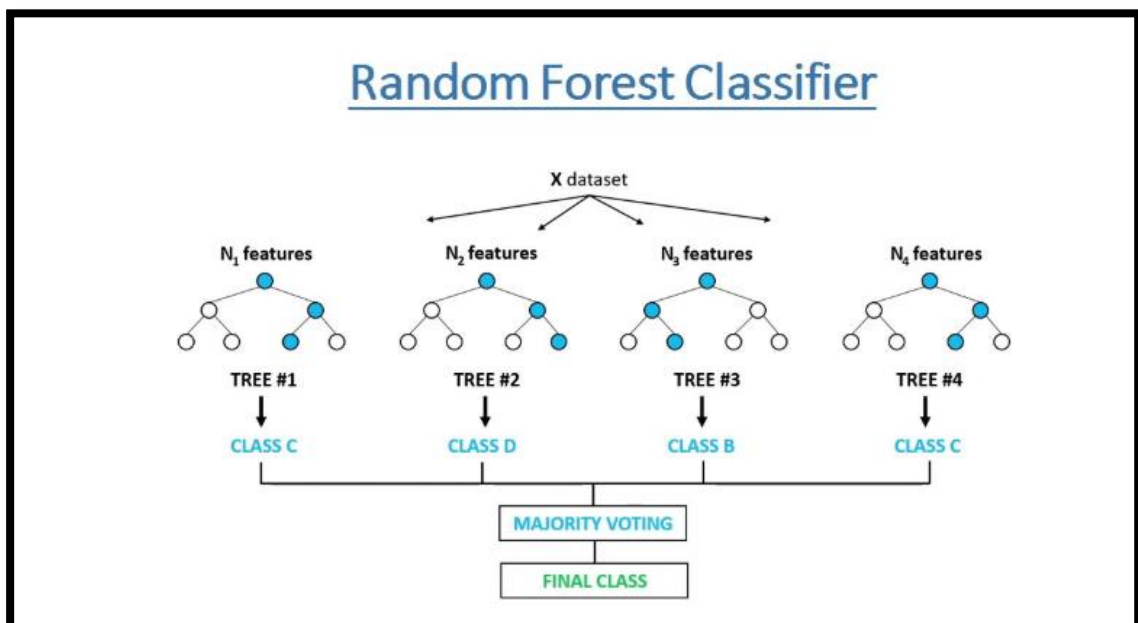


Figure 12 Working of a Random Forest Classifier (Davis David, 2020)

The selected samples are called as in-bag samples, are used to train trees while the remaining samples called as Out-of-bag (OOB) samples are used for cross validating the performance of the model. The algorithm generates decision trees for each sample selected. Voting for every predicted result is performed using mode. Averaging the forecasts of each individual tree results in the final predictions of the RF.

6. MATERIALS

6.1 Study Area

The Chandra basin that houses all the glaciers of interest . The Study areas chosen for this project are of the Bada Shigri, Gepang Gath and Chotta Shigri glaciers over the basin. It attracts a sizeable number of tourists and is the home for places like Chandra Tal and other populated villages like Koksar, Sissu etc.

The basin is located in the Lahaul–Spiti district, western Himalaya, India as depicted in Figure 1. The basin occupies an area of $2.44 \times 10^3 \text{ km}^2$ with elevations varying from 2887 to 6547 meters from sea level. The basin contains 703.64 km^2 of glaciated area, which translates to thirty percent of the total area (Sangewar, 2009).The basin houses 201 glaciers. These glaciers flow into the Chandra River (depicted with a blue line in figure1) which is a big tributary to Chenab River which flows through major and minor cities of both India and Pakistan. The region is defined by towering mountains and sharply dissected valleys, it is extremely rough and inaccessible (P. Sharma et al., 2013). Heavy and dry precipitation, low temperatures, and significant wind patterns define the basin. (S. S. Sharma & Ganju, 2000).

(Bookhagen & Burbank, 2010). Heavy precipitation is observed in the months of July and September (Summer) and in the winter due to westerlies (P. Sharma et al., 2013). This multi seasonal rainfall behaviour puts the dams downstream at risk.

All glacier boundaries were marked with the help of Randolph glacier inventory (V.6.0) (RGI Consortium, 2017)

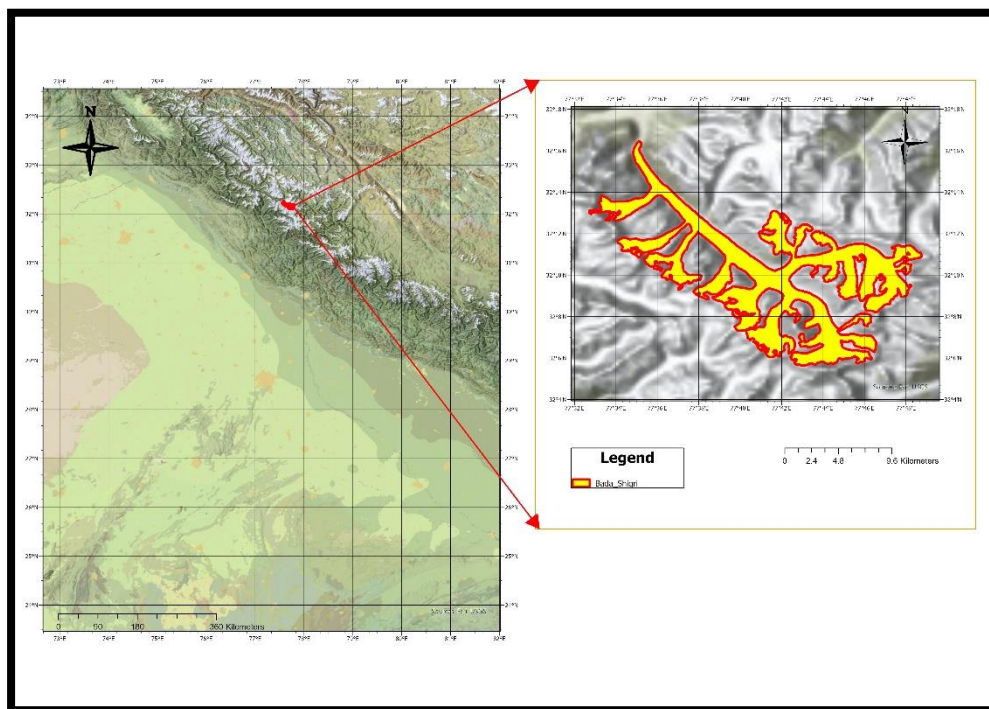


Figure 13 Map showing the Study area of Bada Shigri glacier.

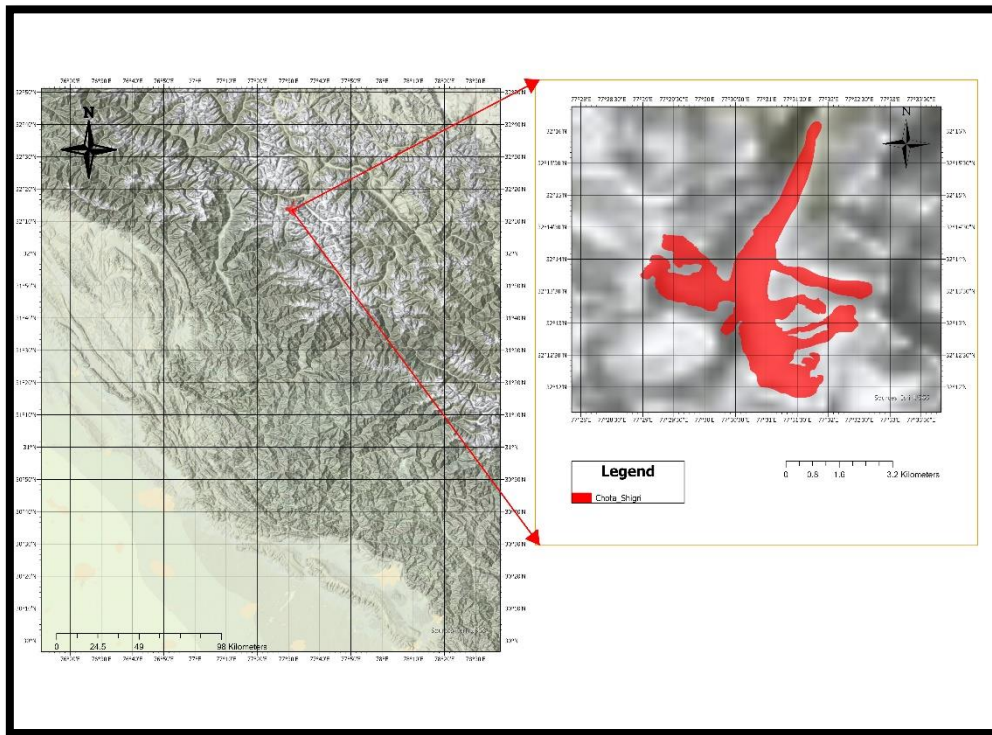


Figure 14 Figure showing the study area of Chota Shigri glacier [you have two figure 15]

Figure 15 depicts the location of CS glacier. Chhota Shigri glacier resides on the northern slopes of the Pir Panjal range in western Himalayas, it is a valley-type glacier and exists in a north to south orientation in the ablation zone and a varying range of orientations in the accumulation zone. It has three main trunks that has a 3% coverage of debris (Azam et al., 2016). The glacial basin occupies an area of 15.7 km². Small scale meteorological observations in the late summer season on the glacier showed temperatures from -5.2 to +10.5 Celsius at an elevation of 4600m from msl (Dobhal et al., 1995). The equilibrium line altitude (ELA) varied between 4900 msl to 5200 msl from 2002 to 2014 (Berthier et al., 2007). The debris cover usually varies between 30-40cm (Sanchayita Das & Chakraborty, 2019)

Figure 14 depicts the location of BS glacier..Bada Shigri glacier is the largest glacier in the basin which occupies an area of 136 km². The length of the glacier is about 30 kms (Dobhal et al., 1995). The elevation of the snout of the glacier is at about 4000 msl (Anil V Kulkarni et al., 2006)

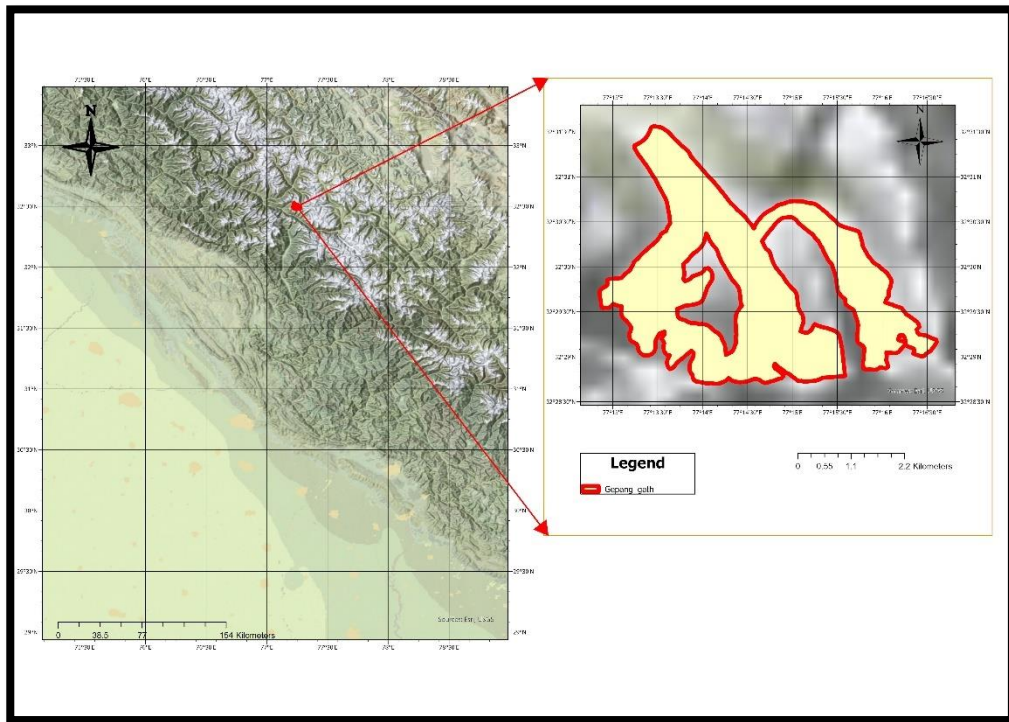


Figure 15 Study Area of Gepang Gath glacier

Gepang gath, displayed in figure 16, lies in the western Himalayan middle climatic zone. Hence, it depicts cold weather conditions. It has an area of 12.26.km² and its elevation varies from 3500 to 5300 msl (S. S. Sharma & Ganju, 2000).

Just like the case with other Himalayan glaciers, all the glaciers have a heavy cover of debris which hides ice for most of its stretches(Yellala et al., 2019a).

6.2 Datasets used

(i)Sentinel 1 SAR (European Space Agency,2018) – The Sentinel 1, launched by the European space agency, disseminates data at 5.405 GHz through a dual polarization C-band synthetic aperture radar device (C band). The mission consists of two polar orbiting satellites which operates at all weather conditions. It follows a near-polar sun synchronous orbit that revisits a point every 12 days. Sentinel 1-A and Sentinel-1B which give SAR coverage on a worldwide scale and on a 6-day repeat cycle when used together. They both have the same orbital plane with an 180° orbital phasing difference The sentinel GRD offers three resolutions at 10, 25 and 40 meters with four band combinations (VV +VH and HH + HV). The sentinel-1 IW swath mode in dual polarization mode (VV+VH) has become the standard imaging mode over complex terrains like mountains (Snapir et al., 2019)

(ii)Sentinel 2- The Copernicus sentinel-2 mission comprises of two satellites flying in the same orbit but phased in 180°, is designed to give an excellent temporal resolution of 5 days at the equator with a swath width of 290kms. It carries an optical instrument that transmits 12 spectral band, four bands at 10m, six bands at 20m and three bands at 60m spatial resolution.

The glaciers were classified using Sentinel 1-b GRD data in VV polarisation, that was sensed in descending pass of the satellite. The specific datasets used for each process is given below: -

Glacier	Year	Date of acquisition
Chota Shigri Glacier	2019	21-08
	2020	15-08
	2021	22-08
	2022	09-08
Bada Shigri Glacier	2019	21-08
	2020	15-08
	2021	22-08
	2022	09-08
Gangotri Glacier	2019	05-08
	2020	10-08
	2021	13-08
	2022	17-08

Table 3 Dataset used for polarimetric classification

Glacier	Year	Dataset used for classification		
		Winter	Early Summer	Late Summer
Chota Shigri Glacier	2020	08-Jan	31-May	11-Sep
	2021	03-Jan	28-May	30-Aug
	2022	28-Dec	06-May	05-Sep
Bada Shigri Glacier	2020	08-Jan	29-May	29-Aug
	2021	04-Jan	05-May	29-Aug
	2022	09-Jan	07-May	13-Sep
Gangotri Glacier	2020	17-Jan	11-Apr	23-Sep
	2021	22-Dec	29-Apr	19-Sep
	2022	08-Jan	13-May	15-Sep

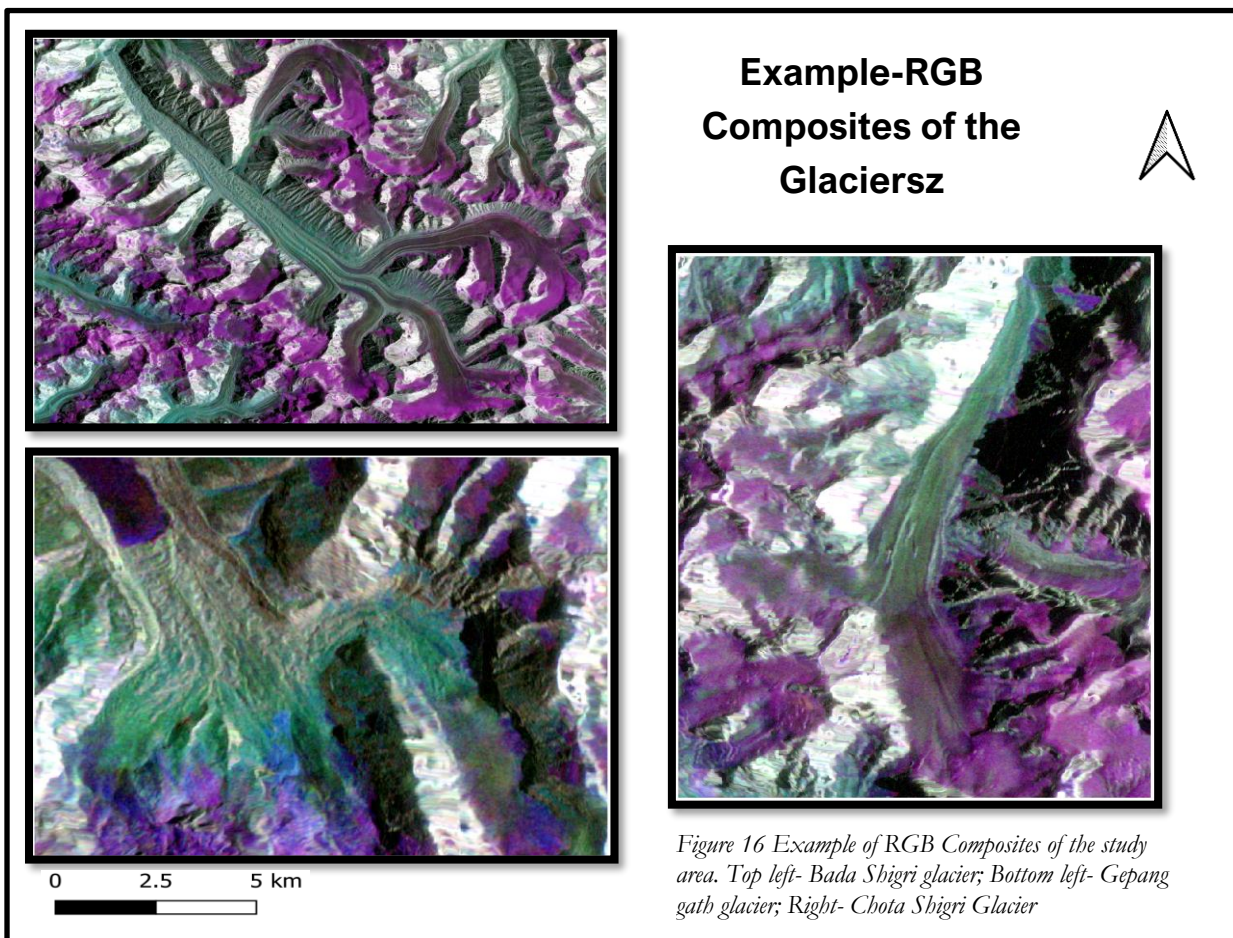
Table 4 Dataset used for Optical feature tracking and SAR pixel tracking

(iii) ALOS-PALSAR- ALOS-PALSAR is a satellite mission initiated by JAXA. The high-resolution DEM (12.5m) provided by the same was used for creation of elevation maps for the glaciers

7. RESULTS

7.1 Glacier Facies Classification

The glaciers were classified using Sentinel 1-b GRD data in VV polarisation, that was sensed in descending pass of the satellite. The dates used for classification is given in section 5.2. As mentioned in section 6.2, RGB composites of the three glaciers are created using one image of early summer, late summer, and winter each for the years 2020, 2021 and 2022. A total of 27 images are used to create 9 composites.



The glaciers are classified by exploiting the difference in backscatter intensities of the SAR signals which leads to each glacial zone exhibiting their own characteristic colour as given in figure 7.

A random forest classifier is used for classification. This was carried out with the help of Python sklearn library for machine learning algorithms.

As mentioned in section 2.2.1, a tree comprises of various nodes. The nodes are chosen in a way that an optimal split of the features occur. There are various functions that can be utilized for measuring the quality of the split. The classifier used in this study uses entropy over the Gini Index for measuring the disorder of features with the target (Pablo Anzar, 2020). The entropy is computed with the following equation (G. V. Pedregosa FABIANPEDREGOSA, 2011)

$$\text{Entropy} = -\sum p_j \cdot \log_2 p_j \quad (10)$$

In equation (10), p_j is the probability of class j . The graphs obtained after hyperparameter tuning of the RF model are given below,

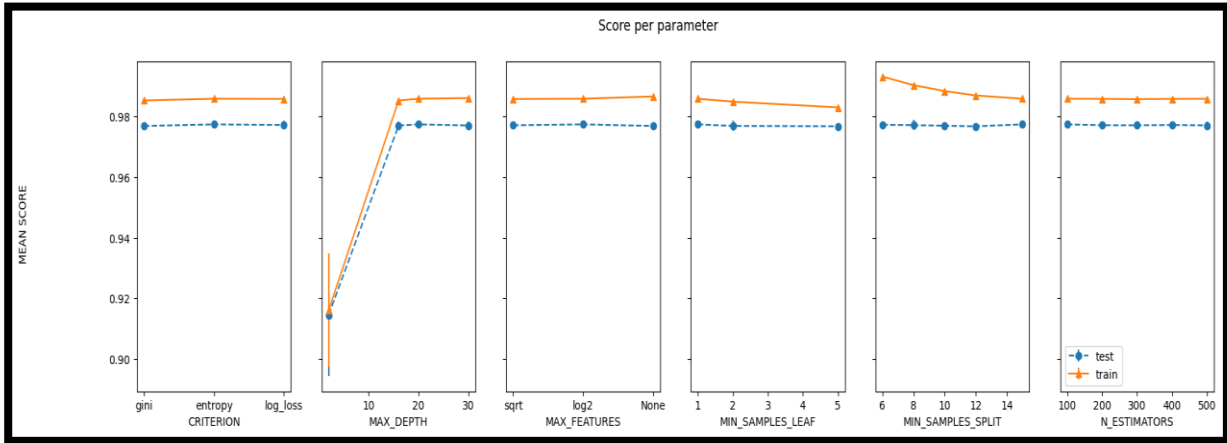


Figure 17 Graphs of mean score of each parameter of RF classifier

The hyper tuning was done using different combinations of parameters to achieve an optimal performance model. The estimator returned a set of parametric values for the best fit and for an accurate model. A total of 66158 pixels for each RGB composite was created where a random split of 80% of the samples were used for training and a 20% of the samples were used for testing. The maximum depth of the tree was set at 20 as it can be seen from Figure 18 that the training line and testing line could be overfitting. The number of features considered while looking for best split was set at log2. The minimum number of samples to be split at the internal node is given as 15. As it can be seen in Figure 8, any value (of minimum number of samples) less than 15 could be underfitting. The minimum required samples needed at node was set 1 as the testing and training line seem to be converging for values lesser than 1, indicating a scenario of overfitting. The number of trees was set at 100 for an optimal performance of the model. The out of bag accuracy of prediction model was found to be 97.73%, which indicates that the model's performance is good. The different bands of the image in this scenario translates to different seasons of the year. The importance of band 1, band 2 and band 3 was found to be 0.27, 0.41 and 0.31 respectively. This indicates that all bands were given a relatively equal importance.

The error matrix returned by the model for the classification process is given in section 7.4.1. The classified maps of Bada shigri, Chota Shigri and Gepang gath glaciers are given in sections 7.1.1, 7.1.2 and 7.1.3 respectively.

7.1.1. Bada Shigri Glacier

The classified maps for Bada Shigri glacier for the years 2020, 2021 and 2022 are given below-

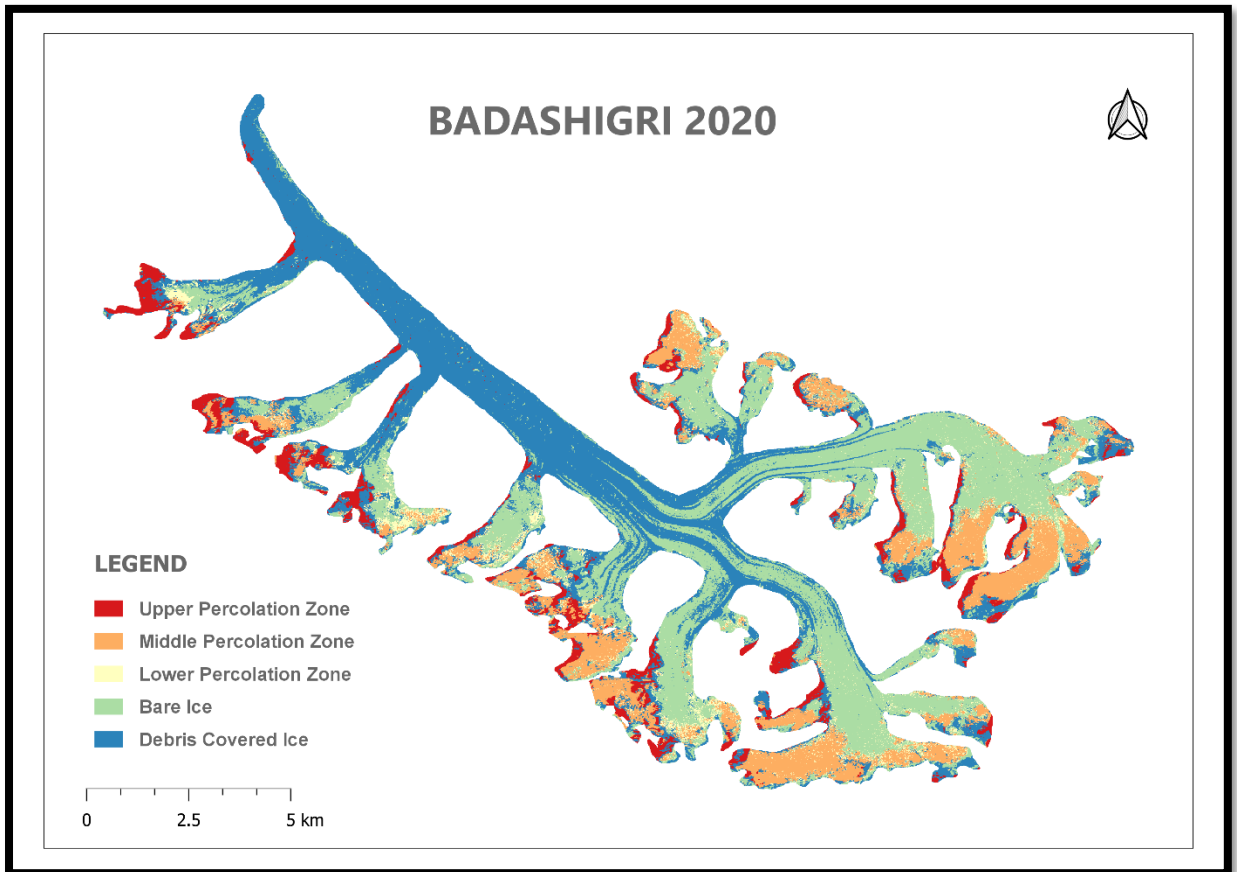


Figure 18 Bada Shigri Glacier Classified Map

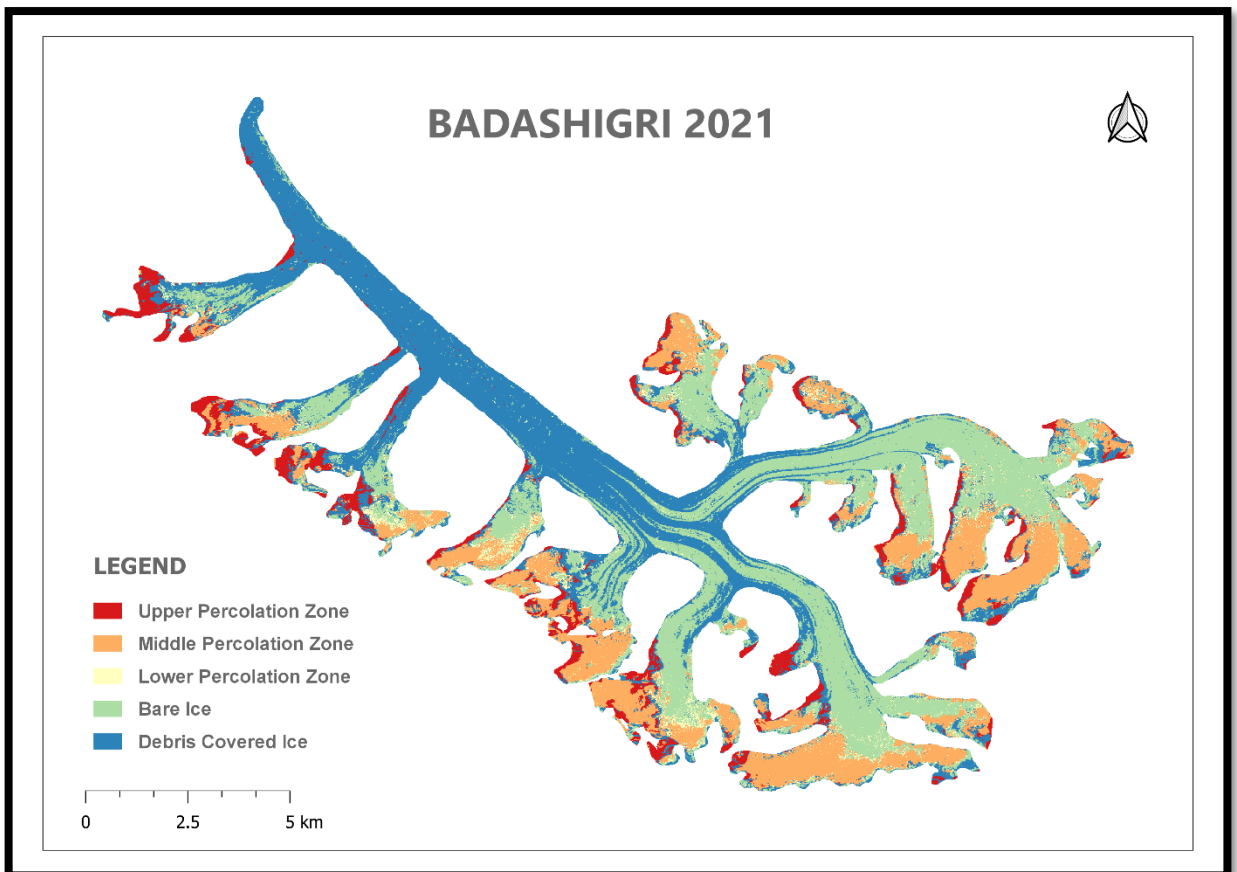


Figure 19 Bada Shigri Glacier Classified map- 2021

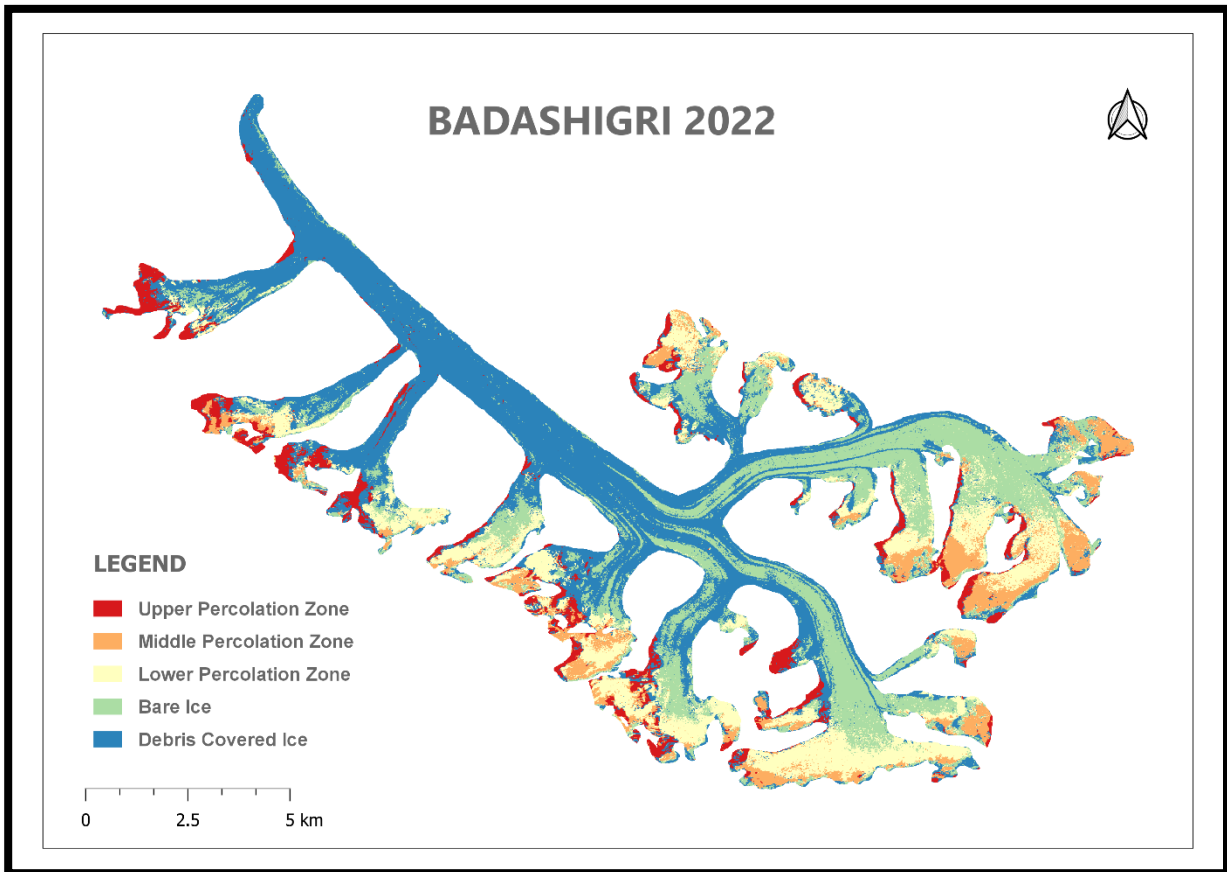


Figure 20 Bada Shigri Glacier Classified map 2022

As bada shigri is a big glacier with a length of 40 Kms, the different zones are easily interpretable. The glaciers in this region of the Indian Himalayas have very little to no upper percolation zone due to the onset of melting of dry snow in the early summer. An absence of the lower percolation zone could be observed in the mid-summer image, due to excessive melting as the temperature rises. From the classified result, it can clearly be seen that majority of the glacier is covered with ice covered with debris and bare ice. The areas of different zones are quantified in table 8..

7.1.2 Chota Shigri Glacier

The classified maps for Chota Shigri glacier for the years of 2020,2021 and 2022 are given below-

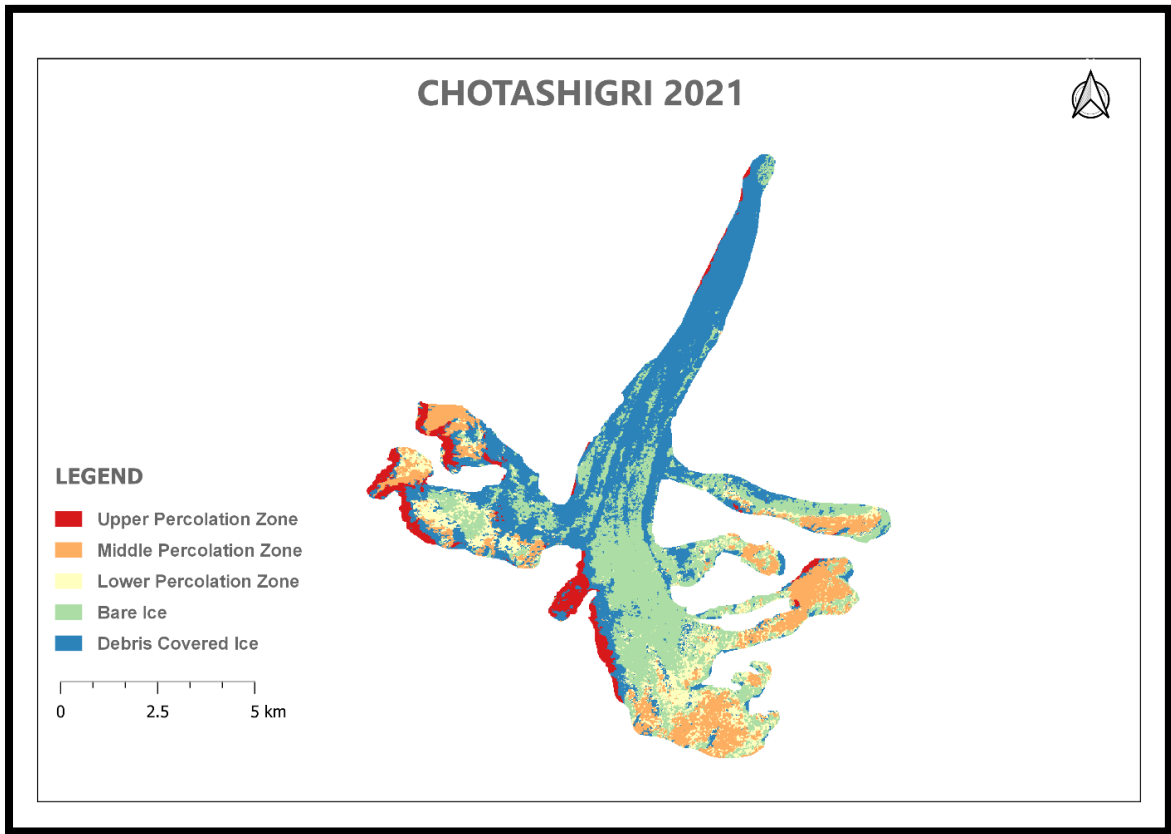


Figure 21 Chota Shigri Glacier Classified Map- 2021

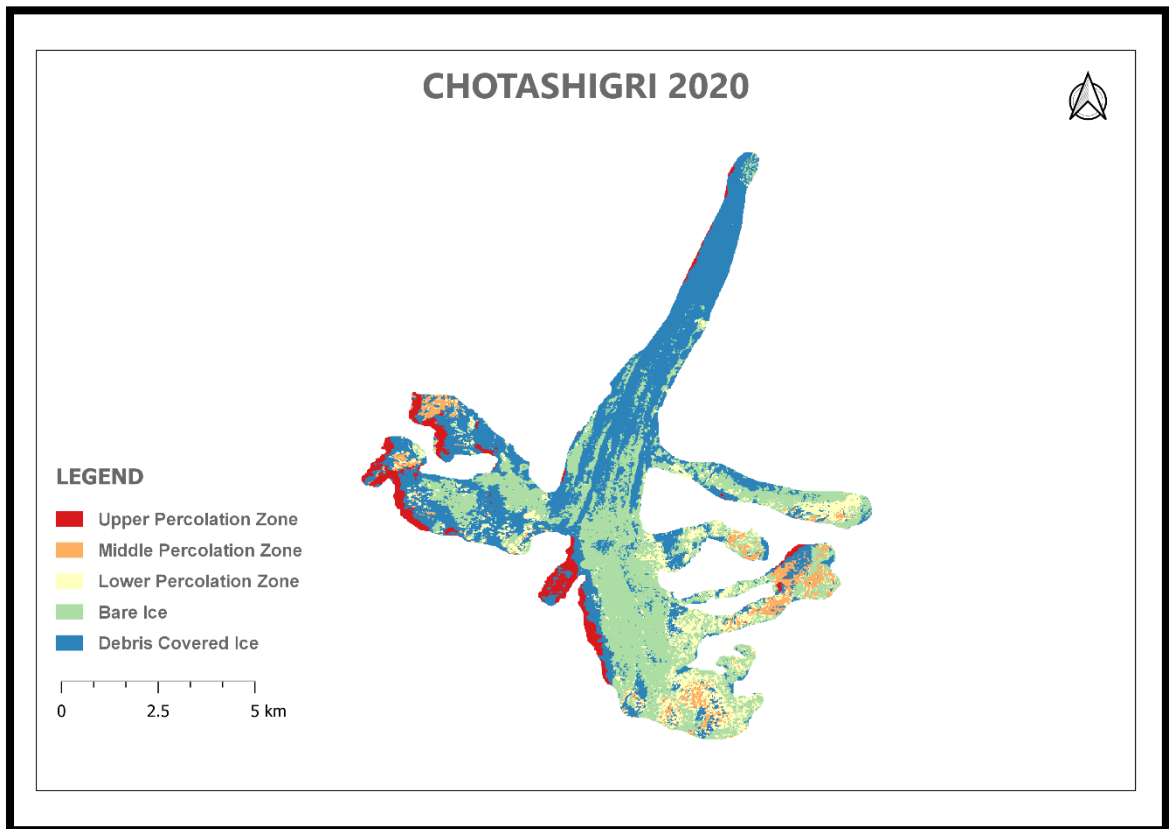


Figure 22 Chota Shigri Glacier Classified Map- 2020

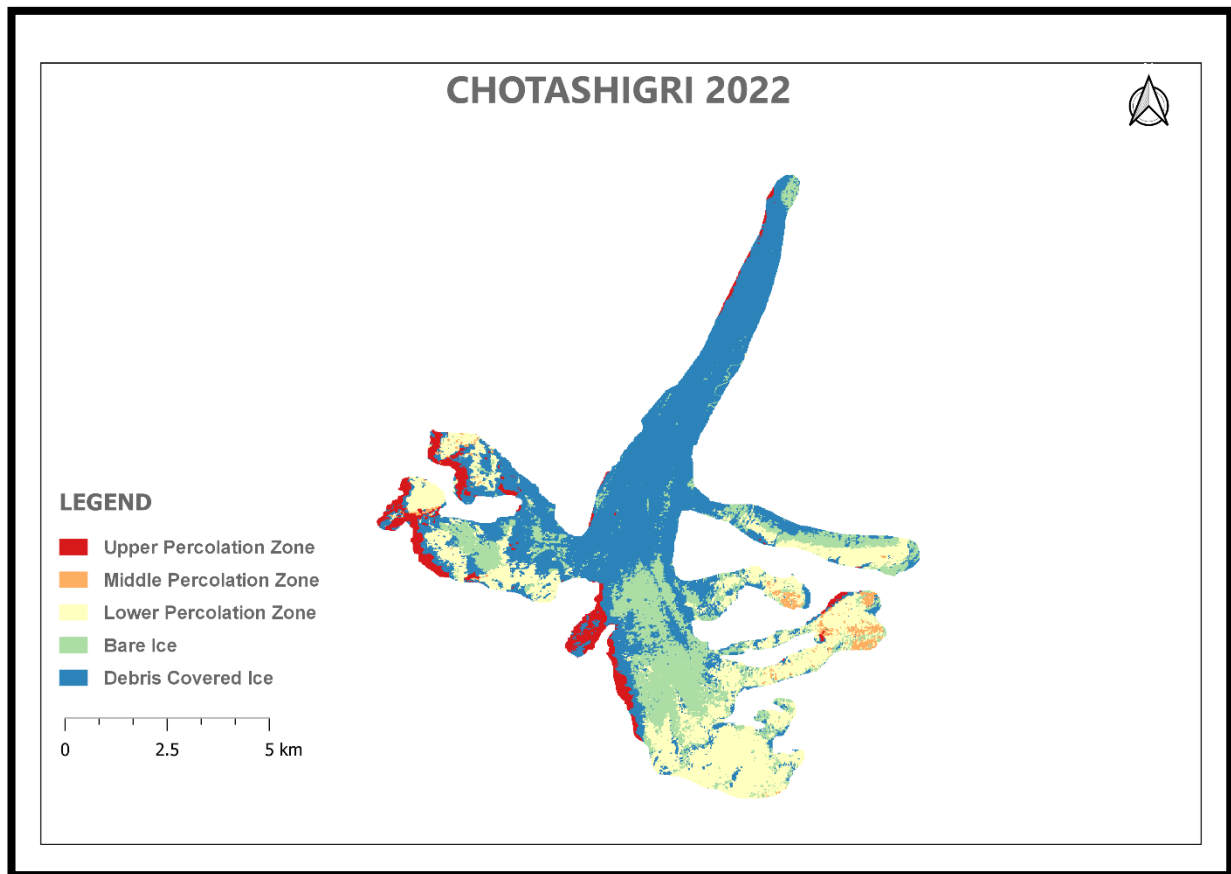


Figure 23 Chota Shigri Glacier Classified Map- 2022

The area of debris covered ice presides all the other zones of Chota Shigri glacier. The observed ablation zone is covered with debris which is a typical characteristic of Himalayan glaciers in this region. As the glacier is in a geographical proximity with Bada shigri glacier, the weather patterns are similar. Hence, the upper percolation zone is minimal in terms of area and an absence of lower and middle percolation zone was observed in the summer seasons due to ablation. The area for each zone is given in table 9

7.1.3 Gepang Gath Glacier

The classified maps for Gepang Gath glacier for the years of 2020,2021 and 2022 are given below-

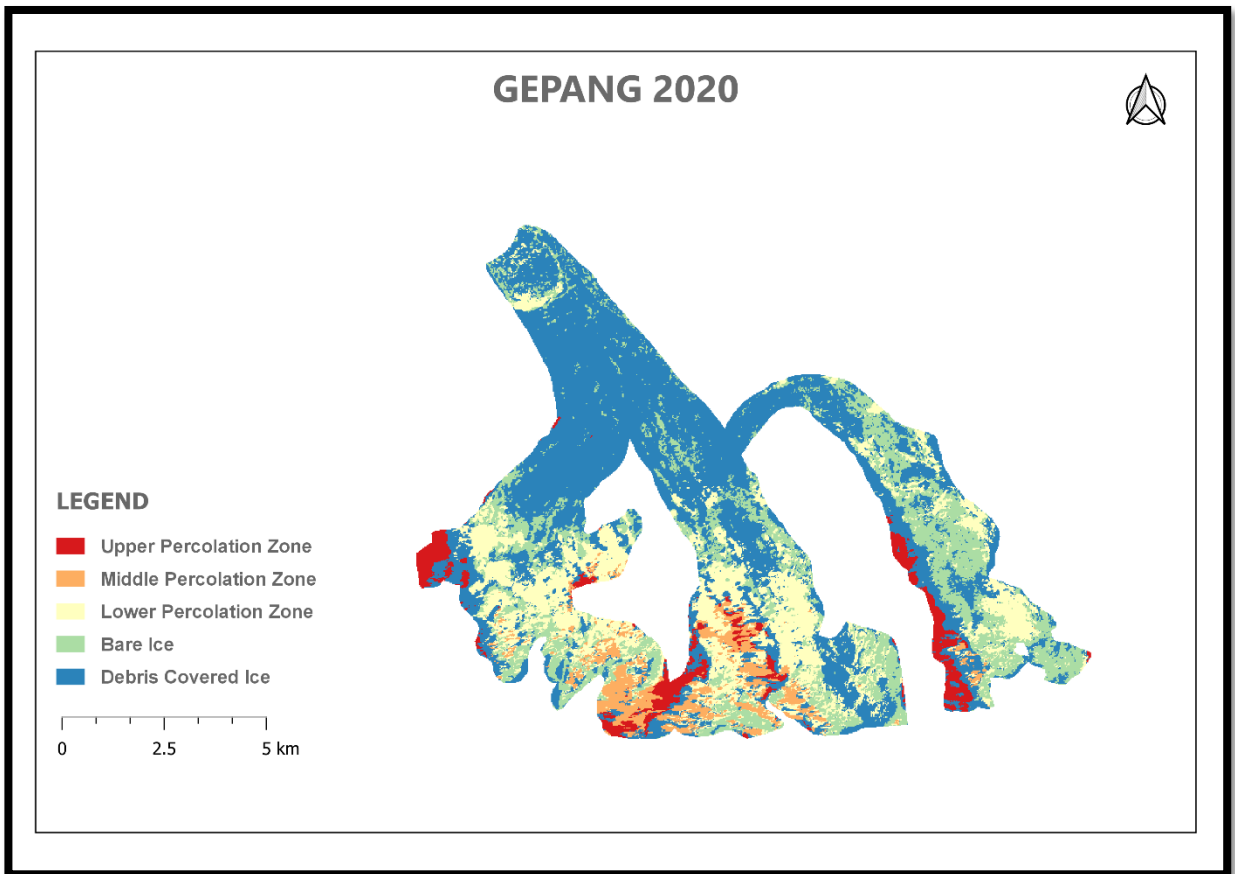


Figure 24 Gepang Glacier Classified Map- 2020

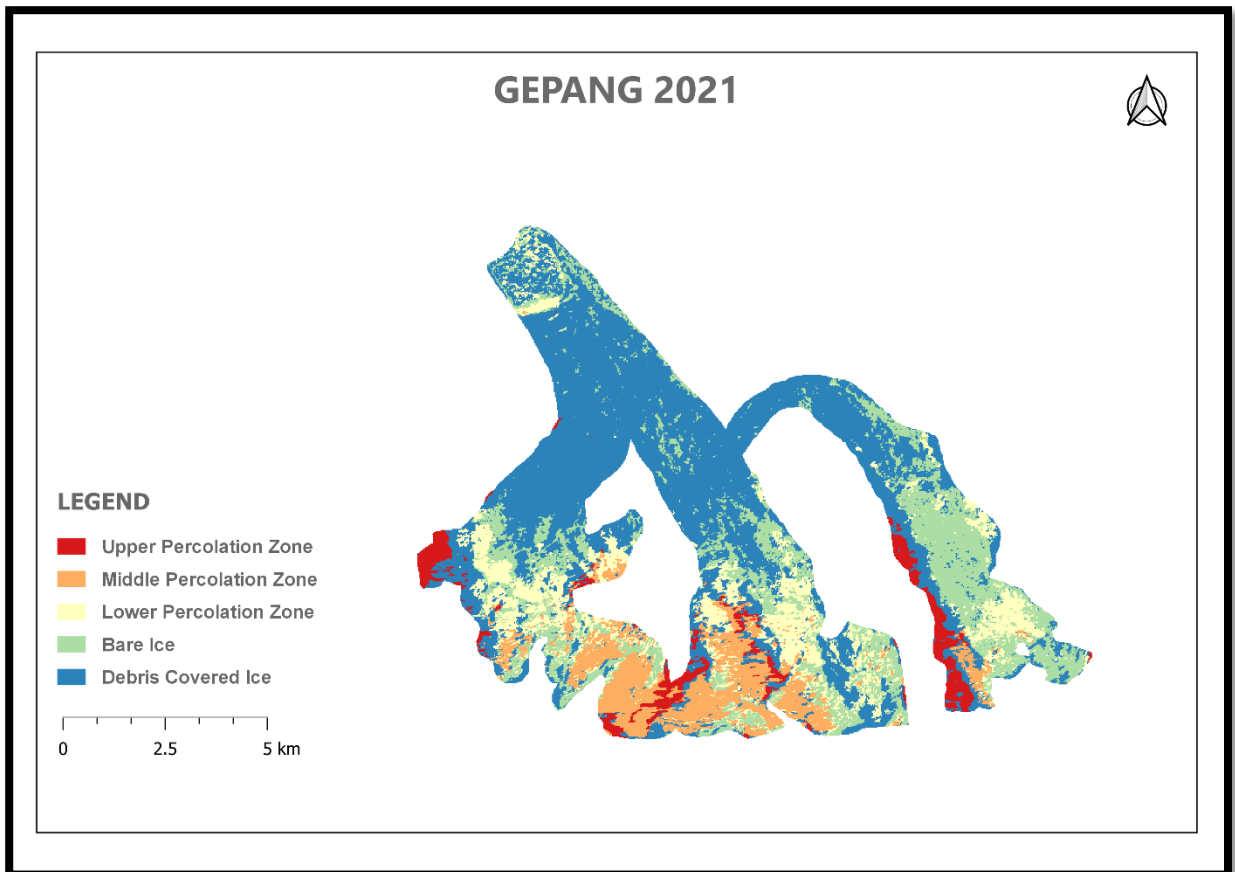


Figure 25 Gepang Gath Glacier Classified Map- 2021

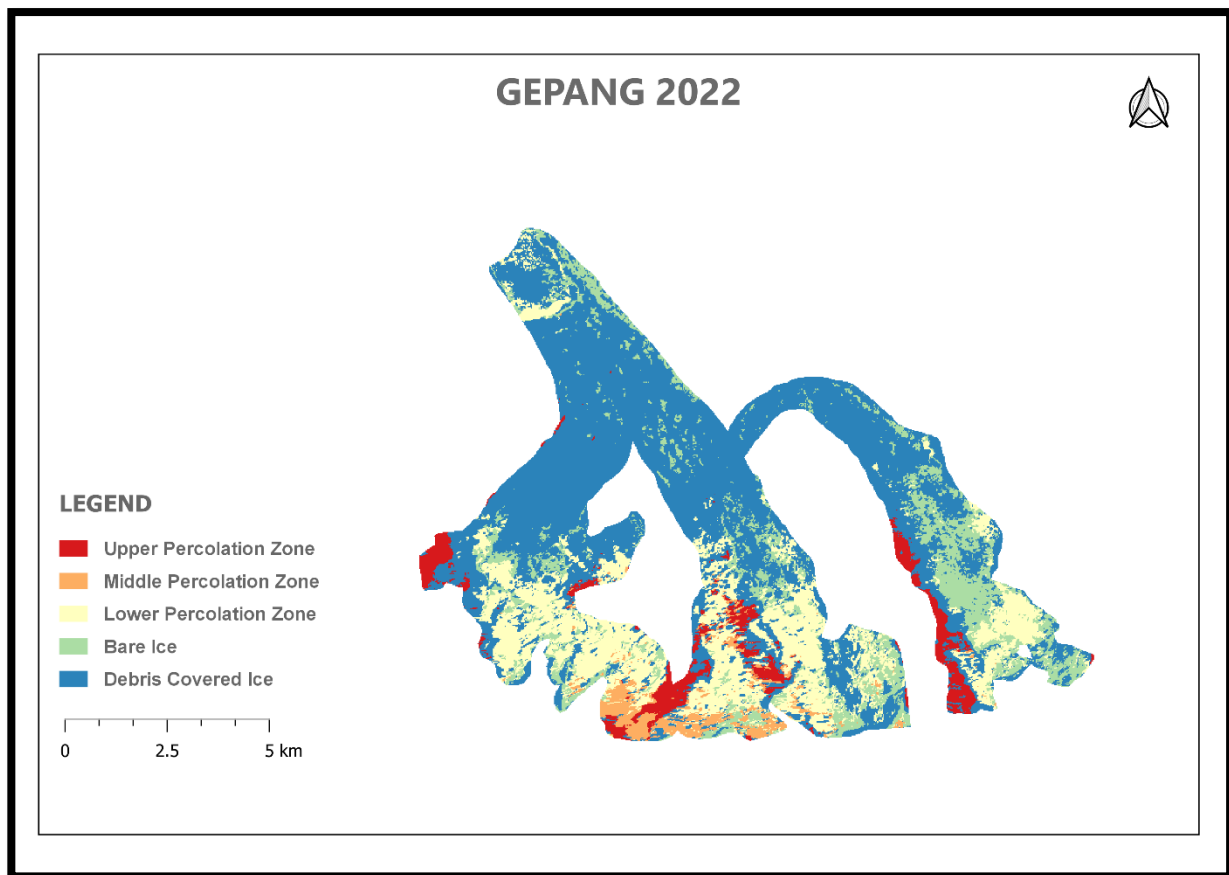


Figure 26 Gepang Gath Glacier Classified Map- 2022

The classification of Gepang (Figure 27 Gepang Gath Glacier Classified Map- 2022) backscatter value of the lake has a similar intensity value to that of the percolation zones which causes intermixing of pixels that are to be assigned to a class.

The glacier has a higher area of debris covered ice as compared to the other zones. The lower percolation zone is more prominent as compared to the middle percolation zone. The area of dry ice is considerably lower as compared to Bada shigri glacier. The middle percolation area is also much lower as compared to both Chota and Bada shigri glaciers. This could be due to rapid melting of ice due to higher temperatures in this region during summer (Sahu & Gupta, 2020). The areas for each class of GG glacier are given in the table 10.

7.1.4 Accuracy Assessment

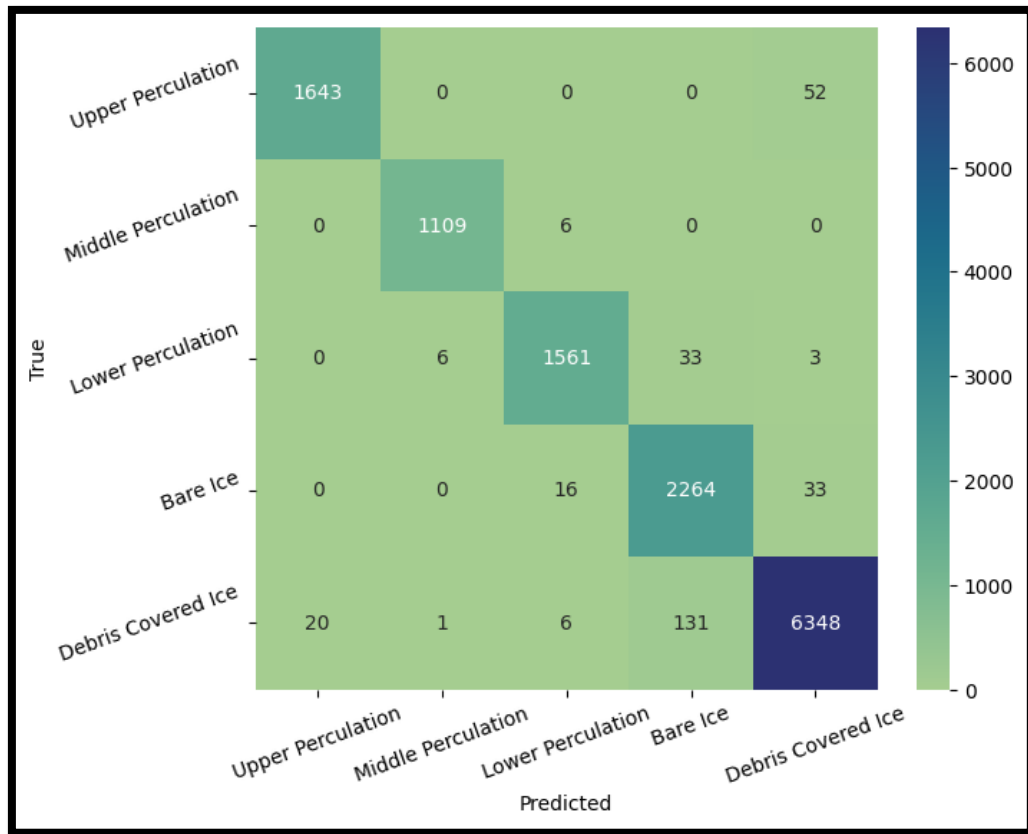


Figure 28 Error Matrix of the Classification process

Debris covered ice had the highest number of pixels across the glaciers. It also had the highest intermixing of pixels with bare ice class. The user's accuracy for upper percolation, middle percolation, lower percolation, bare ice, and debris covered ice are computed as 96%, 99%, 97%, 97% and 97% respectively. While the producer's accuracy was found to be 98%, 99%, 98%, 93% and 98% for upper percolation, middle percolation, lower percolation, bare ice and debris covered ice respectively.

7.2 Velocity Estimation of the Glaciers

Three methods of Optical, SAR feature tracking and time series InSAR were used for computation of velocity across Chota Shigri, Bada Shigri and Gepang Gath glaciers between the years 2017 and 2022.

7.2.1 Optical Feature Tracking

Sentinel-2 optical data is used for this process. The dates of acquisition used are given in the chapter 4.1 PlanetScope data (*Planet*, n.d.) was initially used for this process. Although the data had a very high resolution of 3m, the loss of spectral signature and other information over the Himalayan region resulted in a very noisy and inaccurate velocity result.

The processing was carried out in the COSI-CORR plugin for ENVI. An accurate Co-registration is a crucial step for this process so that the algorithm can detect minute displacement of features which in turn would give the velocity result. The study area is masked out from the larger image to make the data easier to handle and for reducing the processing duration.

Two images namely one pre-event image and one post-event image are chosen. The maximum cross-correlation is computed, and the displacement is estimated. COSI-CORR provides a statistical and a frequential correlator in which the latter is used for this process. It is a Fourier based correlator where the displacement is calculated with the help of the relative phase difference between the pre-event and post-event images (Sébastien Leprince et al., 2007). An initial window size of 128, a final window size of 32 with a step size of 2 with a four-pixel robustness was used for the process. The parameters were chosen carefully after referring to recommendations given in previous studies (S. Leprince et al., 2013)(Sood, 2016). The signal noise ratio band is used for reduction of noise where a SNR threshold of 0.9 was set. The velocity vector is then calculated and overlaid on the velocity map. The resultant maps of BS, CS and GG are represented below.

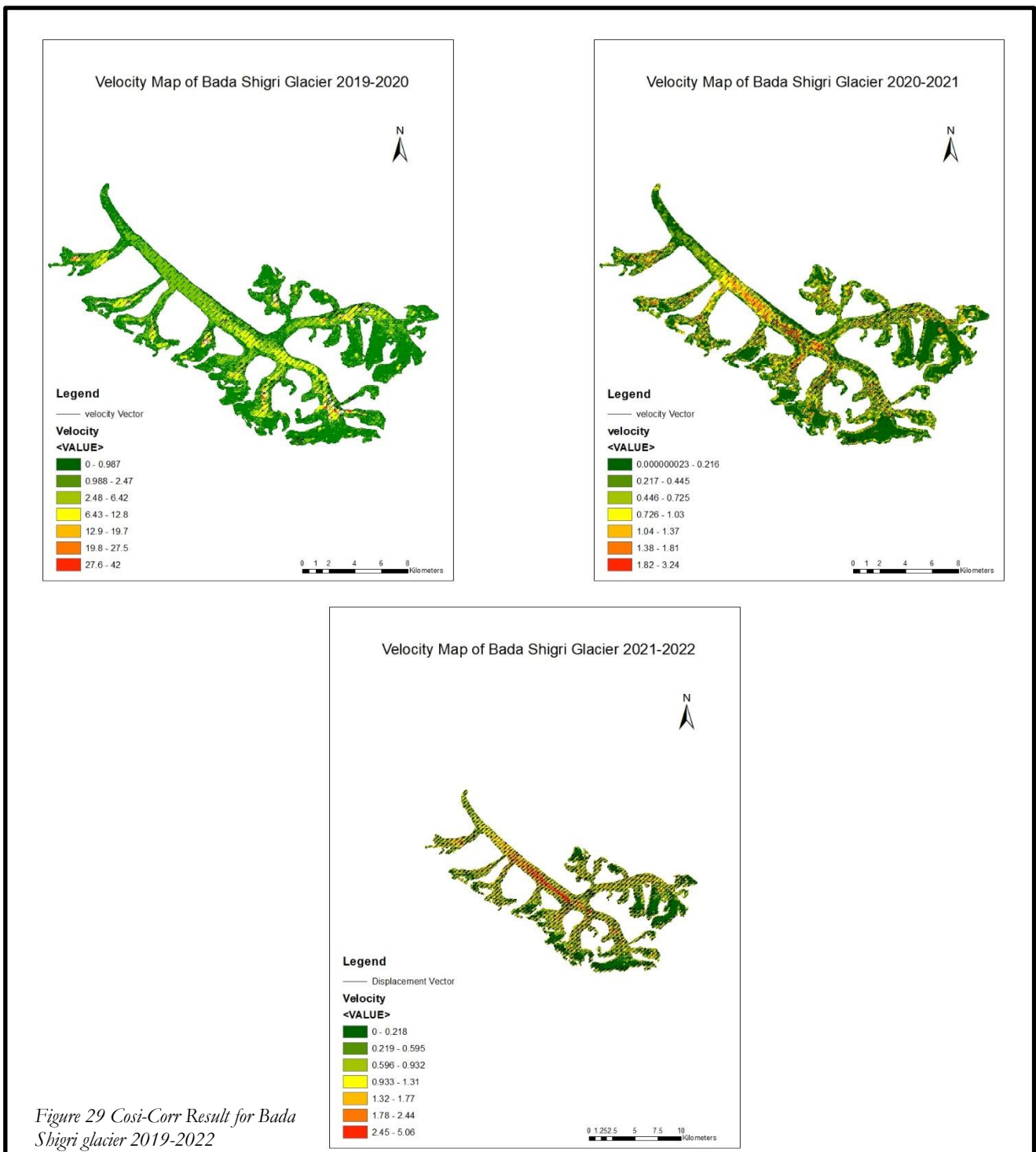


Figure 29 Cosi-Corr Result for Bada Shigri glacier 2019-2022

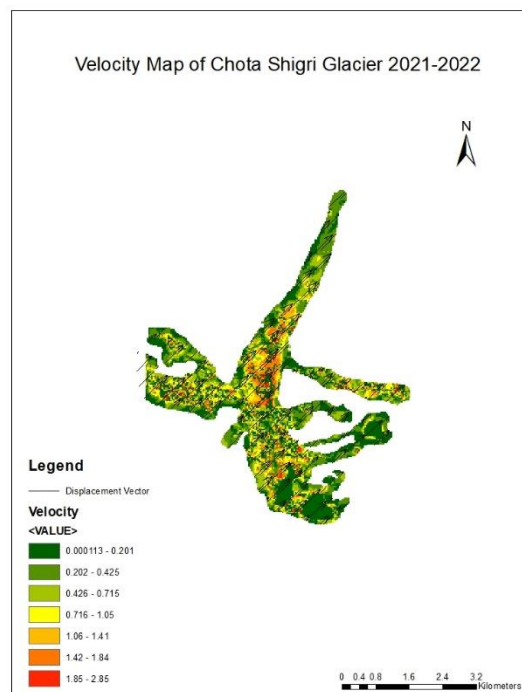
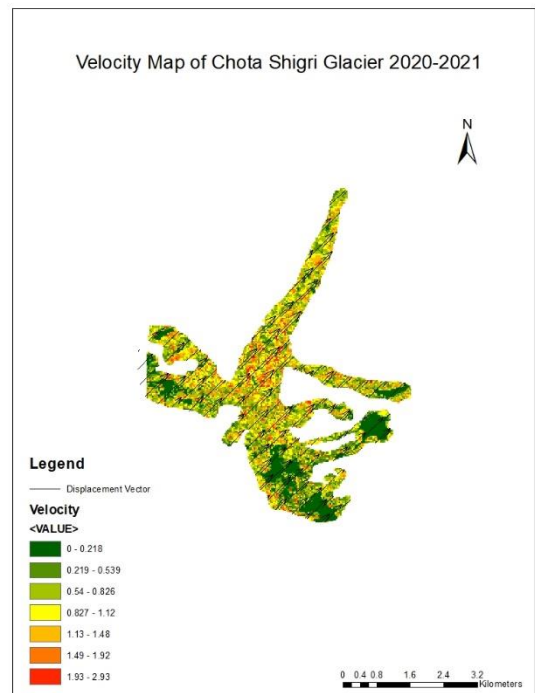
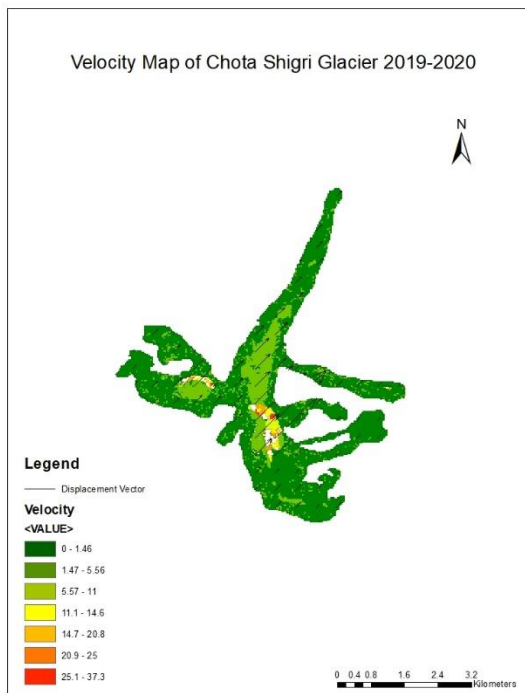


Figure 30 Cosi-Corr Result for Chota Shigri glacier 2019-2022

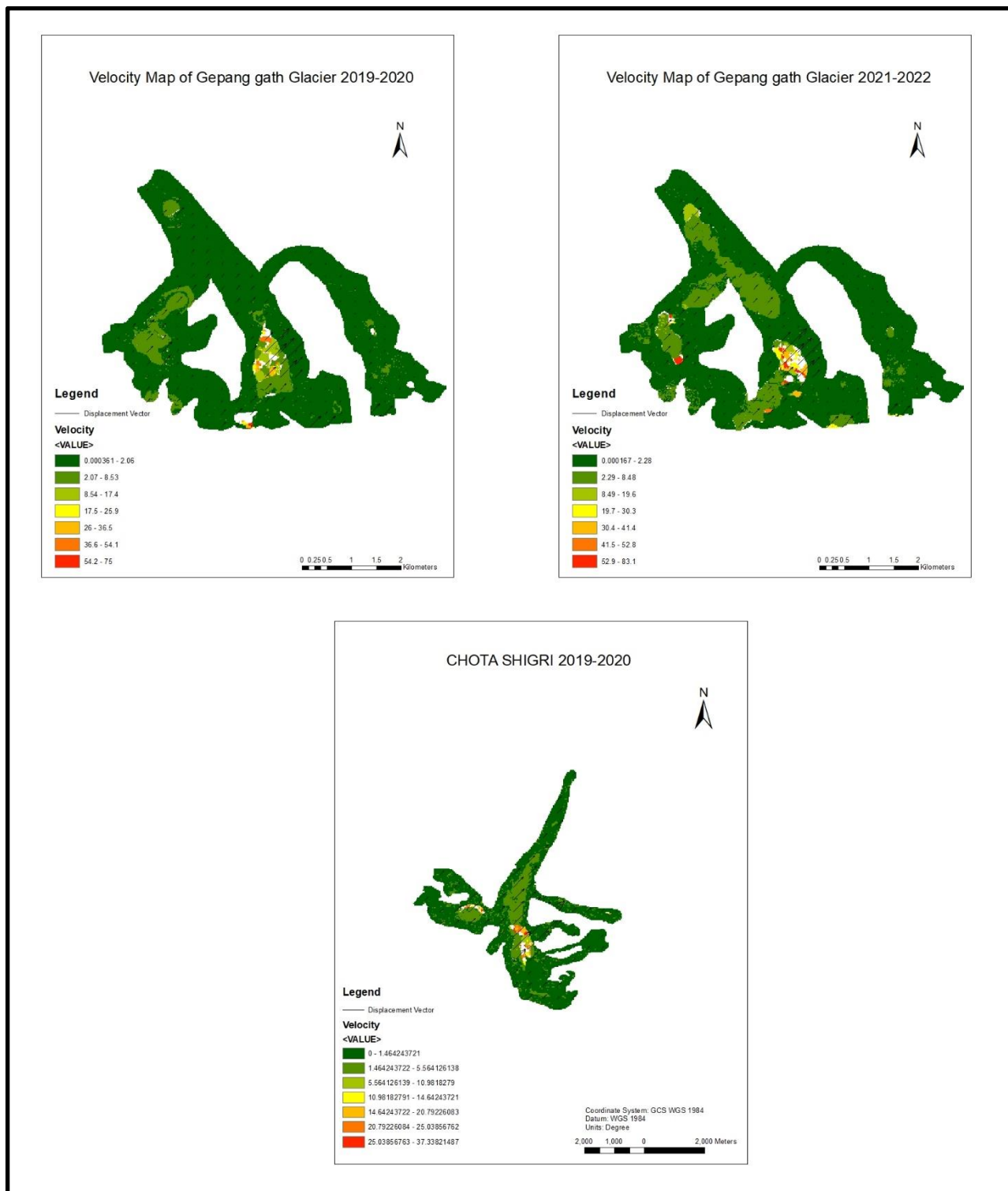


Figure 31 Cosi-Corr Result for Gepang Gath glacier 2019-2022

The deductions for the velocity obtained with COSI-CORR tool is given in chapter 8. The obtained velocity values are inconsistent through all the glaciers and don't coincide with the referred historical data nor the global velocity values. Although the input parameters were kept the same, there is a huge difference for the average velocity between the years of 2019-2020 and 2021-2022 across all the glaciers.

7.2.2 Time Series InSAR

The time series analysis was carried out using Miami time INSAR small baseline method for velocity estimation.

166 image pairs were used with which corresponds to 165 interferograms. The interferograms were imported from Alaska state facility's (ASF) data repository (NASA JPL, n.d.) to initiate the MintPY InSAR process. The interferograms were processed by ASF with Sentinel-1 products using Jet propulsion Laboratory's ARIA science data system with the ISCE (InSAR Scientific computing environment) software package (NASA JPL, n.d.).

The coherence between two SAR imageries represents the resemblance of radar reflection between them (Closson & Milisavljevic, 2017). It quantifies the amount of noise present in the interferogram (Chatterjee et al., 2014). The various statistical measure of coherence is presented below,

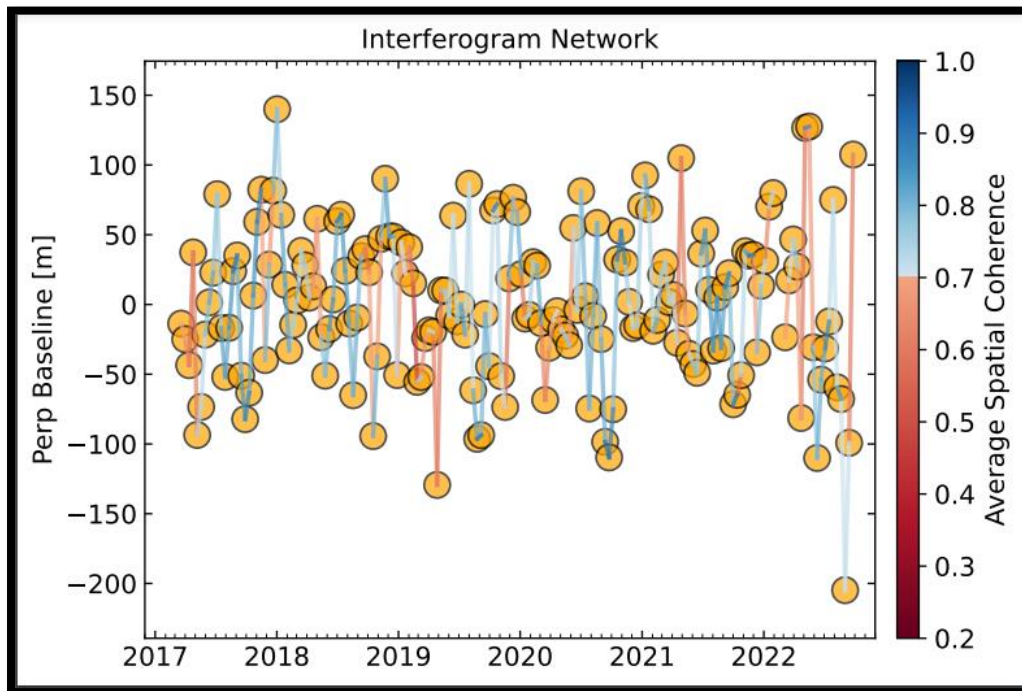


Figure 32 Average Coherence of the interferogram pairs

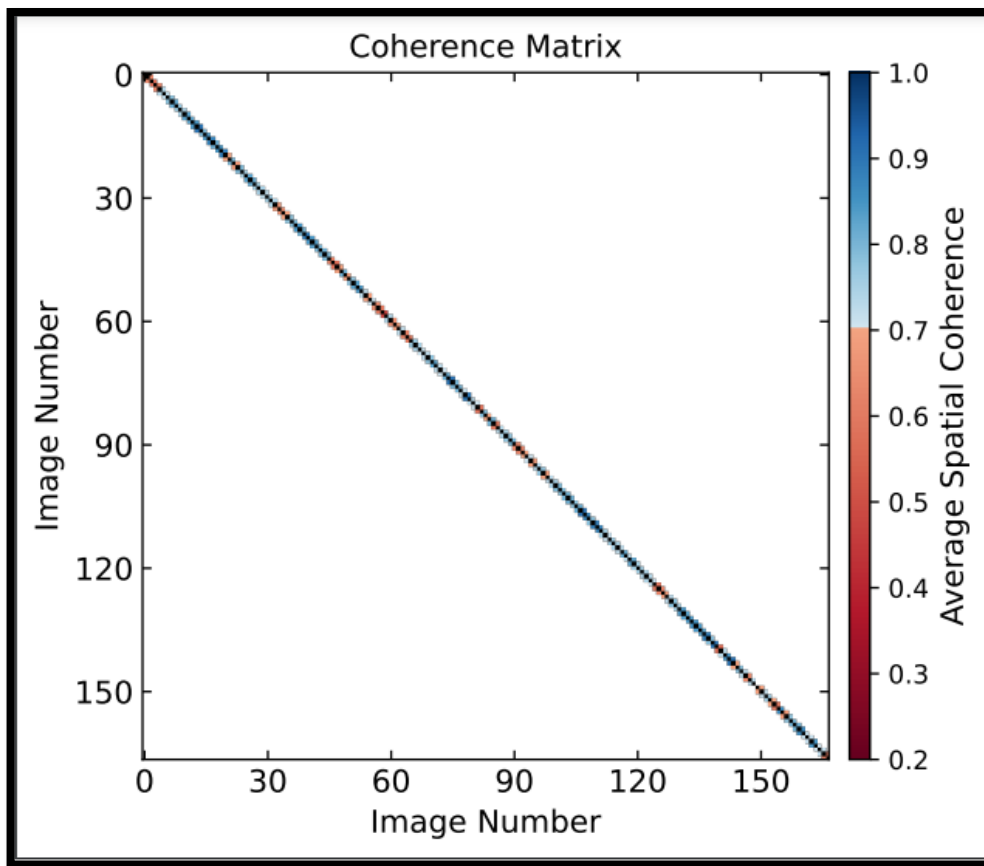


Figure 33 Average spatial coherence of each image

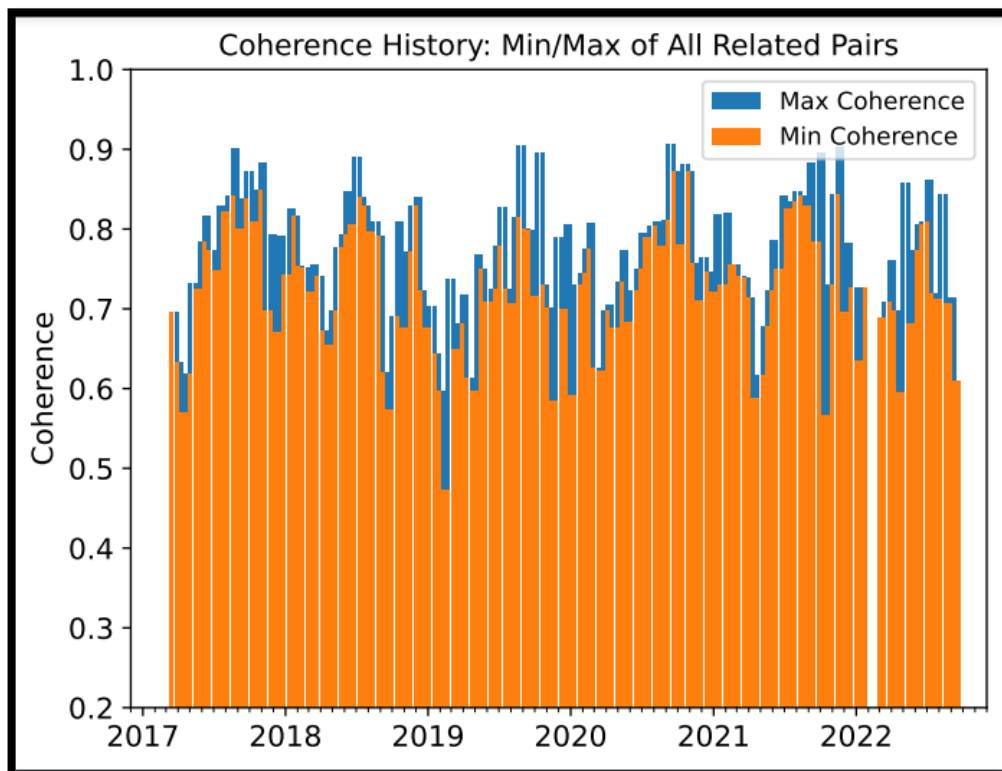


Figure 34 Minimum and Maximum coherence of each interferogram pair

The two images of a pair are sensed at a different time (temporal baseline) at a slightly different orbital angle and position (Perpendicular baseline) (ASF NASA, n.d.). The perpendicular baseline of each pair is depicted below.

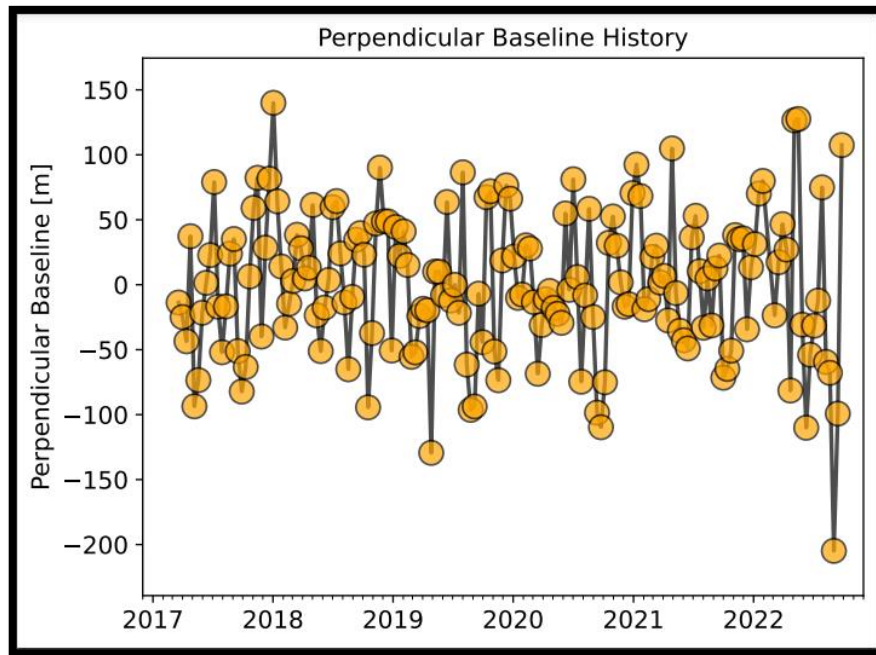


Figure 35 Perpendicular baseline of each image pair

The Velocity results for each glacier is given below. The output was received in the form of an average velocity value for the years 2017 to 2022.

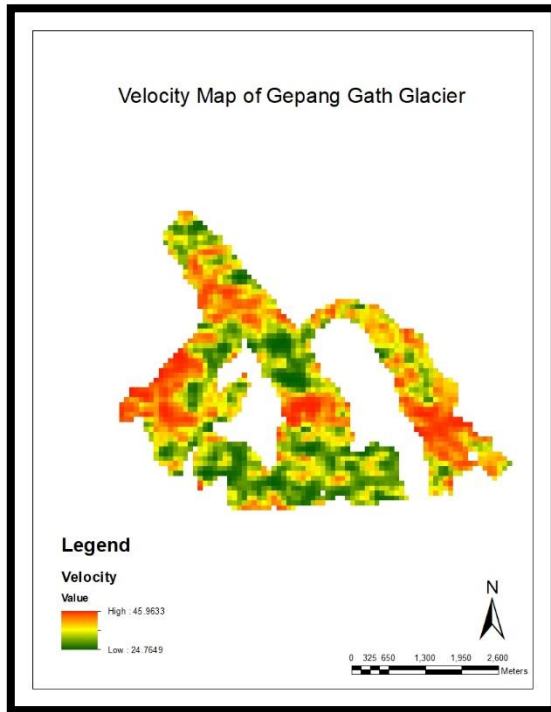
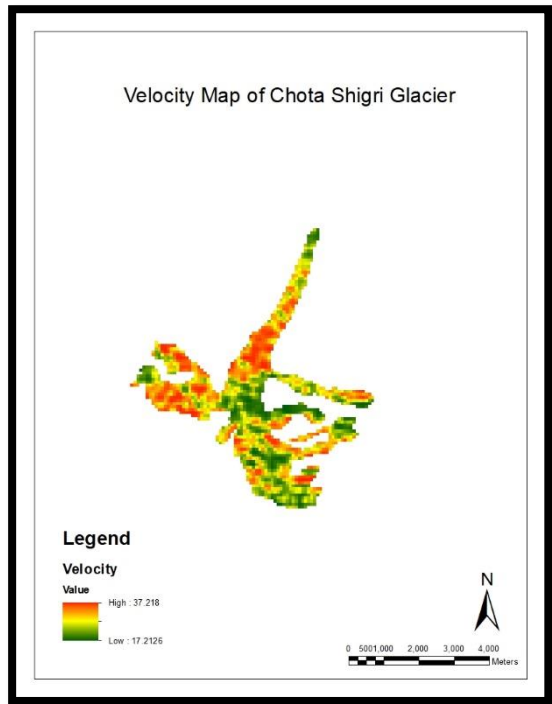
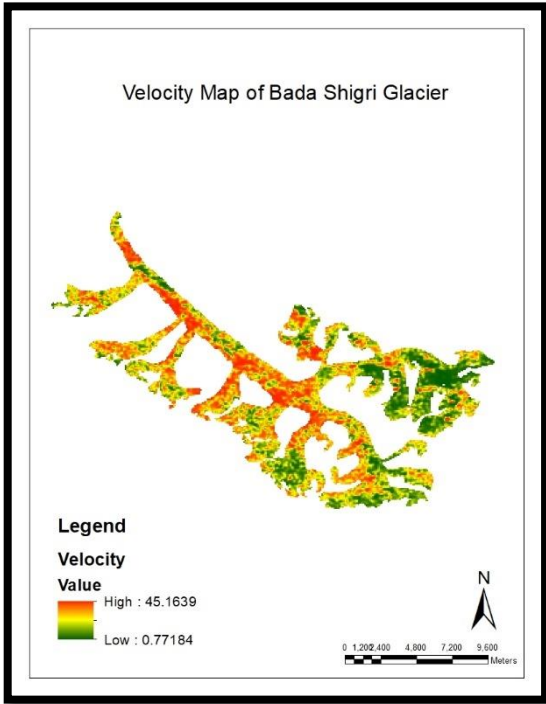


Figure 36 InSAR results of Bada Shigri, Chota Shigri and Gepang Gath Glaciers

8. DISCUSSION & CONCLUSION

8.1 Equilibrium Line Altitude (ELA) of the Glaciers [2020-2022]

The equilibrium line altitude denotes the area of a glacier where the accumulation of snow balances with the ablation of it over a period of one year (Suring, 2020). It separates both accumulation, ablation zones and is a crucial indicator of the glacier's health (A. V. Kulkarni, 1992). Accumulation generally happens at the higher elevations of the glaciers while ablation occurs at the lower elevations that are prone to higher temperatures and precipitation (van den Broeke et al., 2011).

A change in temperature can change the position of the ELA. A higher temperature pattern can result in the ELA to move upwards due to higher ablation indicating that the glacier is gradually losing its mass. A lower temperature can result in the increase of accumulation area which results in the ELA line moving downwards indicating a positive mass balance and a better health of the glacier (Vijay Mahagaonkar, 2019).

The ELA line was carefully plotted with the classified images of the study areas. It was plotted manually with QGIS and is overlaid on a High-resolution ALOS-PALSAR DEM to depict the elevations. All elevations are calculated for the ELA of the main trunk of the glacier.

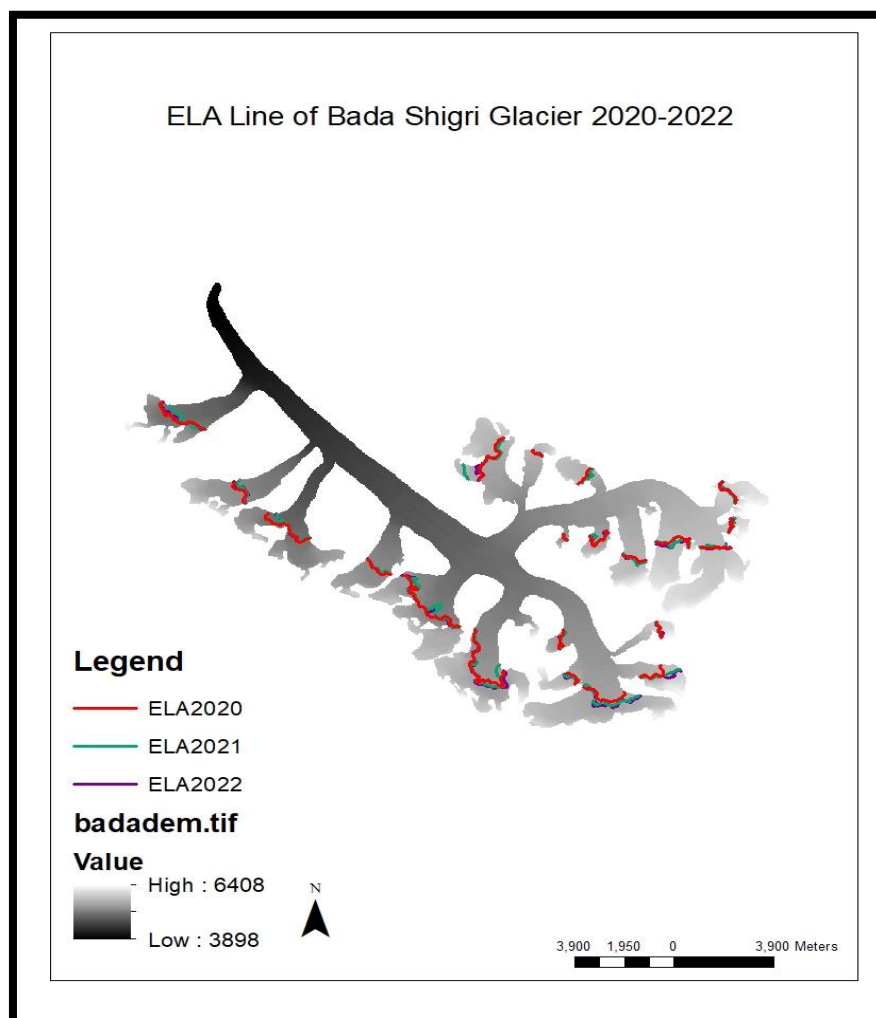


Figure 37 ELA trend of Bada Shigri Glacier

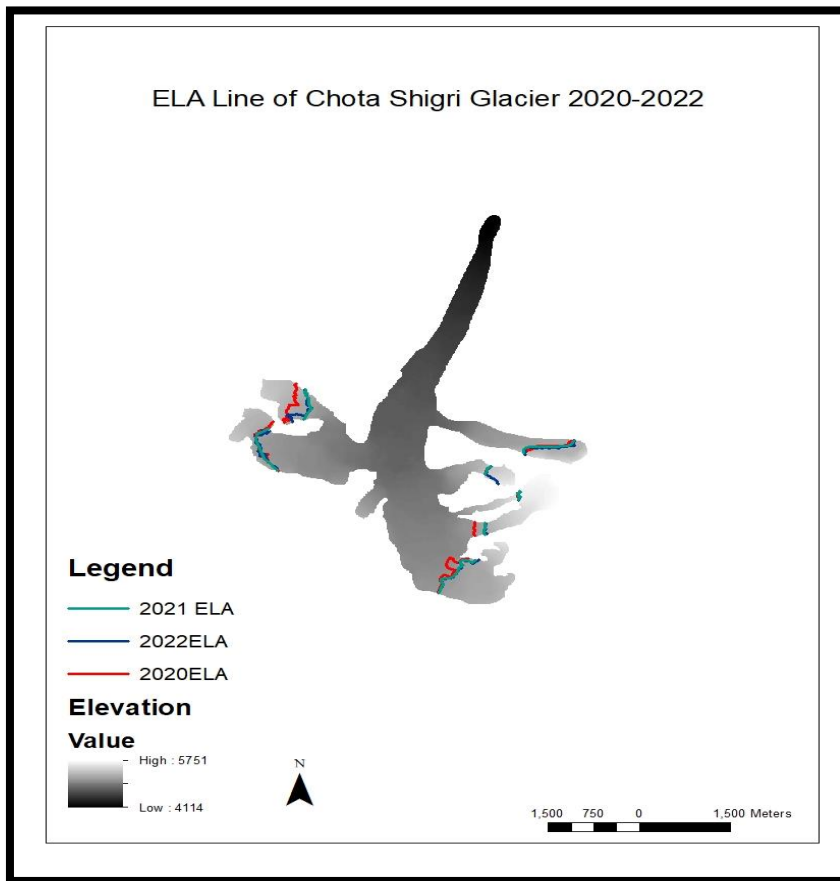


Figure 38 ELA Trend of Chota Shigri Glacier

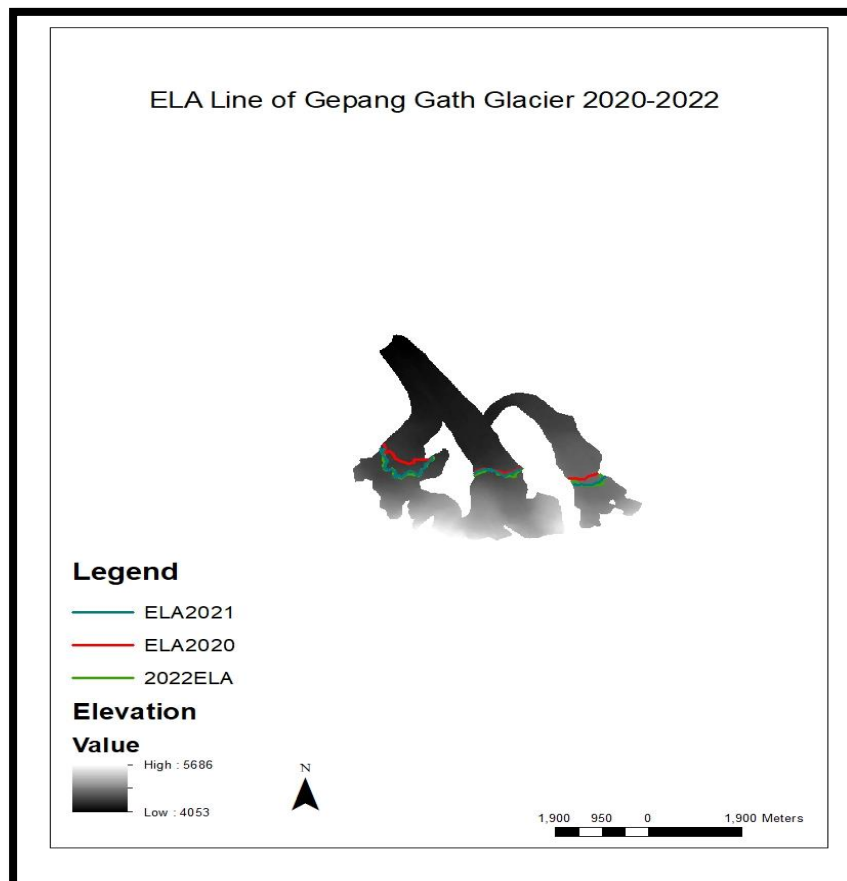


Figure 39 ELA Trend of Gepang Gath Glacier

It can be observed that there has been a change in the ELA elevation through the years of 2020 to 2022. The ELA varied from 4988m, 4995m and 5018 m for the years 2020, 2021 and 2022 respectively. The historical ELA data of Chotta Shigri shows an altitude of :- (Dobhal et al., 1995)(Chandrasekharan et al., 2018)

Year	Equilibrium Line altitude (m from m.s.l)
1987	4650
1988	4750
1989	4840
2017	4948
2020(Present Study)	4988
2021(Present Study)	4995
2022(Present Study)	5018

Table 5 Historical ELA data of Chota Shigri Glacier

The variation of Badashigri glacier's elevation line has been inconsistent through the years. The ELA varied from 5243, 5276 and 5366 m.s.l for the years 2020, 2021 and 2022 respectively. Historically, the ELA of Bada Shigri glacier has shown the following elevation changes (Sanchayita Das & Chakraborty, 2019).

Year	Equilibrium Line altitude (m from m.s.l)
2015	5357
2017	5174
2020(Present Study)	5243
2021(Present Study)	5276
2022(Present Study)	5366

Table 6 Historical ELA data of Bada Shigri Glacier

An ELA elevation of 4875, 4913, 4957 m.s.l was observed for the years 2020, 2021, 2022 for Gepang Gath glacier. The ELA of Gepang Gath glacier has varied slightly and the values are given below (Vinit Kumar et al., 2021)

Year	Equilibrium Line altitude (m from m.s.l)
1989	4771
2017	4825
2020(Present Study)	4875
2021(Present Study)	4913
2022(Present Study)	4957

Table 7 Historical ELA data of Gepang Gath glacier

This is a clear indication that the elevations of ELA of both Chota shigri and Gepang Gath glaciers have been constantly rising. This depicts an increase of the ablation area which in turn indicates that the glacier's mass is receding.

The elevation trend of Bada Shigri Glacier's ELA is inconsistent and has been either raising or lowering. This indicates an increase and decrease in ablation. This could be due to the large extent and a varying weather pattern across different sections of the glacier (Chand et al., 2017).

The change in ELA can be compared with the change in the various radar zones of the glacier. The areas of five classified zones of the glacier for the years 2020 to 2022 are given in the table below:

For Bada Shigri Glacier,

2020	Class Names	Pixel Count	Area Sqm	Area Sqkm
	5 Debris	386294	38629400	38.6294
	4 Bare Ice	382128	38212800	38.2128
	3 Lower perc	59874	5987400	5.9874
	2 middle per	185002	18500200	18.5002
	1 Upper perc	86810	8681000	8.681
2021				
	5 Debris	368920	36892000	36.892
	4 Bare Ice	358612	35861200	
	3 Lower perc	47636	4763600	4.7636
	2 middle per	239304	23930400	23.9304
	1 Upper perc	85636	8563600	8.5636
2022				
	5 Debris	433782	43378200	43.3782
	4 Bare Ice	275822	27582200	27.5822
	3 Lower	199065	19906500	19.9065
	2 middle per	107461	10746100	10.7461
	1 Upper perc	83978	8397800	8.3978

Table 8 Area of each classified zone of Bada Shigri glacier

For Chota Sigri Glacier,

2020	Class Names	Pixel	Area Sqm	Area SqKm
	5 Debris	57135	5713500	5.7135
	4 Bare Ice	49518	4951800	4.9518
	3 Lower perc	17424	1742400	1.7424
	2 middle per	6715	671500	0.6715
	1 Upper perc	7130	713000	0.713
2021				
	5 Debris	52217	5221700	5.2217
	4 Bare Ice	41413	4141300	4.1413
	3 Lower perc	16040	1604000	1.604
	2 middle per	20615	2061500	2.0615
	1 Upper perc	7637	763700	0.7637
2022				
	5 Debris	64544	6454400	6.4544
	4 Bare Ice	27869	2786900	2.7869
	3 Lower perc	35628	3562800	3.5628
	2 middle per	2407	240700	0.2407
	1 Upper perc	7474	747400	0.7474

Table 9 Area of each classified zone of Chota Shigri glacier

For Gepang Gath glacier,

2020	Class Names	Pixel	Area Sqm	Area SqKm
	5 Debris	70759	7075900	7.0759
	4 Bare Ice	31693	3169300	3.1693
	3 Lower perc	31910	3191000	3.191
	2 middle per	6715	852700	0.8527
	1 Upper perc	7130	724500	0.7245
2021				
	5 Debris	72407	7240700	7.2407
	4 Bare Ice	32431	3243100	3.2431
	3 Lower perc	21628	2162800	2.1628
	2 middle per	16615	1661500	1.6615
	1 Upper perc	7052	705200	0.7053
2022				
	5 Debris	82350	8235000	8.235
	4 Bare Ice	21956	2195600	2.1956
	3 Lower perc	32508	3250800	3.2508
	2 middle per	5211	521100	0.5211
	1 Upper perc	8109	810900	0.8109

Table 10 Area of each classified zone of Gepang Gath glacier

8.2. Glacier Velocity

The velocities were successfully calculated using feature tracking and interferometric methods for Bada Shigri, Chota Shigri and Gepnag gath glaciers.

Velocities across the glacier changes depending upon the season. It is generally higher during summer due to reduction of basal friction which aids in easier sliding and is lower during winter due to a denser snowpack condition and lesser basal friction (Satyabala, 2016) . However, for both optical and SAR feature tracking, the images used were sensed in the month of September which ensures a snow-free scenario in which the feature tracking algorithm works better. Hence, the velocities are presumed to be similar throughout the year. A more accurate velocity result can be generated by estimating velocities for all the three seasons separately and averaging the values (Mahagaonkar et al., 2019).

The Pixel tracking process performed with SAR dataset using SARPROZ software did not generate a satisfactory result. This could be due to an error with co-registration of the images or due to an algorithm that does not detect slow movement on a glacier setting. Hence, these results are not used for comparison. However, this study gives an opportunity to provide insight on the software’s performance for cryosphere studies and crucial feedback can be provided as the pixel tracking feature is still in its beta stage.

Due to COVID complications and time constraints, a visit to the field study area was not feasible. Although the validation of results could not be done with data collected from field, it can be compared with existing research studies/literature to gain an insight in the closeness/consistency of the estimates obtained.

The historical velocity values of Bada Shigri glacier are given in the graph below (Yellala et al., 2019a).

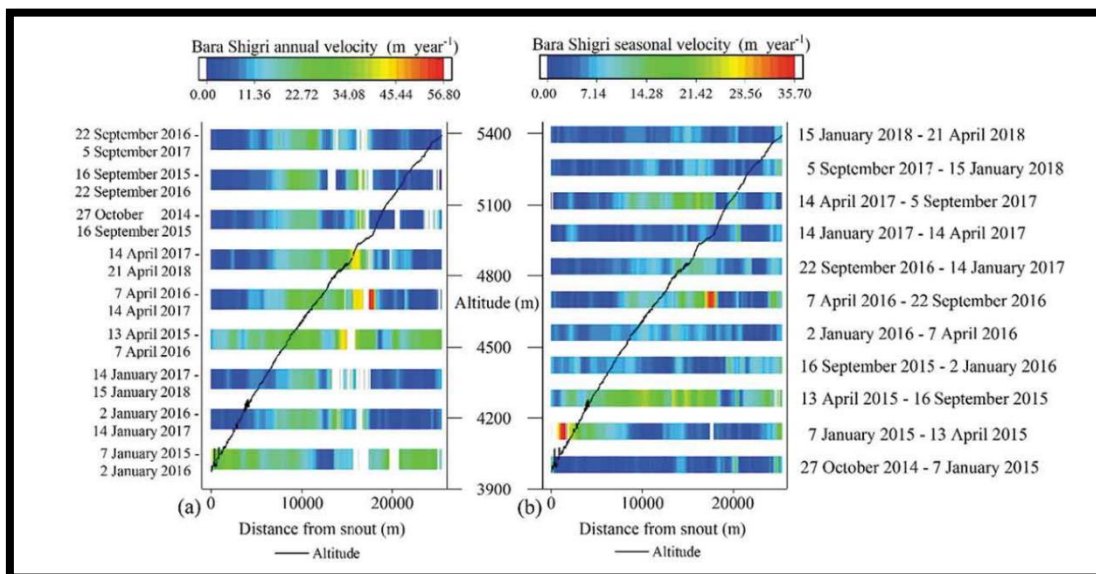


Figure 40 Past Velocity data of Bada Shigri glacier (Yellala et al., 2019a)

It can be deciphered that the velocity of the glacier generally varies between 3-7 m/year with a maximum velocity not exceeding 35 m/year. (Sahu & Gupta, 2019) observed a reduction of 34% in the velocity values in the recent years when compared to values two decades ago.

Year	Velocity (m/year)
1999-2000	34.92
2000-2001	30.82
2001-2002	31.19
2013-2014	20.79
2014-2015	21.73
2019-2022	12(Current Study InSAR)
2019-2022(Averaged)	18.5(Cosi-Corr)

Table 11 Historical velocity data of Bada Shigri glacier

The Velocity at a point at the main trunk of the glacier in the current study showed an average velocity value of 12 m/year with a maximum velocity of 45 m/year for the years 2017-2022. This coincides with the varying trends of velocity of previous studies. The Cosi-Corr process with optical imagery showed a maximum velocity of 47 m/year for 2019-2020, 3.5m/year for 2020-2021 and 5m/year for 2021-2022.

The Historical computed velocity values for Chotta Shigri glacier are given below,

Year	Velocity (m/year)
2003-2004	24 (Field Based) (Reet Kamal Tiwari, 2014)
2006-2007	37 (Field Based) (Reet Kamal Tiwari, 2014)
2013-2014	22.73 (Sahu & Gupta, 2019)
2016-2017	19.53 (Sahu & Gupta, 2019)
2019-2022	18 (Current Study InSAR)
2019-2022(Averaged)	32.7(Cosi-Corr)

Table 12 Historical velocity data for Chota Shigri glacier

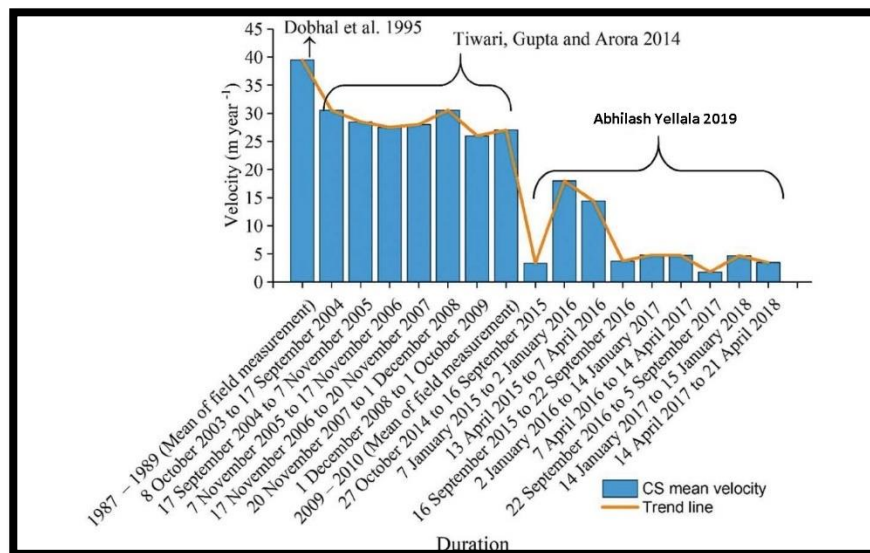


Figure 41 Past Velocity trend of Chota Shigri Glacier (Yellala et al., 2019b)

Further studies (Dobhal et al., 1995)(Reet Kamal Tiwari, 2014)(Yellala et al., 2019b) showed the following velocity trends as depicted in figure 44.. It can be deciphered that Chota Shigri glacier has had a declining trend (Dobhal et al., 1995))of velocity when compared to values from two decades ago. Slight increase in velocity values can be seen for the years of 2016 and 2017.

The time series InSAR result generated with this study showed an average velocity at a pixel in the main trunk as 18 m/year. This value is slightly higher than the recorded trends. The maximum velocity possible was observed to be 37 m/year. The optical feature tracking process showed a maximum velocity of 27, 2.8, 2.9 m/year for the years 2019-2020, 2020-2021 and 2021-2022 respectively.

Gepang gath glacier showed an inconsistent trend and has a velocity value higher than that of both Bada and Chota shigri glaciers.

Year	Velocity m/year
2000-2001	33.43
2002-2003	41
2013-2014	37
2019-2022	23 (Current Study InSAR)
2019-2022 (Averaged)	25 (Cosi-Corr)

Table 13 Historical Velocity data of gepang gath glacier

The Time series InSAR results of the current study shows a minimum velocity of 23 m/year and a maximum possible velocity of 45 m/year which still puts Gepang Gath in the category of a slow-moving glacier. The Cosi-Corr process showed a velocity of 20,25 and 30 m/year at the trunk of the glacier for the years 2019-2020,2020-2021,2021-2022 respectively.

The higher velocity values maybe due to the presence of a glacial lake which enhances the basal lubricant and changes the surface gradient considerably (D. I. Benn et al., 2012)(Bhushan et al., 2018). It could also be because of a higher slope gradient that enables a faster flow of the glacier components (Bhushan et al., 2018).

The inconsistency in the velocity values for optical cross correlation could be related to issues in data. Multiple optical images of PlanetScope and Landsat8 were used, but the tool returned inconsistent values of velocity. This could also be due to the inconsistent weather patterns and snow cover in the region.

8.2.1 GoLIVE Velocity trend

GoLIVE (Global Land Ice Velocity Extraction)(NSIDC, 2013.) is a global dataset that comprises of ice velocity of all terrestrial glaciers from March 2013 to present. The velocity is computed with Landsat 8 panchromatic imagery using an image cross-correlation algorithm. It has a temporal resolution of 16 days and a spatial resolution of 300x300 m

Various studies (Sam et al., 2018) (Khadka et al., 2021)have utilized GoLive data for analysis and validation. The data used is prone to be affected by cloud cover and the feature tracking algorithm for velocity estimation may not be suitable for both slow and fast moving glaciers alike (Sivalingam et al., 2021).The velocity obtained from GoLive is depicted in the graph below. The velocity was obtained in the form of a CSV file for a point in the main trunk of the glaciers for the September months of each year.

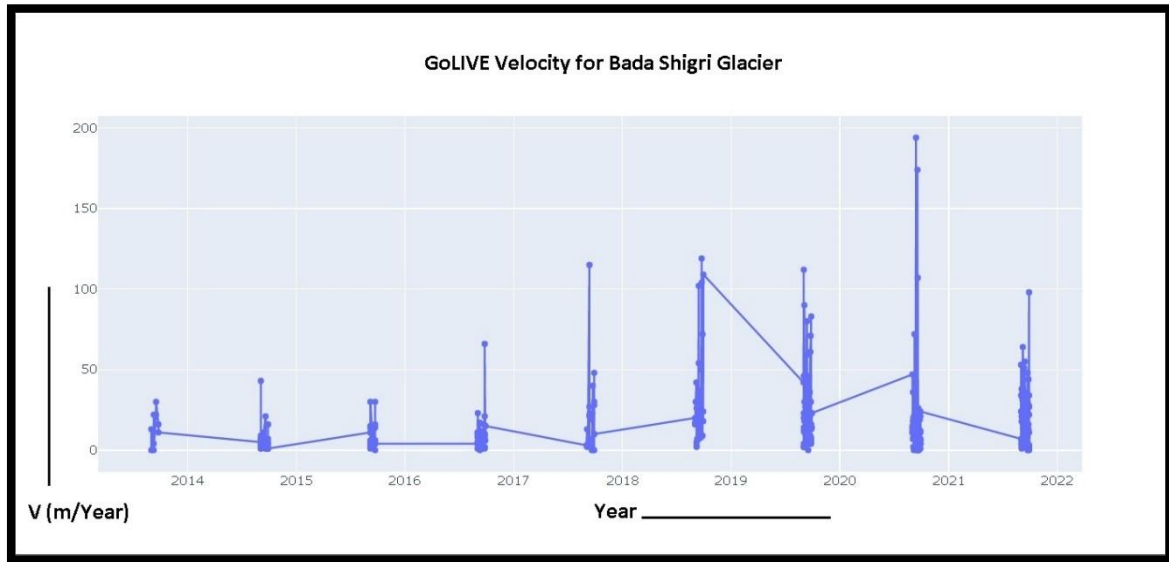


Figure 42 GoLive Velocity trend graph 2014-2021

It can be observed that there is a huge variation in the values with outliers up to about 200 m/year for the year of 2020 which highly deviates from the results obtained from this study and the previously mentioned studies. The velocity also shows an upward trend from 2013-2021 which is directly opposite to the claims of previous studies mentioned in the tables in section 9.2.

Similar trends can be observed for Chota Shigi and Gepang Gath glaciers as well. Although these values can be averaged after eliminating outliers to obtain a fairly accurate result, relevant literature review of past velocity studies and field trips should be conducted to ensure accurate research.

8.3 Research Questions

The completion of this research enables us to answer the following research questions: -

1) *What methods are applicable for glacier facies classification?*

Various workflows can be adopted for carrying out the classification process. Polarimetric decomposition method is an accurate method adopted by various studies for classification but was not deemed suitable for this study. Decomposition process could not be applied to the study due to non-availability of free quad polarized data over the Indian Himalayan region, various methods were investigated during the literature review phase of the thesis.

This study utilized RGB composites for exploiting the unique characteristics possessed by each zone of the glacier. The zones could easily be identified for an accurate delineation of zones.

2) *Which machine learning classification algorithm is optimal for an accurate facies' classification?*

Various ML algorithms have been used over the years for glacial studies. The commonly used ones are support vector machines (SVM), Random Forest (RF), and artificial neural network (ANN). Various studies were investigated that compared these algorithms with one another. Random forest responds the

best for an accurate facies' classification with an accuracy of 95.06%, while other algorithms like SVM and ANN showed 92.86% and 91.86% accuracy respectively (Speiser et al., 2019).

Although different ML algorithms were not compared in the study for their accuracies, previous studies dictate that the RF model gives accurate results. The RF model used in this study returned an out of bag accuracy of 97%, which shows that the performance of the model is good. Hyperparameter tuning was performed to assess the most accurate parameters to be set as mentioned in section 7.1. Accuracy assessment showed the user's and producer's accuracy to be above 95% across all the classes.

Although field visits were not feasible for validation of this result, the classified zones could be compared with ELA of previous studies over the study area for comparison. The obtained results coincide with the historical ELA trend for all the three glaciers.

3) How can the accumulation and ablation zones be mapped?

Accumulation zone represents the region of the glacier where the snow of a season survives the whole preceding season without melting. This increases the mass of the glacier. The ablation zone is the region where snow melts and the glacier mass are lost. These two regions are separated by the equilibrium altitude line (ELA).

Classification of the glacier gave an insight on the various zones (Bare ice, Debris covered ice, Lower, middle, and upper percolation zones) of the glacier. The region where the percolation zone meets the bare ice or debris covered ice is where the ablation initiates. The accumulation region, ablation region and ELA could be identified this way.

4) How has the ELA evolved over the years and what could be the driving factors behind this?

ELA was mapped for all the three glaciers after classification of their facies'. The historical data of the trend of ELA change is given in section 9.1.

Looking at the larger picture, all three glaciers have been gradually receding which is made evident by the change in position of the ELA to a higher elevation. This indicates the increase in area of ablation. Although a research on the driving factors were not carried out, previous studies (Ding et al., 2006)(S. S. Sharma & Ganju, 2000)(Azam et al., 2016) on the Indian Himalayan region indicate the ELA change occurs mostly due to change in meteorological conditions like climate and rainfall.

The ELA of Bada shigri glacier changed from 5243m to 5366m from 2020 to 2022. ELA of Chota Shigri glacier changed from 4988m to 5018m for the same period. Gepang gath showed an ELA change of 4875m to 4957m.

5) How has the velocity trend changed over the years?

The velocities of BS, CS AND GG were calculated using feature tracking of SAR, optical datasets, and time series InSAR methods. The results are validated using existing published research. This study and the historical data shows that the velocity has a constant reduction in velocity in all the glaciers. This could be due the decadal change in accumulation and/or ablation of the glaciers(Y. Zhou et al., 2021)

8.4 Future Scope of work

The Himalayan glaciers are more prone to cause disasters due to proximity of settlements in downstream of the glaciers/ rivers that the glaciers feed into. Glacial hazards/disasters have been on the rise in the states of Himachal Pradesh and Uttarakhand. Hence, Constant monitoring of glacier facies and modelling studies for all major glaciers in the IHR should be carried out as such work is minimal in this region as compared to glaciers of the north and south poles. Polarimetric classification with the help of decompositions should be carried with quad-polarized data. Using an L band data could give more detailed interpretation of sub glacial features and ice crevasses.

9. REFERENCES

- Adam, S., Pietroniro, A., & Brugman, M. M. (1997). Glacier snow line mapping using ERS-1 SAR imagery. *Remote Sensing of Environment*, 61(1), 46–54. [https://doi.org/10.1016/S0034-4257\(96\)00239-8](https://doi.org/10.1016/S0034-4257(96)00239-8)
- Aher, S. P., Khemnar, S. B., & Shinde, S. D. (2014). Synthetic Aperture Radar in Indian Remote Sensing. *International Journal of Applied Information Systems (IJAIS)*, 7(2). www.ijais.org
- Alvarinho J. Luis, S. S. (2020). High-resolution multispectral mapping facies on glacier surface in the Arctic using WorldView-3 data. *MUNI Journals*, 10(1). <https://doi.org/https://doi.org/10.5817/CPR2020-1-3>
- Apollo, M., Andreychouk, V., Rawat, K., Mostowska, J., Jones, T. E., Rettinger, R., & Maciuk, K. (2022). International Journal of conservation science. Himalayan nature based tourism. Challenges for tourism and protected areas. *International Journal of Conservation Science*, 12(1), 249–266. www.ijcs.ro
- Armstrong, R. L. (Richard L., & Brun, E. (2010). *Snow and climate : physical processes, surface energy exchange and modeling*. Cambridge University Press. <https://www.cambridge.org/in/academic/subjects/earth-and-environmental-science/climatology-and-climate-change/snow-and-climate-physical-processes-surface-energy-exchange-and-modeling?format=PB&isbn=9780521130653>
- ASF NASA. (n.d.). *Baseline - ASF SAR Data Search Manual*. Retrieved January 2, 2023, from <https://docs.asf.alaska.edu/vertex/baseline/>
- Azam, M. F., Ramanathan, A. L., Wagnon, P., Vincent, C., Linda, A., Berthier, E., Sharma, P., Mandal, A., Angchuk, T., Singh, V. B., & Pottakkal, J. G. (2016). Meteorological conditions, seasonal and annual mass balances of Chhota Shigri Glacier, western Himalaya, India. *Annals of Glaciology*, 57(71), 328–338. <https://doi.org/10.3189/2016AOG71A570>
- Baek, W.-K., Jung, H.-S., Chae, S.-H., & Lee, W.-J. (2018). Two-dimensional Velocity Measurements of Uvêrsbreen Glacier in Svalbard Using TerraSAR-X Offset Tracking Approach. *Korean Journal of Remote Sensing*, 34(3), 495–506. <https://doi.org/10.7780/KJRS.2018.34.3.5>
- Baghdadi, N., Bernier, M., & Gauthier, Y. (1997). Capability of Multitemporal ERS-1 SAR Data for Wet-Snow Mapping . *Remote Sensing of Environment*, 60(2), 174–186. [https://doi.org/10.1016/S0034-4257\(96\)00180-0](https://doi.org/10.1016/S0034-4257(96)00180-0)
- Baird, T., Bristow, C. S., & Vermeesch, P. (2019). Measuring Sand Dune Migration Rates with COSI-Corr and Landsat: Opportunities and Challenges. *Remote Sensing 2019, Vol. 11, Page 2423*, 11(20), 2423. <https://doi.org/10.3390/RS11202423>
- Bamber, J. L., & Rivera, A. (2007). A review of remote sensing methods for glacier mass balance determination. *Global and Planetary Change*, 59(1–4), 138–148. <https://doi.org/10.1016/J.GLOPLACHA.2006.11.031>
- Barry, R. G. (2006). The status of research on glaciers and global glacier recession: a review. *Progress in Physical Geography*, 30(3), 285–306. <https://doi.org/10.1191/0309133306PP478RA>
- Benn, D. I., Bolch, T., Hands, K., Gulle, J., Luckman, A., Nicholson, L. I., Quincey, D., Thompson, S., Toumi, R., & Wiseman, S. (2012). Response of debris-covered glaciers in the Mount Everest region to recent warming, and implications for outburst flood hazards. *Earth-Science Reviews*, 114(1–2), 156–174. <https://doi.org/10.1016/J.EARSCIREV.2012.03.008>
- Benn, Douglas I., & Evans, D. J. A. (1996). The interpretation and classification of subglacially-deformed materials. *Quaternary Science Reviews*, 15(1), 23–52. [https://doi.org/10.1016/0277-3791\(95\)00082-8](https://doi.org/10.1016/0277-3791(95)00082-8)
- Berthier, E., Arnaud, Y., Kumar, R., Ahmad, S., Wagnon, P., & Chevallier, P. (2007). Remote sensing estimates of glacier mass balances in the Himachal Pradesh (Western Himalaya, India). *Remote Sensing of Environment*, 108(3), 327–338. <https://doi.org/10.1016/J.RSE.2006.11.017>
- Bhambri, R., Hewitt, K., Kawishwar, P., & Pratap, B. (2017). Surge-type and surge-modified glaciers in the Karakoram. *Scientific Reports 2017 7:1*, 7(1), 1–14. <https://doi.org/10.1038/s41598-017-15473-8>
- Bhattacharya, A., Arora, M. K., & Sharma, M. L. (2011). Usefulness of synthetic aperture radar (SAR) interferometry for digital elevation model (DEM) generation and estimation of land surface displacement in Jharia coal field area. *Http://Dx.Doi.Org/10.1080/10106049.2011.614358*, 27(1), 57–77. <https://doi.org/10.1080/10106049.2011.614358>
- Bhushan, S., Syed, T. H., Arendt, A. A., Kulkarni, A. V., & Sinha, D. (2018). Assessing controls on mass budget and surface velocity variations of glaciers in Western Himalaya. *Scientific Reports*, 8(1).

- <https://doi.org/10.1038/S41598-018-27014-Y>
- Bishop, B. C. and C. (2022, November). *Himalayas*. Britannica.
<https://www.britannica.com/place/Himalayas>
- Blunier, T., & Schwander, J. (2000). Gas enclosure in ice : age difference and fractionation. *Physics of Ice Core Records*, 307–326.
- Bolch, T., Kulkarni, A., Kääb, A., Huggel, C., Paul, F., Cogley, J. G., Frey, H., Kargel, J. S., Fujita, K., Scheel, M., Bajracharya, S., & Stoffel, M. (2012). The state and fate of himalayan glaciers. *Science*, 336(6079), 310–314.
https://doi.org/10.1126/SCIENCE.1215828/SUPPL_FILE/BOLCH.SM.PDF
- Bookhagen, B., & Burbank, D. W. (2010). Toward a complete Himalayan hydrological budget: Spatiotemporal distribution of snowmelt and rainfall and their impact on river discharge. *Journal of Geophysical Research: Earth Surface*, 115(F3), 3019. <https://doi.org/10.1029/2009JF001426>
- Breiman, L. (2001). Random forests. *Machine Learning*, 45(1), 5–32.
<https://doi.org/10.1023/A:1010933404324/METRICS>
- Chand, P., Sharma, M. C., Bhambri, R., Sangewar, C. V., & Juyal, N. (2017). Reconstructing the pattern of the Bara Shigri Glacier fluctuation since the end of the Little Ice Age, Chandra valley, north-western Himalaya. *Progress in Physical Geography*, 41(5), 643–675. <https://doi.org/10.1177/0309133317728017>
- Chandrasekharan, A., Ramsankaran, R. A. A. J., Pandit, A., & Rabatel, A. (2018). Quantification of annual glacier surface mass balance for the Chhota Shigri Glacier, Western Himalayas, India using an Equilibrium-Line Altitude (ELA) based approach. *International Journal of Remote Sensing*, 39(23), 9092–9112.
https://doi.org/10.1080/01431161.2018.1506182/SUPPL_FILE/TRES_A_1506182_SM8557.DOCX
- Chatterjee, R. S., Lakhera, R. C., & Dadhwal, V. K. (2014). *Canadian Journal of Remote Sensing Journal Canadien de Teledetection InSAR coherence and phase information for mapping environmental indicators of opencast coal mining: a case study in Jbaria Coalfield, Jharkhand, India InSAR coherence and phase information for mapping environmental indicators of opencast coal mining: a case study in Jbaria Coalfield, Jharkhand, India.*
<https://doi.org/10.5589/m10-047>
- Chen, C. W., & Zebker, H. A. (2002). Phase Unwrapping for Large SAR Interferograms: Statistical Segmentation and Generalized Network Models. *IEEE TRANSACTIONS ON GEOSCIENCE AND REMOTE SENSING*, 40(8). <https://doi.org/10.1109/TGRS.2002.802453>
- Closson, D., & Milisavljevic, N. (2017). InSAR Coherence and Intensity Changes Detection. *Mine Action - The Research Experience of the Royal Military Academy of Belgium*. <https://doi.org/10.5772/65779>
- Das, Sanchayita, & Chakraborty, M. (2019). Mass balance of Chhota Shigri glacier using dual-polarized C band SAR data. *Remote Sensing Applications: Society and Environment*, 13, 150–157.
<https://doi.org/10.1016/J.RSASE.2018.11.003>
- Das, Sayantan, Kar, N. S., & Bandyopadhyay, S. (2015). Glacial lake outburst flood at Kedarnath, Indian Himalaya: a study using digital elevation models and satellite images. *Natural Hazards*, 77(2), 769–786. <https://doi.org/10.1007/S11069-015-1629-6>
- Davis David. (2020, August). *Random Forest Classifier Tutorial: How to Use Tree-Based Algorithms for Machine Learning*. <https://www.freecodecamp.org/news/how-to-use-the-tree-based-algorithm-for-machine-learning/>
- Dehecq, A., Gourmelen, N., Gardner, A. S., Brun, F., Goldberg, D., Nienow, P. W., Berthier, E., Vincent, C., Wagnon, P., & Trouvé, E. (2019). Twenty-first century glacier slowdown driven by mass loss in High Mountain Asia. *Nature Geoscience*, 12(1), 22–27. <https://doi.org/10.1038/S41561-018-0271-9>
- Ding, Y., Liu, S., Li, J., & Shangguan, D. (2006). The retreat of glaciers in response to recent climate warming in western China. *Annals of Glaciology*, 43, 97–105.
<https://doi.org/10.3189/172756406781812005>
- Dobhal, D. P., Kumar, S., & Mundepi, A. K. (1995). monsoon-arid transition zone : An exam Chhota Shigri glacier , Himachal-Himala Morphology and glacier dynamics stu. *JSTOR*, 68(9), 936–944.
<https://www.jstor.org/stable/24096758>
- Erten, E., Reigber, A., Hellwich, O., & Prats, P. (2009). Glacier velocity monitoring by maximum likelihood texture tracking. *IEEE Transactions on Geoscience and Remote Sensing*, 47(2), 394–405.
<https://doi.org/10.1109/TGRS.2008.2009932>
- Evans, A. N. (2000). Glacier Surface Motion Computation from Digital Image Sequences. *IEEE*

TRANSACTIONS ON GEOSCIENCE AND REMOTE SENSING, 38(2), 1064–1072.

- Farinotti, D., Huss, M., Fürst, J. J., Landmann, J., Machguth, H., Maussion, F., & Pandit, A. (2019). A consensus estimate for the ice thickness distribution of all glaciers on Earth. *Nature Geoscience* 2019 12:3, 12(3), 168–173. <https://doi.org/10.1038/s41561-019-0300-3>
- Fattahi, H., & Amelung, F. (2013). DEM error correction in InSAR time series. *IEEE Transactions on Geoscience and Remote Sensing*, 51(7), 4249–4259. <https://doi.org/10.1109/TGRS.2012.2227761>
- Fischer, A., Rott, H., Björnsson, H., Fischer, A., Rott, H., & Björnsson, H. (2003). Observation of recent surges of Vatnajökull, Iceland, by means of ERS SAR interferometry. *AnGla*, 37, 69–76. <https://doi.org/10.3189/172756403781815546>
- Frauenfelder, R., & Kääb, A. (2000). Towards a palaeoclimatic model of rock-glacier formation in the Swiss Alps. *Annals of Glaciology*, 31, 281–286. <https://doi.org/10.3189/172756400781820264>
- Frey, H., Paul, F., & Strozzi, T. (2012). Compilation of a glacier inventory for the western Himalayas from satellite data: methods, challenges, and results. *Remote Sensing of Environment*, 124, 832–843. <https://doi.org/10.1016/J.RSE.2012.06.020>
- Friedl, P., Seehaus, T., & Braun, M. (2021). Global time series and temporal mosaics of glacier surface velocities, derived from Sentinel-1 data. *Earth System Science Data Discussions*, June, 1–33. <https://doi.org/10.5194/essd-2021-106>
- Gabriel, A. K., Goldstein, R. M., & Zebker, H. A. (1989). Mapping small elevation changes over large areas: Differential radar interferometry. *Journal of Geophysical Research: Solid Earth*, 94(B7), 9183–9191. <https://doi.org/10.1029/JB094IB07P09183>
- Hall, D. K., Ormsby, J. P., Bindschadler, R. A., & Siddalingaiah, H. (1987). Characterization of Snow and Ice Reflectance Zones On Glaciers Using Landsat Thematic Mapper Data. *Annals of Glaciology*, 9, 104–108. <https://doi.org/10.3189/S0260305500000471>
- Hambrey, M. J., Murray, T., Glasser, N. F., Hubbard, A., Hubbard, B., Stuart, G., Hansen, S., Kohler, J., Hambrey, M. J., Murray, T., Glasser, N. F., Hubbard, A., Hubbard, B., Stuart, G., Hansen, S., & Kohler, J. (2005). Structure and changing dynamics of a polythermal valley glacier on a centennial timescale: Midre Lovénbreen, Svalbard. *J. Geophys. Res*, 110, 1006. <https://doi.org/10.1029/2004JF000128>
- Hanssen, R. F. (2001). *Radar Interferometry: Data Interpretation and Error Analysis (PhD Thesis)*.
- Hetland, E. A., Musé, P., Simons, M., Lin, Y. N., Agram, P. S., & Dicaprio, C. J. (2012). Multiscale InSAR Time Series (MInTS) analysis of surface deformation. *Journal of Geophysical Research: Solid Earth*, 117(B2), 2404. <https://doi.org/10.1029/2011JB008731>
- Hooper, A., Zebker, H., Segall, P., & Kampes, B. (2004). A new method for measuring deformation on volcanoes and other natural terrains using InSAR persistent scatterers. *Geophysical Research Letters*, 31(23), 1–5. <https://doi.org/10.1029/2004GL021737>
- Huang, L., & Li, Z. (2011). Comparison of SAR and optical data in deriving glacier velocity with feature tracking. <http://Dx.Doi.Org/10.1080/01431161003720395>, 32(10), 2681–2698. <https://doi.org/10.1080/01431161003720395>
- Jehad Ali, N. A. (2012). (PDF) Random Forests and Decision Trees. *International Journal of Computer Science Issues*, 9(5), 1694–0814. https://www.researchgate.net/publication/259235118_Random_Forests_and_Decision_Trees
- Jesko Schaper, K. S. (2000, June). Modelling Daily Runoff From Snow And Glacier Melt Using Remote Sensing Data. *20th EARSeL Symposium on Remote Sensing*. https://www.researchgate.net/publication/2541315_Modelling_Daily_Runoff_From_Snow_And_Glacier_Melt_Using_Remote_Sensing_Data
- Jiang, Z., Wu, K., Liu, S., Wang, X., Zhang, Y., Tahir, A. A., & Long, S. (2021). Surging dynamics of South Rimo Glacier, Eastern Karakoram. *Environmental Research Letters*, 16(11), 114044. <https://doi.org/10.1088/1748-9326/AC3175>
- Kääb, A., Chiarle, M., Raup, B., & Schneider, C. (2007). Climate change impacts on mountain glaciers and permafrost. *Global and Planetary Change*, 56(1–2). <https://doi.org/10.1016/j.gloplacha.2006.07.008>
- Kaab, A., Wessels, R., Haeberli, W., Huggel, C., Kargel, J., Jodha, S., & Khalsa, S. (2003). Rapid ASTER imaging facilitates timely assessment of glacier hazards and disasters. *Eos, Transactions American Geophysical Union*, 84(13), 117–121. <https://doi.org/10.1029/2003EO130001>
- Khadka, M., Steiner, J., Hassan, J., Maussion, F., Fujita, K., Gurung, T., He, X., Liu, Q., Mandal, A., Miles, E., Quincey, D., Wagnon, P., Watson, S., Yang, W., & Zhao, C. (2021). Performance Evaluation of

- Existing Algorithms and Datasets for Glacier Surface Velocity Estimation in Himalayan Glaciers. *AGUFM*, 2021, C13B-04. <https://ui.adsabs.harvard.edu/abs/2021AGUFM.C13B..04K/abstract>
- Khan, A. A., Jamil, A., Hussain, D., Taj, M., Jabeen, G., & Malik, M. K. (2020). Machine-Learning Algorithms for Mapping Debris-Covered Glaciers: The Hunza Basin Case Study. *IEEE Access*, 8, 12725–12734. <https://doi.org/10.1109/ACCESS.2020.2965768>
- Kodde, M. P., Pfeifer, N., Gorte, B. G. H., Geist, T., & Höfle, B. (2007). AUTOMATIC GLACIER SURFACE ANALYSIS FROM AIRBORNE LASER SCANNING. *LAPRS*, XXXVI(3).
- König, M., Winther, J. G., & Isaksson, E. (2001). Measuring snow and glacier ice properties from satellite. *Reviews of Geophysics*, 39(1), 1–27. <https://doi.org/10.1029/1999RG000076>
- Koskinen, J., Pulliainen, J., & Hallikainen, M. (2000). Effect of snow wetness to C-band backscatter - a modeling approach. *International Geoscience and Remote Sensing Symposium (IGARSS)*, 4, 1754–1756. <https://doi.org/10.1109/IGARSS.2000.857335>
- Kulkarni, A. V. (1992). Mass balance of Himalayan glaciers using AAR and ELA methods. *Journal of Glaciology*, 38(128), 101–104. <https://doi.org/10.1017/S0022143000009631>
- Kulkarni, Anil V., Rathore, B. P., Singh, S. K., & Bahuguna, I. M. (2011). Understanding changes in the Himalayan cryosphere using remote sensing techniques. <https://doi.org/10.1080/01431161.2010.517802>, 32(3), 601–615. <https://doi.org/10.1080/01431161.2010.517802>
- Kulkarni, Anil V., Dhar, L., Rathore, B., Govindha Raj, B. K., & Kalia, R. (2006). RECESSION OF SAMUDRA TAPU GLACIER, CHANDRA RIVER BASIN, HIMACHAL PRADESH. *Journal of the Indian Society of Remote Sensing*, 34(1).
- Kumar, V., Venkataramana, G., & Högda, K. A. (2011). Glacier surface velocity estimation using SAR interferometry technique applying ascending and descending passes in Himalayas. *International Journal of Applied Earth Observation and Geoinformation*, 13(4), 545–551. <https://doi.org/10.1016/J.JAG.2011.02.004>
- Kumar, Vinit, Mehta, M., & Shukla, T. (2021). Spatially resolved estimates of glacial retreat and lake changes from Gepang Gath Glacier, Chandra Basin, Western Himalaya, India. *MAY2021 JOURNAL GEOLOGICAL SOCIETY OF INDIA*, 97, 520–526. <https://doi.org/10.1007/s12594-021-1718-y>
- Kurt Cuffey, W. S. B. P. (2006). *The Physics of Glaciers - 4th Edition* (4th ed., Vol. 1). Academic Press. <https://www.elsevier.com/books/the-physics-of-glaciers/cuffey/978-0-12-369461-4>
- Leprince, S., & Ayoub, F. (2009). Earth Surface Monitoring with COSI-Corr, Techniques and Applications. *American Geophysical Union, 2009*, IN43D-1171. <https://ui.adsabs.harvard.edu/abs/2009AGUFMIN43D1171L/abstract>
- Leprince, S., Lin, J., Ayoub, F., Herman, F., Avouac, J., Leprince, S., Lin, J., Ayoub, F., Herman, F., & Avouac, J. (2013). 3D high resolution tracking of ice flow using multi-temporal stereo satellite imagery, Franz Josef Glacier, New Zealand. *AGUFM*, 2013, G22A-07. <https://ui.adsabs.harvard.edu/abs/2013AGUFM.G22A..07L/abstract>
- Leprince, Sébastien, Barbot, S., Ayoub, F., & Avouac, J. P. (2007). Automatic and precise orthorectification, coregistration, and subpixel correlation of satellite images, application to ground deformation measurements. *IEEE Transactions on Geoscience and Remote Sensing*, 45(6), 1529–1558. <https://doi.org/10.1109/TGRS.2006.888937>
- Lu, Y., Zhang, Z., & Huang, D. (2020). Glacier mapping based on random forest algorithm: A case study over the eastern Pamir. *Water (Switzerland)*, 12(11), 1–25. <https://doi.org/10.3390/W12113231>
- Lu, Y., Zhang, Z., Kong, Y., & Hu, K. (2022). Integration of optical, SAR and DEM data for automated detection of debris-covered glaciers over the western Nyainqentanglha using a random forest classifier. *Cold Regions Science and Technology*, 193, 103421. <https://doi.org/10.1016/J.COLDREGIONS.2021.103421>
- Luckman, A., Quincey, D., & Bevan, S. (2007). The potential of satellite radar interferometry and feature tracking for monitoring flow rates of Himalayan glaciers. *Remote Sensing of Environment*, 111(2–3), 172–181. <https://doi.org/10.1016/J.RSE.2007.05.019>
- Lutz, E., Geist, T., & Stötter, J. (2003). INVESTIGATIONS OF AIRBORNE LASER SCANNING SIGNAL INTENSITY ON GLACIAL SURFACES-UTILIZING COMPREHENSIVE LASER GEOMETRY MODELING AND ORTHOPHOTO SURFACE MODELING (A CASE STUDY: SVARTISHEIBREEN, NORWAY).

- Mahagaonkar, A., Thakur, P. K., & Chang, L. (2019). Assessment of Sentinel-1 Products for Revealing Glacier Surface Movement in Indian Himalayas Using Differential Sar Interferometry. *International Geoscience and Remote Sensing Symposium (IGARSS)*, 2070–2073. <https://doi.org/10.1109/IGARSS.2019.8898831>
- Massonnet, D., Rossi, M., Carmona, C., Adragna, F., Peltzer, G., Feigl, K., & Rabaute, T. (1993). The displacement field of the Landers earthquake mapped by radar interferometry. *Nature* 1993 364:6433, 364(6433), 138–142. <https://doi.org/10.1038/364138a0>
- Mayewski, P. A., & Jeschke, P. A. (1979). Himalayan and trans-Himalayan glacier fluctuations since AD 1812. *Arctic And Alpine Research*, 11(3), 267–287. <https://doi.org/10.2307/1550417>
- Moon, T., Joughin, I., Smith, B., Van Den Broeke, M. R., Van De Berg, W. J., Noël, B., & Usher, M. (2014). Distinct patterns of seasonal Greenland glacier velocity. *Geophysical Research Letters*, 41(20), 7209–7216. <https://doi.org/10.1002/2014GL061836>
- Moore, R. D., Fleming, S. W., Menounos, B., Wheate, R., Fountain, A., Stahl, K., Holm, K., & Jakob, M. (2009). Glacier change in western North America: influences on hydrology, geomorphic hazards and water quality. *Hydrological Processes*, 23(1), 42–61. <https://doi.org/10.1002/HYP.7162>
- Moreira, A., Prats-Iraola, P., Younis, M., Krieger, G., Hajnsek, I., & Papathanassiou, K. P. (2013). A tutorial on synthetic aperture radar. *IEEE Geoscience and Remote Sensing Magazine*, 1(1), 6–43. <https://doi.org/10.1109/MGRS.2013.2248301>
- Murray, T., Booth, A., & Rippin, D. M. (2007). Water-content of Glacier-ice: Limitations on estimates from velocity analysis of surface ground-penetrating radar surveys. *Journal of Environmental and Engineering Geophysics*, 12(1), 87–99. <https://doi.org/10.2113/JEEG12.1.87>
- NASA. (2022). *Evidence | Facts – Climate Change: Vital Signs of the Planet*. <https://climate.nasa.gov/evidence/>
- NASA JPL. (n.d.). *ASF Home Page | ASF*. Retrieved January 2, 2023, from <https://asf.alaska.edu/>
- Neyret & Benastar. (2005). Water crisis looms as Himalayan glaciers retreat. *WWF*, 2(2), 1–6. https://wwf.panda.org/wwf_news/?unewsid=19111
- Nijhawan, R., Das, J., & Balasubramanian, R. (2018). A Hybrid CNN + Random Forest Approach to Delineate Debris Covered Glaciers Using Deep Features. *Journal of the Indian Society of Remote Sensing*, 46(6), 981–989. <https://doi.org/10.1007/S12524-018-0750-X/FIGURES/5>
- Nijhawan, R., Garg, P., & Thakur, P. (2016). A comparison of classification techniques for glacier change detection using multispectral images. *Perspectives in Science*, 8, 377–380. <https://doi.org/10.1016/J.PISC.2016.04.080>
- NSIDC. (n.d.). *Global Land Ice Velocity Extraction from Landsat 8 (GoLIVE), Version 1 | National Snow and Ice Data Center*. Retrieved January 5, 2023, from <https://nsidc.org/data/nsidc-0710/versions/1>
- Osmanoğlu, B., Sunar, F., Wdowinski, S., & Cabral-Cano, E. (2016). Time series analysis of InSAR data: Methods and trends. *ISPRS Journal of Photogrammetry and Remote Sensing*, 115, 90–102. <https://doi.org/10.1016/J.ISPRSJPRS.2015.10.003>
- Pablo Anzar. (2020, December 2). *Decision Trees: Gini vs Entropy | Quantdare*. <https://quantdare.com/decision-trees-gini-vs-entropy/>
- Partington, K. C. (1998a). Discrimination of glacier facies using multi-temporal SAR data. *Journal of Glaciology*, 44(146), 42–53. <https://doi.org/10.3189/S0022143000002331>
- Partington, K. C. (1998b). Discrimination of glacier facies using multi-temporal SAR data. *Journal of Glaciology*, 44(146), 42–53. <https://doi.org/10.3189/S0022143000002331>
- Pedregosa FABIANPEDREGOSA, F., Michel, V., Grisel OLIVIERGRISEL, O., Blondel, M., Prettenhofer, P., Weiss, R., Vanderplas, J., Cournapeau, D., Pedregosa, F., Varoquaux, G., Gramfort, A., Thirion, B., Grisel, O., Dubourg, V., Passos, A., Brucher, M., Perrot and Édouardand, M., Duchesnay, and Édouard, & Duchesnay EDOUARD DUCHESNAY, Fré. (2011). Scikit-learn: Machine Learning in Python Gaël Varoquaux Bertrand Thirion Vincent Dubourg Alexandre Passos PEDREGOSA, VAROQUAUX, GRAMFORT ET AL. Matthieu Perrot. *Journal of Machine Learning Research*, 12, 2825–2830. <http://scikit-learn.sourceforge.net>
- Pedregosa FABIANPEDREGOSA, G. V. (2011). Scikit-Learn: Machine learning in Python. *JMLR*, 12(85), 2825–2830.
- Pellikka, P., & Rees, W. G. (2009). Remote Sensing of Glaciers: Techniques for Topographic, Spatial and Thematic Mapping of Glaciers. In *Remote Sensing of Glaciers: Techniques for Topographic, Spatial and Thematic Mapping of Glaciers*. CRC Press. <https://doi.org/10.1201/B10155/REMOTE-SENSING-GLACIERS-GARETH-REES-PETRI-PELLIKKA>

- Planet*. (n.d.). <https://www.planet.com/products/planet-imagery/>
- Reet Kamal Tiwari. (2014). Estimation of surface ice velocity of Chhota- Shigri glacier using sub-pixel ASTER image correlation. *Current Science*, 106(6).
https://www.researchgate.net/publication/260993110_Estimation_of_surface_ice_velocity_of_Chhota-Shigri_glacier_using_sub-pixel_ASTER_image_correlation
- Reigber, A., & Scheiber, R. (2003). Airborne differential SAR interferometry: First results at L-band. *IEEE Transactions on Geoscience and Remote Sensing*, 41(6 PART II), 1516–1520.
<https://doi.org/10.1109/TGRS.2003.814610>
- RGI Consortium. (2017). *GLIMS: Global Land Ice Measurements from Space*. A Dataset of Global Glacier Outlines: Version 6.0: Technical Report, Global Land Ice Measurements from Space, Colorado, USA. <https://doi.org/https://doi.org/10.7265/4m1f-gd79>
- Rosen, P. A., Hensley, S., Peltzer, G., & Simons, M. (2004). Updated repeat orbit interferometry package released. *Eos, Transactions American Geophysical Union*, 85(5), 47–47.
<https://doi.org/10.1029/2004EO050004>
- Rott, H., & Mätzler, C. (1987). Possibilities and Limits of Synthetic Aperture Radar for Snow and Glacier Surveying. *Annals of Glaciology*, 9, 195–199. <https://doi.org/10.3189/S0260305500000604>
- Rutberg, R. L., Hemming, S. R., & Goldstein, S. L. (2000). Reduced North Atlantic Deep Water flux to the glacial Southern Ocean inferred from neodymium isotope ratios. *Nature*, 405(6789), 935–938.
<https://doi.org/10.1038/35016049>
- Sahu, R., & Gupta, R. D. (2019). Spatiotemporal variation in surface velocity in Chandra basin glacier between 1999 and 2017 using Landsat-7 and Landsat-8 imagery.
<https://doi.org/10.1080/10106049.2019.1659423>, 36(14), 1591–1611.
<https://doi.org/10.1080/10106049.2019.1659423>
- Sahu, R., & Gupta, R. D. (2020). Snow cover area analysis and its relation with climate variability in Chandra basin, Western Himalaya, during 2001–2017 using MODIS and ERA5 data. *Environmental Monitoring and Assessment*, 192(8), 1–26. <https://doi.org/10.1007/s10661-020-08442-8>
- Sam, L., Bhardwaj, A., Kumar, R., Buchroithner, M. F., & Martín-Torres, F. J. (2018). Heterogeneity in topographic control on velocities of Western Himalayan glaciers. *Scientific Reports*, 8(1).
<https://doi.org/10.1038/S41598-018-31310-Y>
- Sánchez-Gómez, P., Navarro, F. J., Paul, F., Wuite, J., Briggs, K., McNabb, R., Nuth, C., Li, X., & Thenkabail, P. S. (2017). Glacier Surface Velocity Retrieval Using D-InSAR and Offset Tracking Techniques Applied to Ascending and Descending Passes of Sentinel-1 Data for Southern Ellesmere Ice Caps, Canadian Arctic. *Remote Sensing 2017, Vol. 9, Page 442*, 9(5), 442.
<https://doi.org/10.3390/RS9050442>
- Sangewar, C. (2009). *Inventory of the Himalayan glaciers : a contribution to the international hydrological programme* (Updated ed.). Director General Geological Survey of India.
- Satyabala, S. P. (2016). Spatiotemporal variations in surface velocity of the Gangotri glacier, Garhwal Himalaya, India: Study using synthetic aperture radar data. *Remote Sensing of Environment*, 181, 151–161. <https://doi.org/10.1016/J.RSE.2016.03.042>
- Scambos, T. A., Bohlander, J. A., Shuman, C. A., & Skvarca, P. (2004). Glacier acceleration and thinning after ice shelf collapse in the Larsen B embayment, Antarctica. *Geophysical Research Letters*, 31(18), 2001–2004. <https://doi.org/10.1029/2004GL020670>
- Scherler, D., Leprince, S., & Strecker, M. R. (2008). Glacier-surface velocities in alpine terrain from optical satellite imagery—Accuracy improvement and quality assessment. *Remote Sensing of Environment*, 112(10), 3806–3819. <https://doi.org/10.1016/J.RSE.2008.05.018>
- Schmidt, D. A., & Bürgmann, R. (2003). Time-dependent land uplift and subsidence in the Santa Clara valley, California, from a large interferometric synthetic aperture radar data set. *Journal of Geophysical Research: Solid Earth*, 108(B9). <https://doi.org/10.1029/2002JB002267>
- Sharma, P., Ramanathan, A. L., & Pottakkal, J. (2013). Study of solute sources and evolution of hydrogeochemical processes of the Chhota Shigri Glacier meltwaters, Himachal Himalaya, India. <https://doi.org/10.1080/02626667.2013.802092>, 58(5), 1128–1143.
<https://doi.org/10.1080/02626667.2013.802092>
- Sharma, S. S., & Ganju, A. (2000). Complexities of avalanche forecasting in Western Himalaya - an overview. *Cold Regions Science and Technology*, 31(2), 95–102. [https://doi.org/10.1016/S0165-232X\(99\)00034-8](https://doi.org/10.1016/S0165-232X(99)00034-8)

- Shi, J., & Dozier, J. (1995). Inferring Snow Wetness Using C-Band Data from SIR-C's Polarimetric Synthetic Aperture Radar. *IEEE Transactions on Geoscience and Remote Sensing*, 33(4), 905–914. <https://doi.org/10.1109/36.406676>
- Shrestha, A. B., & Aryal, R. (2011). Climate change in Nepal and its impact on Himalayan glaciers. *Regional Environmental Change*, 11(SUPPL. 1), 65–77. <https://doi.org/10.1007/S10113-010-0174-9/TABLES/3>
- Shridhar Jawak, Sagar Filipe, K. B. (2022). High-Resolution Remote Sensing for Mapping Glacier Facies in the Arctic. *Remote Sensing Technology and the Three Poles*. <https://doi.org/https://doi.org/10.1002/9781119787754.ch26>
- Siegert, M. J. (2008). Chapter 6 Numerical Modelling of the Antarctic Ice Sheet. *Developments in Earth and Environmental Sciences*, 8, 235–256. [https://doi.org/10.1016/S1571-9197\(08\)00006-2](https://doi.org/10.1016/S1571-9197(08)00006-2)
- Sivalingam, S., Murugesan, G. P., Dhulipala, K., Kulkarni, A. V., & Pandit, A. (2021). Essential study of Karakoram glacier velocity products extracted using various techniques. *Geocarto International*, 0(0), 1–17. <https://doi.org/10.1080/10106049.2021.1974954>
- Snapiro, B., Momblanch, A., Jain, S. K., Waite, T. W., & Holman, I. P. (2019). A method for monthly mapping of wet and dry snow using Sentinel-1 and MODIS: Application to a Himalayan river basin. *International Journal of Applied Earth Observation and Geoinformation*, 74, 222–230. <https://doi.org/10.1016/J.JAG.2018.09.011>
- Sood, S. (2016). *Glacier Classification and Movement Estimation using SAR Polarimetric and Interferometric Techniques*.
- Speiser, J. L., Miller, M. E., Tooze, J., & Ip, E. (2019). A comparison of random forest variable selection methods for classification prediction modeling. *Expert Systems with Applications*, 134, 93–101. <https://doi.org/10.1016/J.ESWA.2019.05.028>
- Sridhar Jawak. (2015). (PDF) Potential of SAR imagery for mapping and monitoring iceberg calving events in Antarctic environment. *XII International Symposium on Antarctic Earth Science*. https://www.researchgate.net/publication/280111605_Potential_of_SAR_imagery_for_mapping_and_monitoring_iceberg_calving_events_in_Antarctic_environment
- Strozzi, T., Luckman, A., Murray, T., Wegmüller, U., & Werner, C. L. (2002). Glacier motion estimation using SAR offset-tracking procedures. *IEEE Transactions on Geoscience and Remote Sensing*, 40(11), 2384–2391. <https://doi.org/10.1109/TGRS.2002.805079>
- Suring, L. H. (2020). Freshwater: A Glossary of Terminology Used in Freshwater Biology and Management. *Encyclopedia of the World's Biomes*, 4–5, 462–470. <https://doi.org/10.1016/B978-0-12-409548-9.12447-9>
- Thakur, P. K., Aggarwal, S. P., Arun, G., Sood, S., Senthil Kumar, A., Mani, S., & Dobhal, D. P. (2017). Estimation of Snow Cover Area, Snow Physical Properties and Glacier Classification in Parts of Western Himalayas Using C-Band SAR Data. *Journal of the Indian Society of Remote Sensing*, 45(3), 525–539. <https://doi.org/10.1007/S12524-016-0609-Y>
- Ulaby, F. T., Moore, R. K., Fung, A. K., Moore, R. K., & Fung, A. K. (1982). *Microwave remote sensing: Active and passive. Volume 2 - Radar remote sensing and surface scattering and emission theory*.
- van den Broeke, M. R., Bamber, J., Lenaerts, J., & Rignot, E. (2011). Ice Sheets and Sea Level: Thinking Outside the Box. *Surveys in Geophysics*, 32(4–5), 495–505. <https://doi.org/10.1007/S10712-011-9137-Z/FULLTEXT.HTML>
- Van Wychen, W., Burgess, D. O., Gray, L., Copland, L., Sharp, M., Dowdeswell, J. A., & Benham, T. J. (2014). Glacier velocities and dynamic ice discharge from the Queen Elizabeth Islands, Nunavut, Canada. *Geophysical Research Letters*, 41(2), 484–490. <https://doi.org/10.1002/2013GL058558>
- Vijay Mahagaonkar, A. (2019). *Glacier Surface Velocity Estimation & Facies Classification using InSAR and Multi-Temporal SAR Techniques in Indian Himalaya*.
- Vijay, S., Khan, S. A., Kusk, A., Solgaard, A. M., Moon, T., & Bjørk, A. A. (2019). Resolving Seasonal Ice Velocity of 45 Greenlandic Glaciers With Very High Temporal Details. *Geophysical Research Letters*, 46(3), 1485–1495. <https://doi.org/10.1029/2018GL081503>
- Wangchuk, S., & Bolch, T. (2020). Mapping of glacial lakes using Sentinel-1 and Sentinel-2 data and a random forest classifier: Strengths and challenges. *Science of Remote Sensing*, 2, 100008. <https://doi.org/10.1016/J.SRS.2020.100008>
- Werner, C., Wegmüller, U., Strozzi, T., & Wiesmann, A. (2000, September 16). GAMMA SAR AND INTERFEROMETRIC PROCESSING SOFTWARE. *ERS-ENVISAT Symposium*.

- <http://www.gamma-rs.ch>
- Wolken, G. J., Sharp, M., & Wang, L. (2009). Snow and ice facies variability and ice layer formation on Canadian Arctic ice caps, 1999–2005. *Journal of Geophysical Research: Earth Surface*, 114(F3). <https://doi.org/10.1029/2008JF001173>
- Yellala, A., Kumar, V., & Høgda, K. A. (2019a). Bara Shigri and Chhota Shigri glacier velocity estimation in western Himalaya using Sentinel-1 SAR data. *International Journal of Remote Sensing*, 40(15), 5861–5874. <https://doi.org/10.1080/01431161.2019.1584685>
- Yellala, A., Kumar, V., & Høgda, K. A. (2019b). Bara Shigri and Chhota Shigri glacier velocity estimation in western Himalaya using Sentinel-1 SAR data. *International Journal of Remote Sensing*, 40(15), 5861–5874. <https://doi.org/10.1080/01431161.2019.1584685>
- Yunjun, Z., Fattahi, H., & Amelung, F. (2019). *Small baseline InSAR time series analysis: Unwrapping error correction and noise reduction*. <https://doi.org/10.1016/j.cageo.2019.104331>
- Zemp, M., Huss, M., Thibert, E., Eckert, N., McNabb, R., Huber, J., Barandun, M., Machguth, H., Nussbaumer, S. U., Gärtner-Roer, I., Thomson, L., Paul, F., Maussion, F., Kutuzov, S., & Cogley, J. G. (2019). Global glacier mass changes and their contributions to sea-level rise from 1961 to 2016. *Nature* 2019 568:7752, 568(7752), 382–386. <https://doi.org/10.1038/s41586-019-1071-0>
- Zhou, C., & Zheng, L. (2017). Mapping Radar Glacier Zones and Dry Snow Line in the Antarctic Peninsula Using Sentinel-1 Images. *Remote Sensing 2017, Vol. 9, Page 1171*, 9(11), 1171. <https://doi.org/10.3390/RS9111171>
- Zhou, X., Chang, N. Bin, & Li, S. (2009). Applications of SAR interferometry in earth and environmental science research. *Sensors*, 9(3), 1876–1912. <https://doi.org/10.3390/S90301876>
- Zhou, Y., Chen, J., & Cheng, X. (2021). Glacier velocity changes in the himalayas in relation to ice mass balance. *Remote Sensing*, 13(19). <https://doi.org/10.3390/RS13193825>

ANNEXURE

Feature Tracking with SAR Dataset

The feature tracking procedure for Sentinel datasets are commonly performed in sentinel application platform. Other studies (Luckman et al., 2007)(Khadka et al., 2021) used the same for feature tracking velocity estimation. This study intends to use SARPROZ software by Periz as it has never been used for cryosphere studies. The pixel tracking feature is still in the Beta phase and hence the response of the software over the IHR can be observed.

All images chosen were for the month of September as this month has the least snow cover. The algorithm works better for feature tracking in a snow free setting. The co-registration process was tricky and was not accurate as compared to previous studies (Yellala et al., 2019a) that used SNAP over the same study areas for prior years. Trial and error method was used for finding the optimal parameters for co-registration of the image pairs chosen.

Sentinel-1 SLC datasets in VV polarization were used as GRD data is still not being supported in the software. 1092820 points were used for the process of co-registration with a correlation window size of 16, a reference window size of 64, an SNR threshold of 7, pixel search step size of 12. The amplitude correlation threshold was set at 0.3. An external STRM DEM of 30m resolution was used for co-registration assistance.

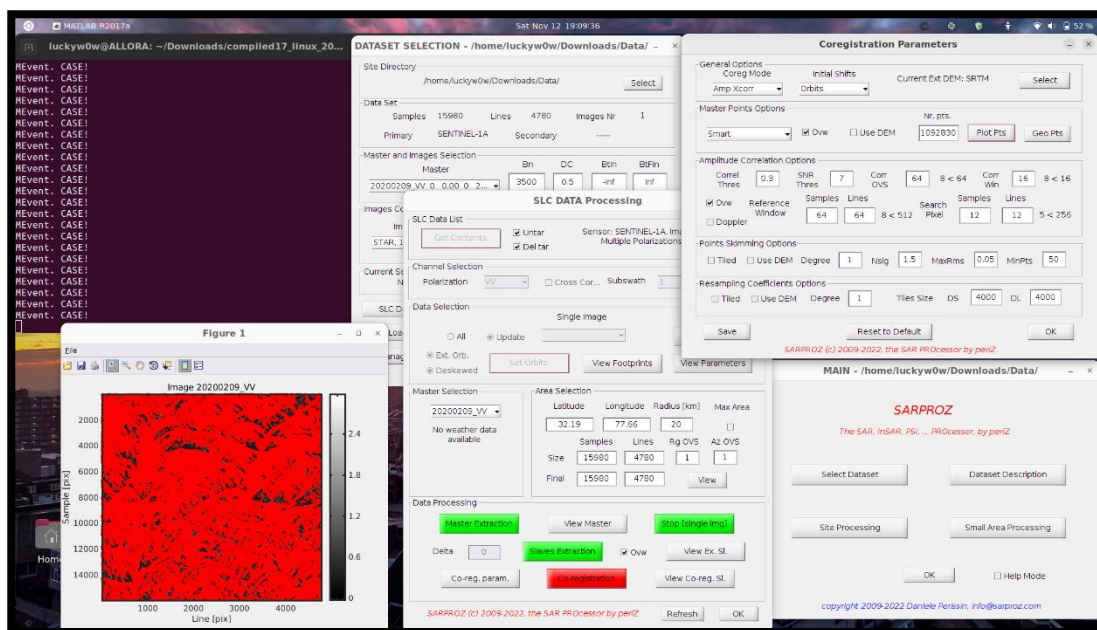


Figure 43 Screenshot of Co-registration process and the relevant parameters. Map of chosen master points.

The software does not allow outputs to be exported as TIFF imagery, hence relevant maps or postprocessing could not be carried out. All outputs were obtained in the form of .PNG scatterplots. Hence a more decipherable map with the glacier boundaries could not be generated. The Scatterplots for each year pairs of analysis are given below.

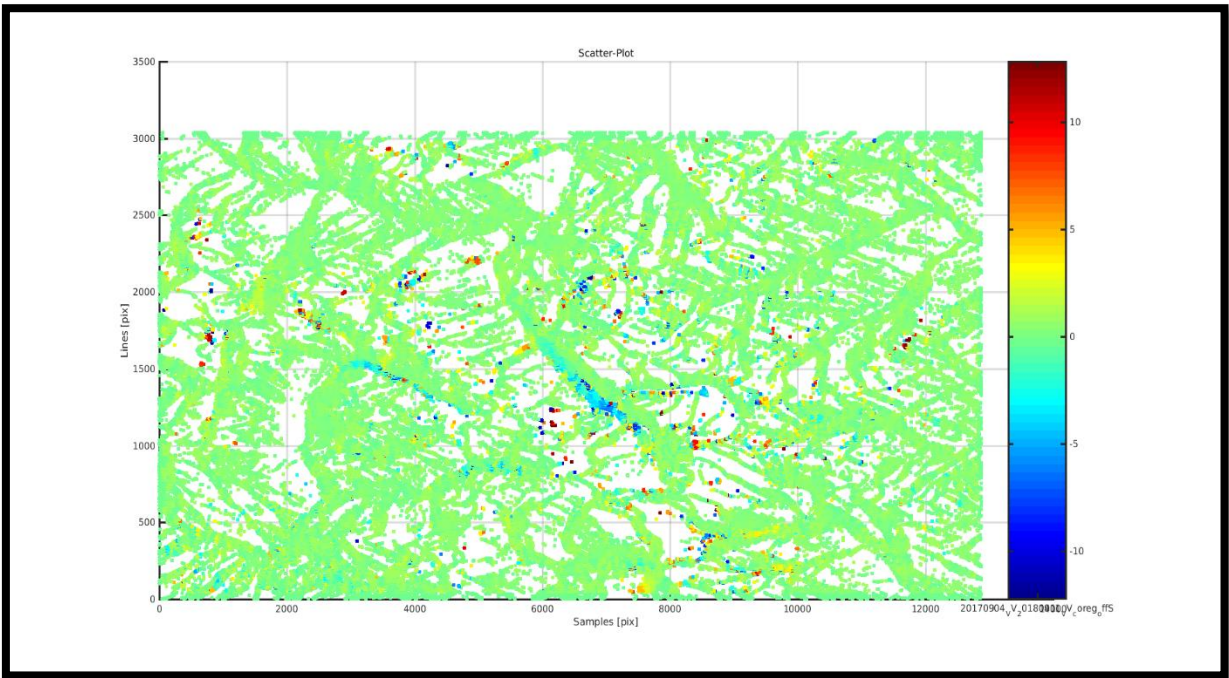


Figure 44 Velocity Scatterplot for 2017-2018

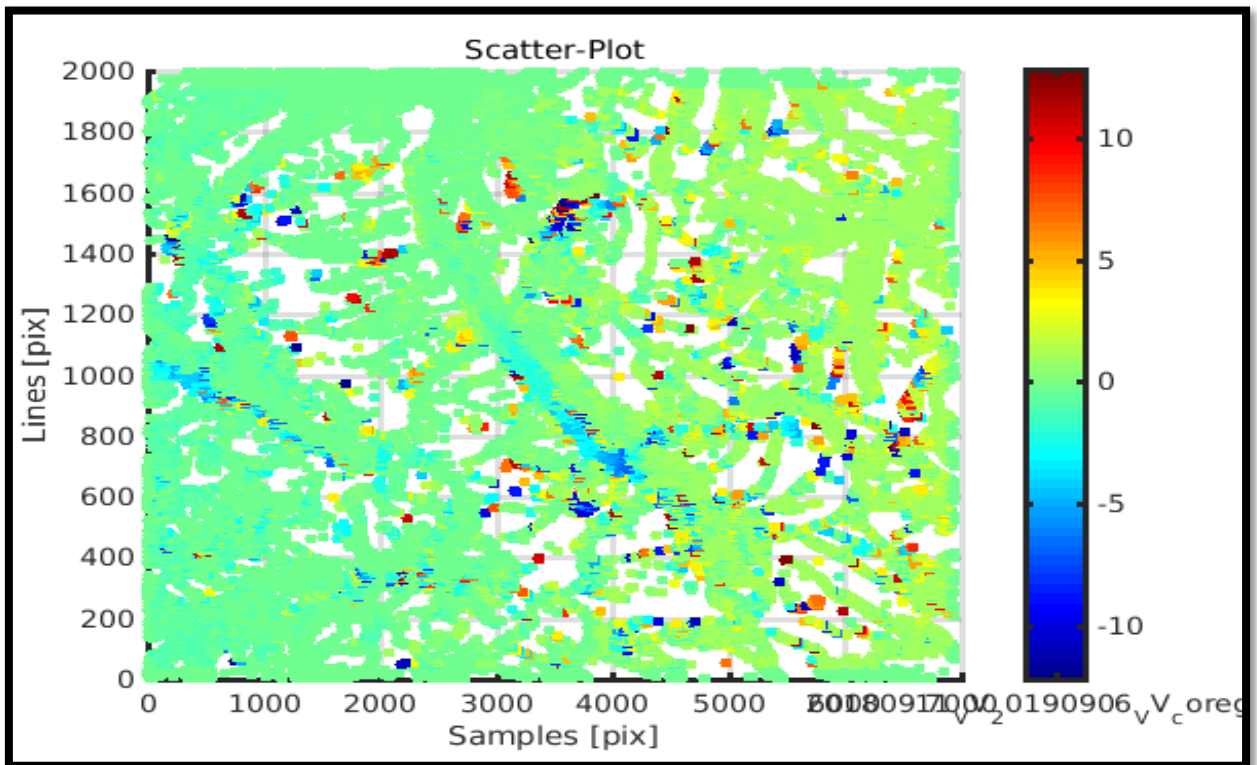


Figure 45 Velocity Scatterplot for 2018-2019

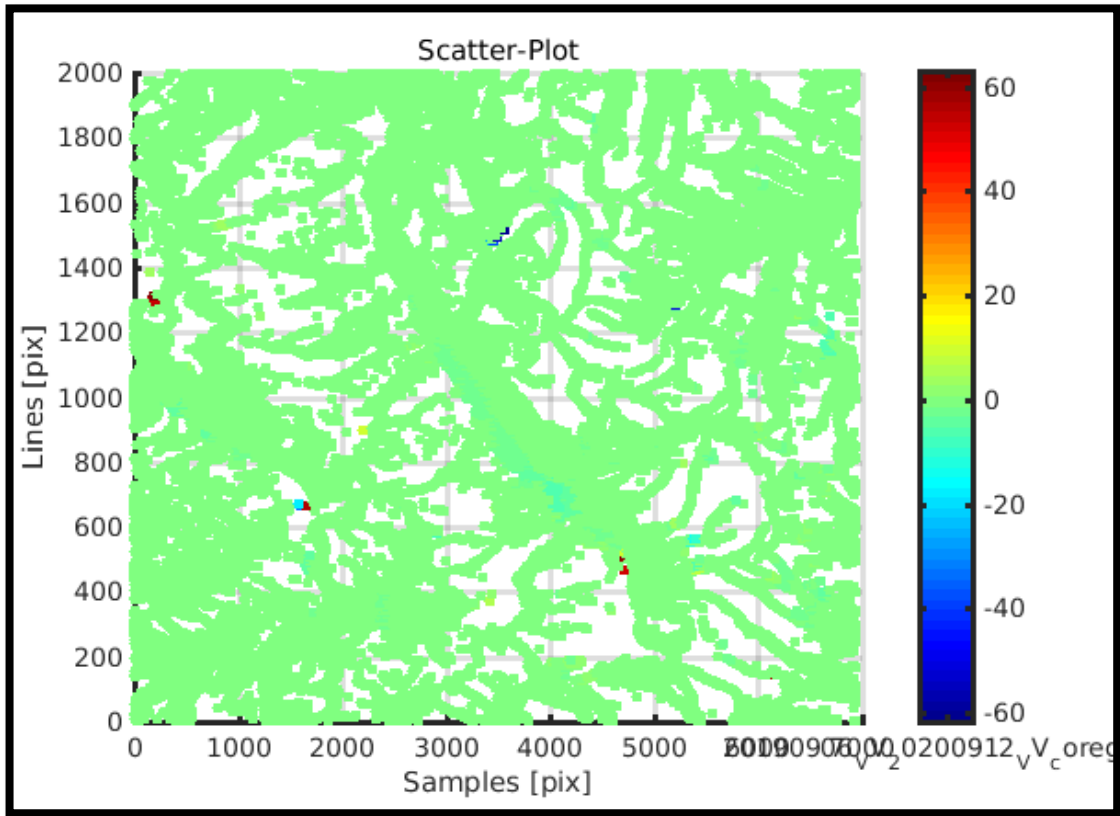


Figure 46 Velocity Scatterplot for 2019-2020

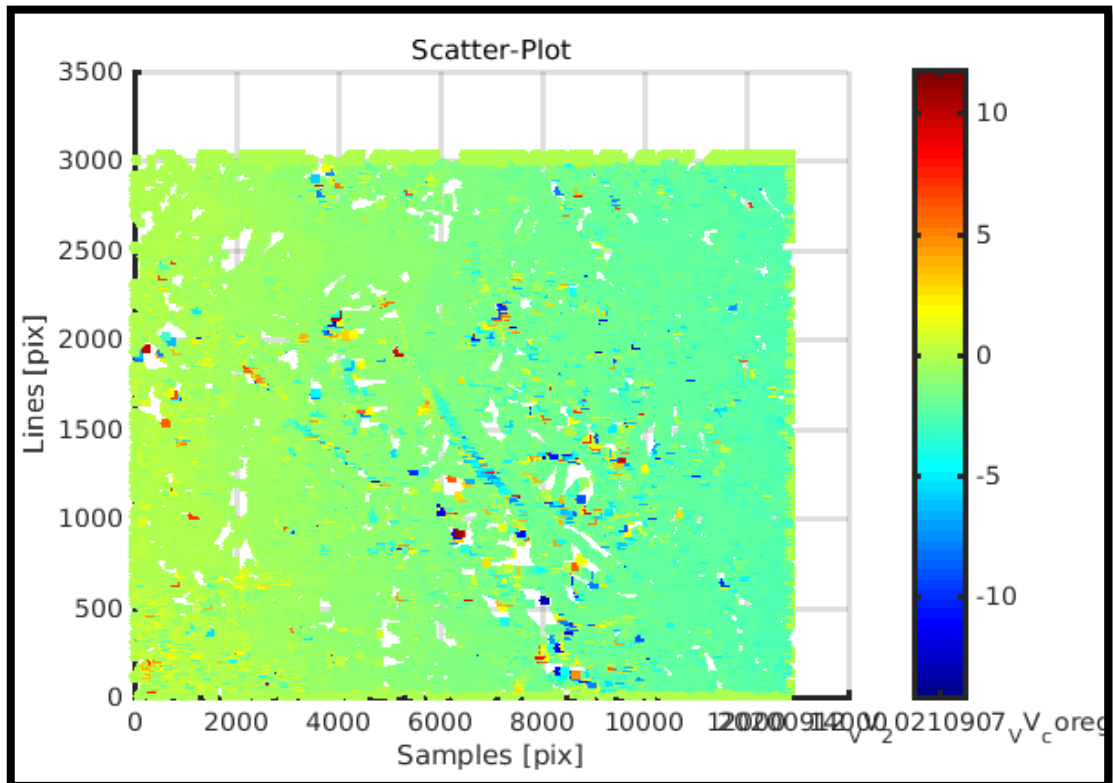


Figure 47 Velocity Scatterplot for 2020-2021

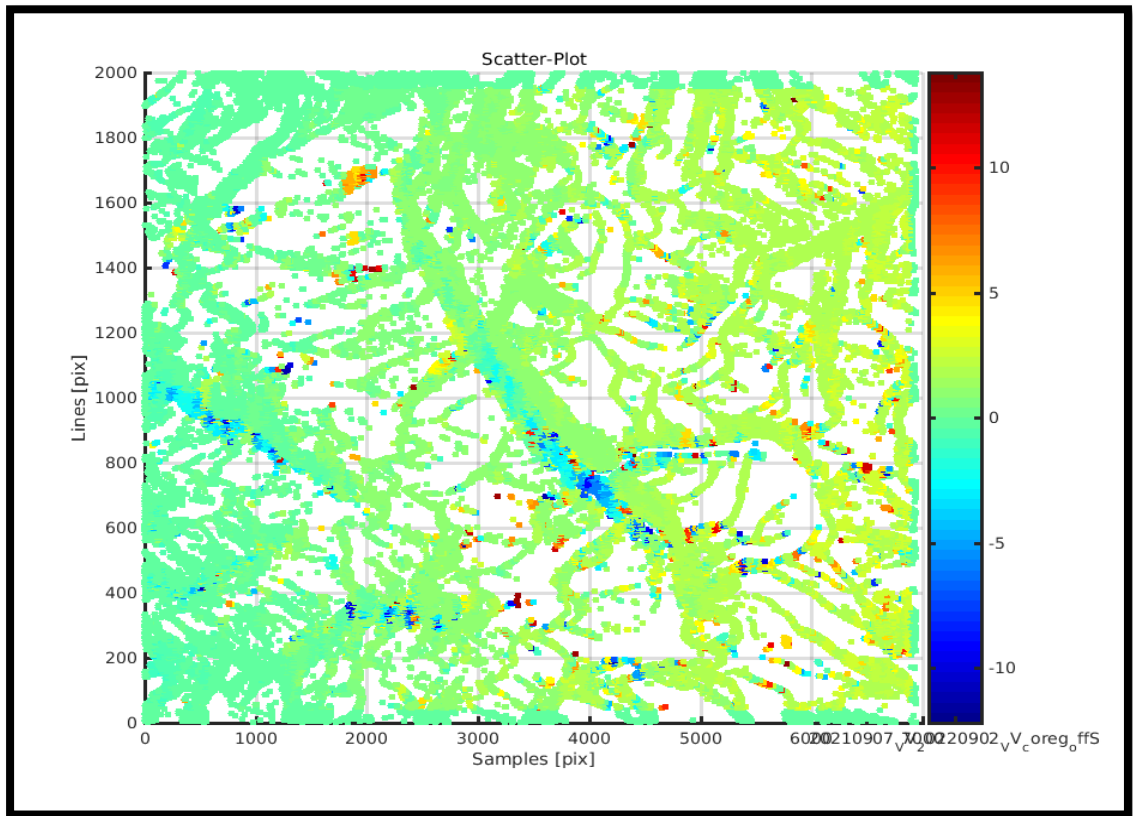


Figure 48 Velocity Scatterplot for 2021-2022

Although the algorithm could not detect movement across the whole glacier, a velocity of 12m/year can be seen in Bada Shigri glacier. A velocity of about 6m/year can be seen in Chotta Shigri glacier and a movement of about 6 m/year can be seen in Gepang Gath Glacier.

It can be observed that the pixel tracking algorithm could not accurately generate the velocity result for the study areas. The glaciers of the Himalayan region tend to be slow moving and not all feature tracking algorithms respond well to them (Sivalingam et al., 2021).